OBSERVATIONS OF
THE WIND FIELD IN THE FIRST TEN METERS
OF THE ATMOSPHERE ABOVE THE OCEAN

by

Kenneth Warren Ruggles

B.S. United States Naval Academy

(1954)

M.S. United States Naval Postgraduate School

(1960)

SUBMITTED IN PARTIAL FULFILLMENT

OF THE REQUIREMENT FOR THE

DEGREE OF DOCTOR OF PHILOSOPHY

at the

MASSACHUSETTS INSTITUTE OF TECHNOLOGY

May 16, 1969

Signature of Author .....
Department of Meteorology, May 16, 1969

Certified by .....
Thesis Supervisor

Accepted by .....
Chairman, Departmental Committee on
Graduate Students
Lindgren

Observations of the Wind Field in the First Ten Meters of the Atmosphere Above the Ocean

Kenneth Warren Ruggles

Submitted to the Department of Meteorology on 16 May 1969 in partial fulfillment of the requirement for the degree of Doctor of Philosophy.

ABSTRACT

Simultaneous measurements of mean wind speed, horizontal wind velocity, vertical wind velocity, and water height were made during the summer of 1968 at an exposed field site off the New England Coast. A vertical array of five cup anemometers provided wind speed data for heights extending up to 8.2 meters. Hot film anemometers operated in pairs measured component wind velocities at a height of 1 meter above the mean water level. Hot film anemometers mounted on two horizontally separated instrument platforms measured a two-point spatial correlation field. Measurements were conducted with and without an artificial sea slick on the water, demonstrating the importance of small waves to air-sea interaction.

Analysis of the wind profile data indicates better than 90 percent of the validly measured wind profiles are logarithmic. The friction velocity U_* is a linear function of wind speed in the range of wind speeds studied, while the roughness length parameter, z_o, is highly structured. The structure of the roughness length parameter can be explained in part by the Kelvin-Helmholtz instability and the onset of wave generation. A discoutinuity at 4 meters/sec^{-1} cannot be explained. The drag coefficient is constant with a value of 1.6×10^{-3} except in the vicinity of roughness length discontinuities. The mean wind speed at 10 meters is represented as the sum of a mean profile term and a velocity defect term constructed from the correlation between U_* and z_o. The velocity defect term has a systematic behavior as a function of wind speed.

Taylor's Hypothesis is tested based on cross-correlations and cross spectral denisty computations of the data from spatially separated hot film anemometers. Taylor's Hypothesis does not appear to be consistently valid for atmospheric turbulence in the general spectral domain

of ocean surface waves. Reynolds stress measurements are consistent with the values observed by other investigators and with the values inferred from the wind profile data. Cross spectral density computations indicate that the near-surface horizontal velocity is a maximum over the wave trough for both the well and the wind waves, except when the water is covered by a slick. In the case of a slick, the horizontal velocity has its maximum value over the wave crest of the swell and looses coherence with the wind sea.

Thesis Supervisor: Erik L. Mollo-Christensen

Title Professor of Meteorology

Table of Contents

List of Illustrations

Tables

Introduction

This paper is concerned with the momentum transfer processes at the air-sea interface; specifically those processes which contribute to the growth and maintenance of wind waves. Attention is focused on the atmosphere over the ocean, and the isolation and identification of atmospheric phenomena unique to the ocean atmosphere. As a matter of viewpoint, the research was approached with a minimum concern for the air's action on the sea, as opposed to the sea's action upon the atmosphere, in the belief that the atmosphere's ability to transfer energy into the ocean is dependent primarily on the nature of the effects of the ocean on the atmosphere.

As a point of departure, we look at the atmosphere directly over the ocean from the point of view of the atmospheric investigator as contrasted with that view commonly held by the wind wave investigator. The former tends to consider the ocean surface as just another rigid boundary, where the magnitude and direction of the energy fluxes across the boundary are not considered. [Paulson (1967); Pond, Smith, Hamblin, and Burling (1967); Pond, Stewart, and Burling (1963).] While such an approach appears to result in the proper wind profiles over the sea, it is obviously the incorrect viewpoint when discussing the energetics of the air-sea interface. Stewart (1967) has shown that the saturated wind wave field has gained momentum from the atmosphere equivalent to the entire momentum contained in the atmospheric mean wind extending to a height of one ocean wave wavelength (roughly 40-60 meters as a typical

figure). Intuitively, during a falling sea, one should expect the momentum flux across the air-sea boundary to reverse sign.

The wind wave investigator, looking up from below, tends to treat the atmosphere as an infinite energy source over the ocean, being milked of momentum in response to proper excitation from the wave below. Again this appears to be a correct viewpoint in a most general sense, however one is left asking just how much momentum can the atmosphere provide.

The focal point for the different viewpoints in the treatment of the atmosphere is the vertical mean wind profile. Stewart (1961) and Kinsman (1965) argue that the magnitude of the momentum flux from the atmosphere to the ocean is so large that the atmosphere should not be able to support a logarithmic profile. Atmospheric investigations, such as those summarized by Roll (1964), show that the oceanic profile is in general a logarithmic profile, but beg the question of explaining the maintenance of the profile in the face of wave generation. All of this suggests to this investigator that the oceanic vertical mean wind profile must be considered as the result of a quite different process from that effecting its rigid boundary counterpart.

The research reported in this paper has tried to identify unique aspects of the oceanic wind profile, and there find some explanation for the existence of these unique aspects. The research, and consequently this report, can be conveniently divided into three general areas. The first area is the development and use of suitable measurement techniques needed to observe the atmosphere over the ocean. Next, the vertical mean wind profile is examined. Finally, some information is presented

concerning the two-dimensional motions directly above the ocean. As an illuminating side bearing on the results, some experimental results with artificial sea-slicks are reported.

I

Site and Instrumentation

Field measurements were conducted from a rigid spar designed and erected under the supervision of Professor Erik Mollo-Christensen in Buzzard's Bay, Massachusetts. The spar was placed in 60 feet of water as shown in figure 1.1, and provided an ideal platform for mounting sensitive instruments for air-sea interaction studies.

Figure 1.2 is a rough sketch of the geography of the area around the spar. Prevailing winds for the area are from the Southwest, and almost all of the observations recorded were of winds from the Southern sector. The nearest land to the Southwest is Block Island, at a distance of 26 miles. The bottom topography to the South and Southwest gradually increases in depth, so one need not be concerned about wave field distortion due to upwind and up-sea shoaling of the wind-waves studied in this report.

The deep water, the high wind speed variability, the virtually unlimited fetches to the South, and the rigid instrument platform provide an excellent environment for the study of air-sea interaction processes.

Figure 1.3 is a photograph of the spar with instruments rigged. Note that the instruments are mounted on the end of a trainable instrument boom extending 12 feet from the spar. The boom was oriented into the wind at the beginning of each run, and was elevated or depressed so that an inscribed boom "waterline" was positioned at the mean water level of the sea expected for the duration of the data run. During any given data run, the mean water height would vary less than 1 foot due to tidal effects, and was treated as being essentially constant during the run.

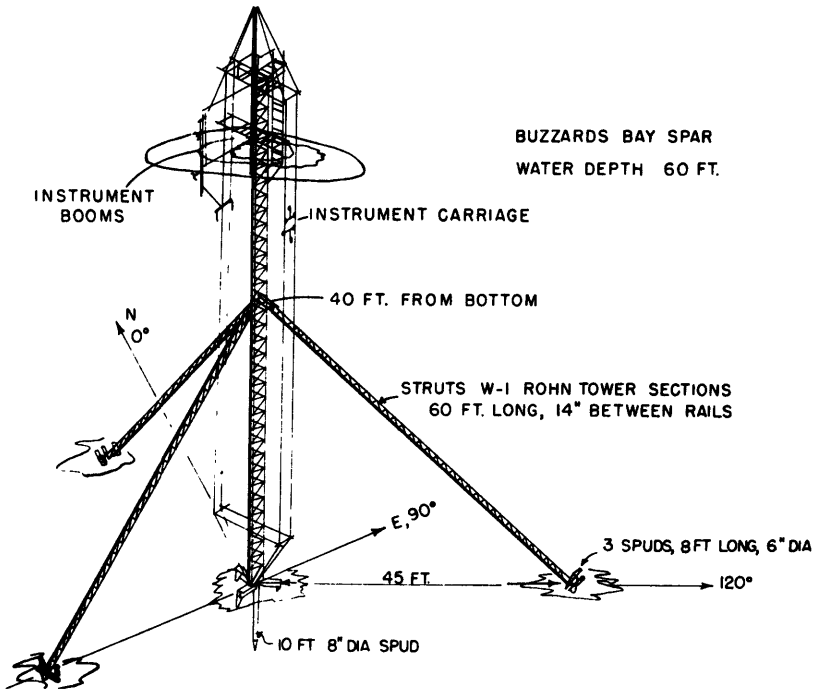

Figure 1.1

Bottom mounted spar design for use in Buzzards Bay during the summer of 1968.

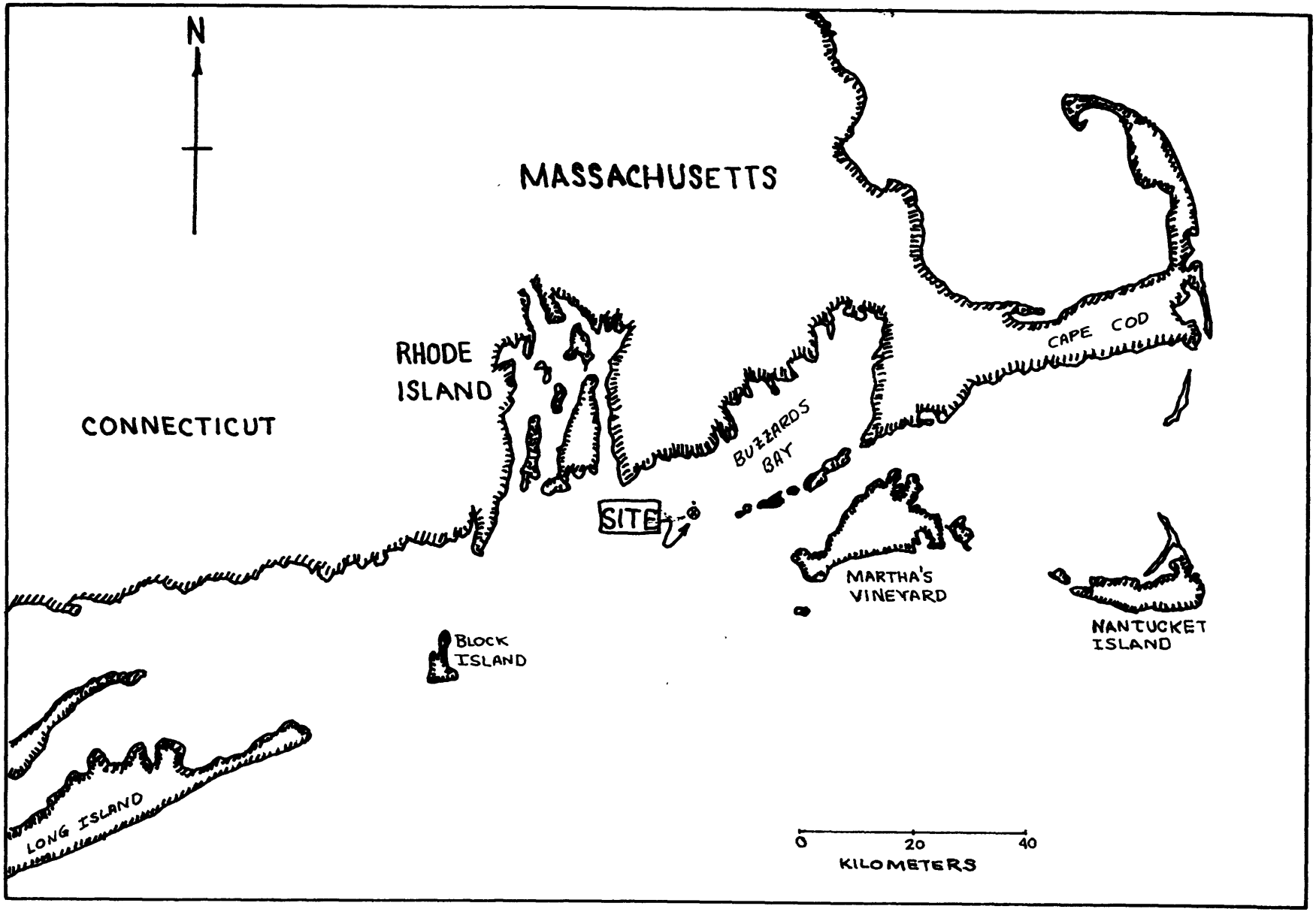

Figure 1.2 Air-Sea Interaction site location

For spatial wind correlation studies, a taut moored, moveable, wind stabilized instrument buoy as placed at various locations near the main spar. Initial plans called for two such buoys, as shown in figure 1.4, however, one of the buoys was lost during heavy weather before experiments could be conducted using two buoys simultaneously. The portable buoy consisted of an instrument cage mounted on the end of a 25 foot section of 2 inch structual aluminum pipe, of which 6 to 10 feet protruded above the water. The floatation for the buoy was roughly 10 feet below the water line. The instrument electronics were contained in a Sears-Roebuck pressure cooker, as shown in figure 1.5. A hot film probe was mounted on the end of a two meter long combination instrument support and radio antenna. The entire instrument package was dropped into bearing sleeves mounted in the instrument cage when the buoy was to be used, otherwise the instruments were maintained ashore.

The instrumentation on the spar and the portable buoy remained unchanged during the entire summer of 1968, except for minor variations to accommodate special experiments. The instrumentation consisted of:

One Beckman and Whitley 6-cup anemometer and wind vane system mounted at the top of the spar at a height of 8.2 meters.

Four C. W. Thorthwaite Associates cup anemometers located at 1, 2, 3, and 5 meters above the mean water level.

Two sets of DISA S & B battery operated hot film anemometers mounted at 1 and 5 meters above the mean water level. The hot film probes were used in pairs as described in chapter II, to provide direct measurement of Reynold's stress.

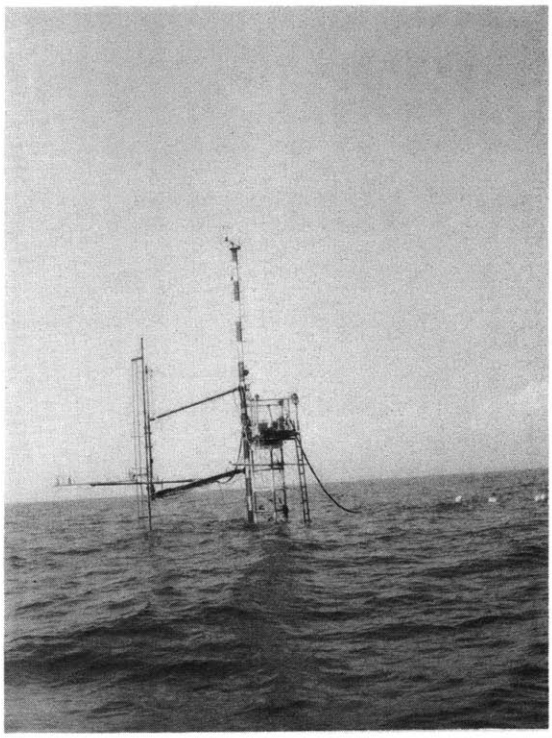

Figure 1.3 Instrument spar with boom extended and instruments rigged.

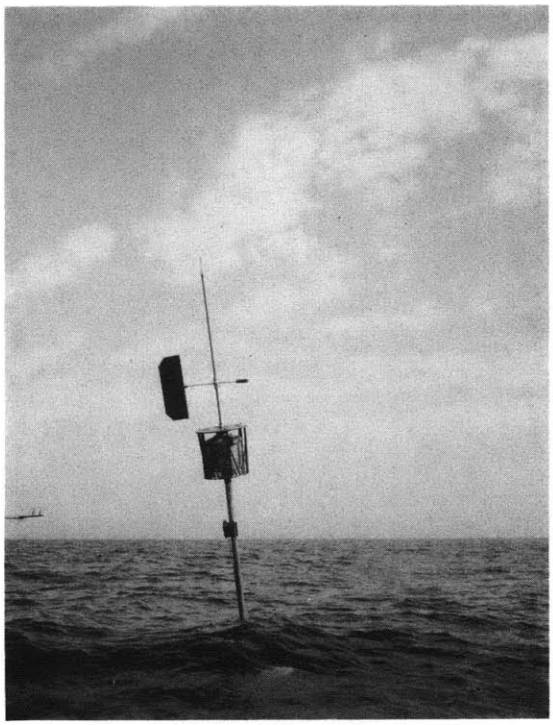

Figure 1.4 Satellite Buoy.

One capacitance wave gauge designed by the Department of Meteorology Fluid Dynamics Laboratory, mounted directly below the hot film anemometers.

One set of slope-matched thermistors mounted at 1 meter and at 5 meters to give temperature difference readings for the computation of Richardson's number.

One hot film anemometer and associated circuitry located on the portable buoy.

The signals from the various sensors on the spar were preprocessed as necessary, and then transmitted through a floating umbilical cord to the R. R. Shrock, moored by a two point moor 150 feet downwind from the spar. The signals from the portable buoy were transmitted by radio link. The data logging system on board the Shrock is shown in figure 1.6. The Thornthwaite Cup anemometer data was recorded and printed out by a Thornthwaite model 106 wind profile register system. The temperature data and the wind direction was recorded on strip-chart recorders. The remaining data was recorded on a Precision Instrument 6208 8-channel tape recorder.

Considerable attention was given to the transmission of the hotwire signals. The outputs of these anemometers were linearized using an in-house designed linearizer (see appendix 3) and then converted into a frequency modulated signal prior to transmission and recording. Such preprocessing is considered essential to maintaning signal fidelity and low signal-to-noise ratios for the hot film signals. In the case of hot films operating together as pairs for the direct measurement of Reynolds stress, an additional

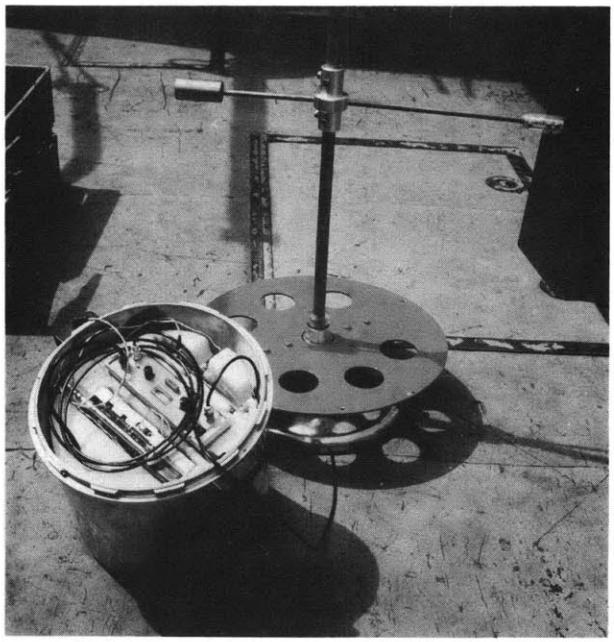

Figure 1.5 Satellite buoy instrument package constructed from pressure cooker with instruments in place.

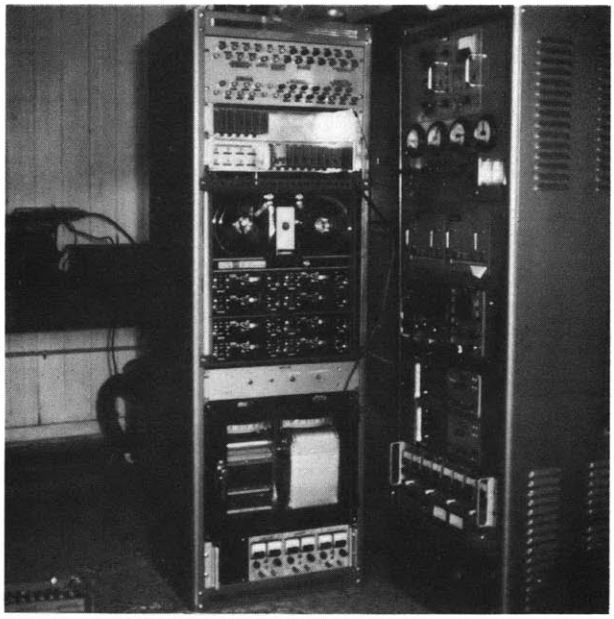

Figure 1.6 Data logging system on board the R/V R.R. Shrock.

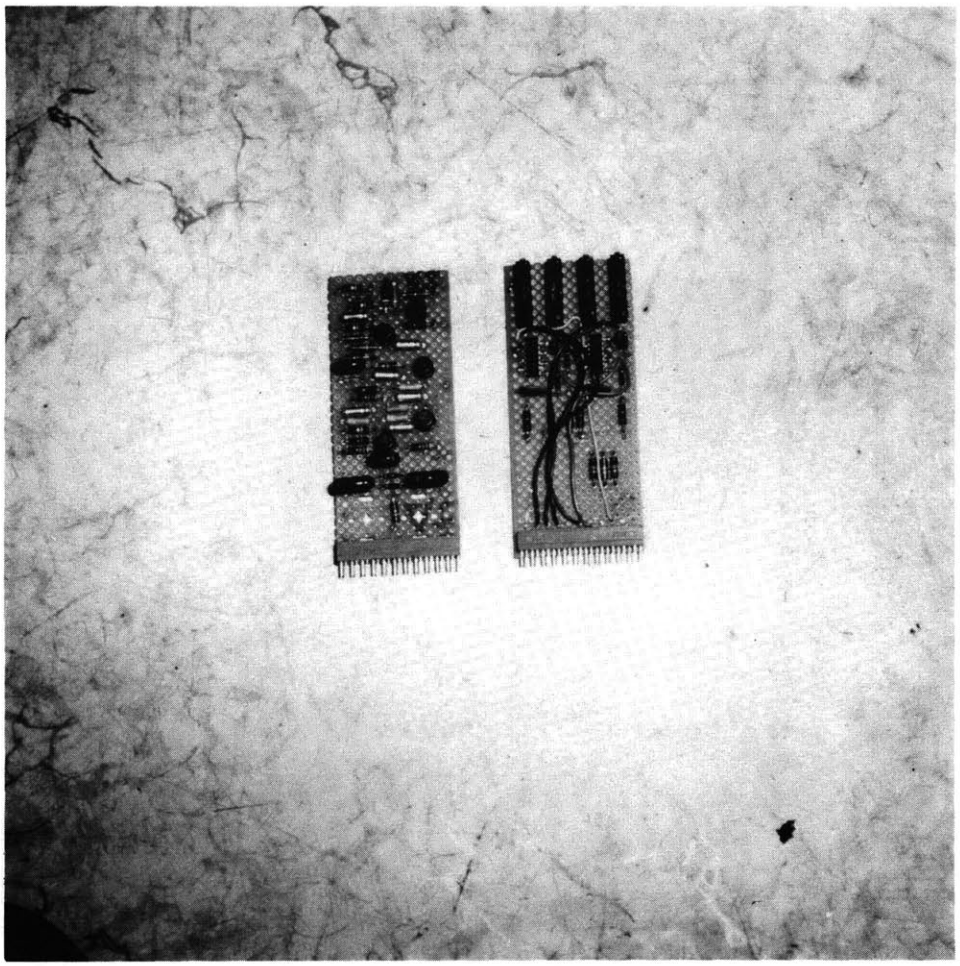

Figure 1.7 Signal conditioning amplifier (left) and voltage-controlled oscillator (right) constructed for use with hotwire systems.

precaution was taken by multiplexing the two signals prior to transmission and recording. This avoided any question of phase match errors due to multipath transmission effects, tape recorder head alignment, etc.

With the exception of the temperature difference measurements and the wave gauges, all of the equipment consisted of standard off-the-shelf hardware. A full description of the cup anemometers, the wave gauges, and their characteristics is covered by Seesholtz (1968). A discussion of the Reynolds stress measurement is contained in Chapter II.

Turbulent fluctuations in the atmosphere were measured using DISA type 55D05 hot wire anemometers in conjunction with DISA 55A85 hot film probes. The anemometers are battery operated, compact, and ideally suited to the rugged field environment. The probes consist of a platinum film sensing element fused to a wedge-shaped tip of a quartz support. The film is electrically insulated from the salt air by a thin quartz coating over the film. The probes were operated at an overheat ratio of 1.7 to 1, recommended by the manufacturer as being the optimum for a probe operated in air and subjected to dousing from occasional rain drops or intermittent water immersion. While the probes performed well in the field and survived environmental extremes, they were subject to sudden and unanticipated step changes in their characteristic operating resistance, requiring close monitoring. Several days of promising data had to be discarded because of this probe behavior. Additional probe characteristics are discussed in Chapter II.

Figure 1.7 shows the conditioning amplifiers and voltage controlled oscillators employed with the hotwire anemometers. The amplifiers were built around Texas Instrument integrated operational amplifier chips. The voltage controlled oscillator is a modification to the standard design presented in Navships 93484 (selected semiconductor circuits).

The temperature difference measuring device consisted of two ruggedized bead thermistors encased in glass, each mounted in identical, naturally ventilated radiation shields. The thermistor beads were slope-matched to provide an identical resistance variation for a given temperature variation to within one part in 10^3. Each thermistor was connected as opposing elements of a balanced bridge, the output of which was amplified by standard operational amplifiers and calibrated to provide a full scale meter deflection on board the R. R. Shrock chart recorder in response to a 1 degree centigrade temperature difference. The high mass of the glass around each bead resulted in a system time constant of approximately 20 seconds, providing high damping and stability. After the system had settled down, it was capable of measuring temperature differences to with .01 degrees centigrade in an ideal environment.

While the instrument worked quite satisfactorily in the laboratory and during pierside tests, it was somewhat of a disappointment at sea. As shown by the tabulated Richardson number calculations in Appendix I, the instrument would work well when the sea conditions closely approximated the ideal conditions available at pierside. Otherwise it would not work at all. The primary problem was the wet bulb effect caused by the deposition of salt spray on the bead. A suitable solution was not found for this problem.

Chapter II

The Direct Measurement of Reynolds Stress

General.

The direct measurement of Reynolds stress at some point near the water surface has been one of the major problems in the observation of air-sea interaction processes. Instruments capable of providing such measurements are usually quite delicate, and require special handling and care to survive the hostile marine environment. The nature of the physical processes under study further impose demanding requirements of dynamic response and sensitivity far beyond that required of the laboratory test environment. The importance of Reynolds stress measurements to the understanding of the near ocean atmospheric turbulence, coupled with the lack of literature discussing the instrumental problem, requires that this problem be separately considered in detail.

The over-riding instrumental requirement in air-sea interaction studies is resolution, with dynamic range running a close second. Wind perturbations induced by the underlying wave action represents a small percentage of the overall turbulent energy. Consequently the instruments must not only have the dynamic range to handle the large gusts characteristic of the atmosphere in general, but must also have the sensitivity to detect the small wave-induced fluctuations. Hot film probes, operated in orthogonally mounted pairs, have been chosen as being best suited for this study. They fulfill the requirements of sensitivity and dynamic range, and have the rugged construction essential to instruments operated in the maritime environment.

Instrument Calibration and Response

From the outset it is assumed that the Reynolds stress sensor is mounted on a rigid mount near the ocean surface. Pond (1968) has discussed the effects of buoy motion, which must be considered if a rigid mount is not available. The problem of Reynolds stress measurement in general will be treated first, followed by the specific case of a hot film probe pair.

Kraus (1968) has shown for an instrument whose alignment deviates from a true vertical by an angle of one degree that one can expect errors in the measurement of Reynolds stress in excess of 100 percent. Kraus suggested several indirect approaches which might be suitable for correcting this error, both of which are considered unsuited for near-ocean measurements. An alternate approach to those of Kraus is to invoke the continuity condition that the mean vertical velocity near the boundary goes to zero, and use this to correct for instrument alignment error.

Let U and W represent horizontal and vertical components of the wind. The apparent velocities as sensed by the instrument will be denoted by a subscript (a). Following the usual Reynolds convention, an overbar denotes a mean quantity, while a prime represents a deviation from the mean. From the geometry of figure 2.1, one can write:

$$W_a + U \sin\alpha + W \cos\alpha$$

$$U_a = U \cos\alpha - W \sin\alpha \qquad (2.1)$$

Applying the Reynolds convention and invoking the requirement that $\overline{W} = 0$, equation (2.1) can be written:

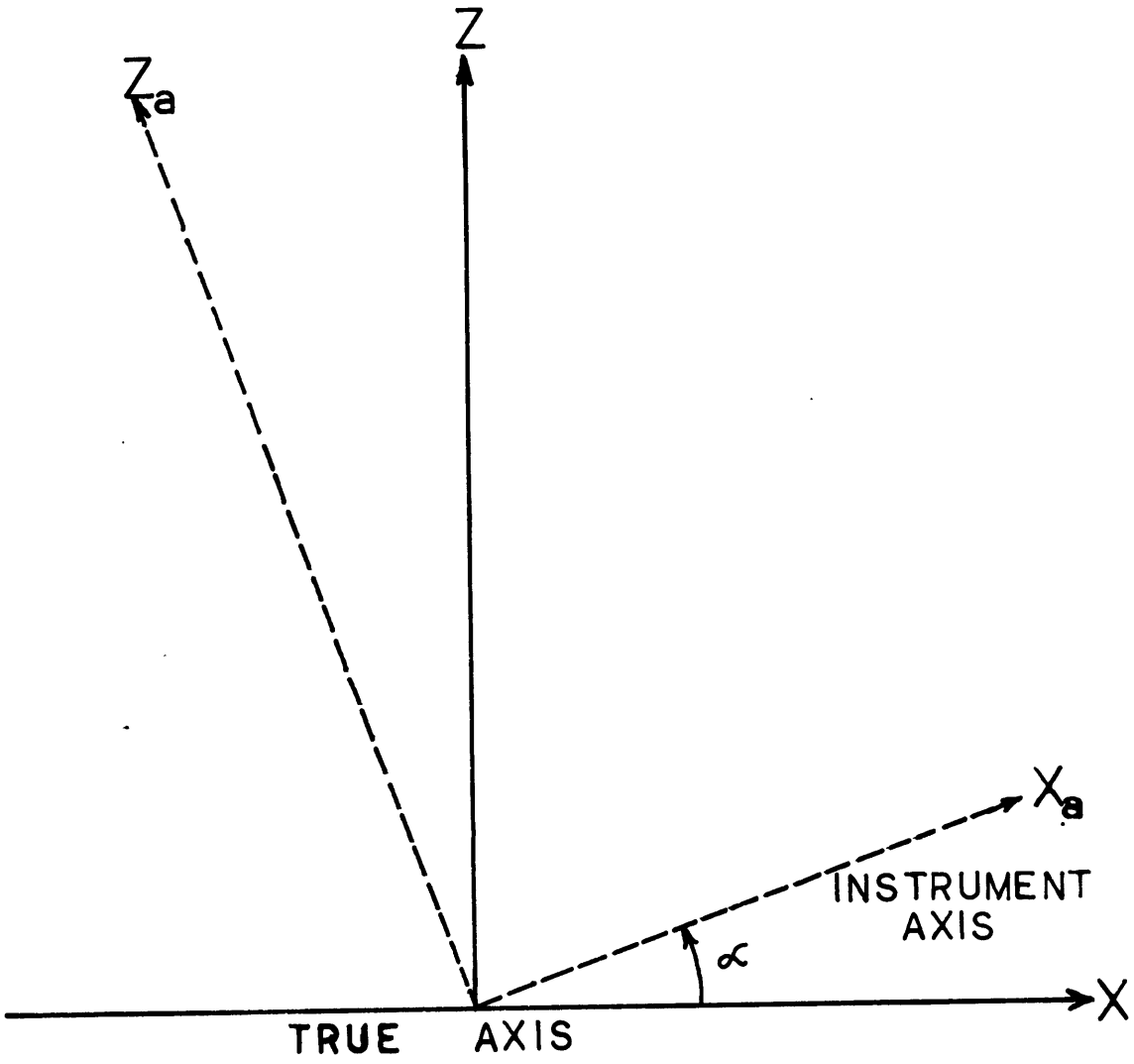

FIGURE 2.1

Geometery of Instrument alignment error.

$$\overline{Wa} = \overline{U} \sin \alpha$$

$$\overline{Ua} = \overline{U} \cos \alpha$$

$$w'a = u' \sin\alpha + w' \cos\alpha$$

$$u'a = u \cos\alpha - w' \sin\alpha \qquad (2.2)$$

Forming the Reynolds stress term from equation (2.2):

$$\overline{u'w'} = \overline{U'aW'a} \cos 2\alpha - \frac{1}{2}\sin 2\alpha \, (\overline{U'a^2} - \overline{w'a^2}) \qquad (2.3)$$

Equation (2.3) can be completely evaluated provided the angle α can be determined. From equation (2.2), however, we can write:

$$\sin\alpha = \frac{\overline{Wa}}{\overline{U}} \qquad (2.4)$$

One can use equation (2.3) and equation (2.4) together to compute the Reynolds stress, since one can directly measure the apparent vertical velocity and the mean horizontal velocity. If the two equations are combined into a single expression, and the small angle approximation is made to order α^2,:

$$\overline{u'w'} = \overline{u'_a w'_a} \left[1-2\left(\frac{\overline{Wa}}{\overline{U}}\right)^2\right] - \frac{\overline{Wa}(\overline{U'a^2} - \overline{w'a^2})}{\overline{U}} \qquad (2.5)$$

For processing of hotwire signals, however, it is more convenient to express the equations directly in terms of the hotwire output signals, rather than the derived expressions. An ideal hotwire would have a cosine law response, where the output signal from the hotwire varies directly as the cosine of the angle between the wind direction and a normal to the hotwire. In reality, however, the hotwire response deviates from the ideal cosinse law response due to the edge cooling of the wire. A better approximation for the directional response of

a hotwire is modified sine-cosine law response of the form:

$$E_o = (V \cos \theta + K V \sin \theta) \qquad (2.6)$$

E_o is the voltage output of the hotwire aenometer, and at this point will be assumed to be a linear function of flow velocity. The non-linearity of the hotwire set putput will be treated separately. V is the free stream velocity, and angle θ is the angle between a normal to the hotwire and the free stream velocity vector. K is an experimentally determined constant characterizing the hotwire response. For the hot film probes used to measure Reynolds stress, K = 0.55.

Consider two hot film probes mounted as shown in figure 2.2. The geometry of the probes is shown in 2.3. From this geometry and from equation (2.6) one can write:

$$V_p = V (\cos (45 + \Theta) + K \sin (45 + \Theta))$$
$$V_s = V (\cos (45 - \Theta) + K \sin (45 - \Theta)) \qquad (2.7)$$

V_p and V_s represents the components of the free stream velocity sensed by hotwires oriented with the wires each normal to the p and s axis, respectively. Also, from figure 2.3:

$$U = V \cos \Theta$$
$$W = -V \sin \Theta \qquad (2.8)$$

Equation (2.7) can be manipulated by expanding the trigonometric functions, and then forming new expressions from the sum and difference of equation (2.7). After evaluating known angles, the result becomes:

$$U = \frac{\sqrt{2}}{2} \frac{V_p + V_s}{1 + K}$$
$$W = \frac{\sqrt{2}}{2} \frac{V_p - V_s}{1-K} \qquad (2.9)$$

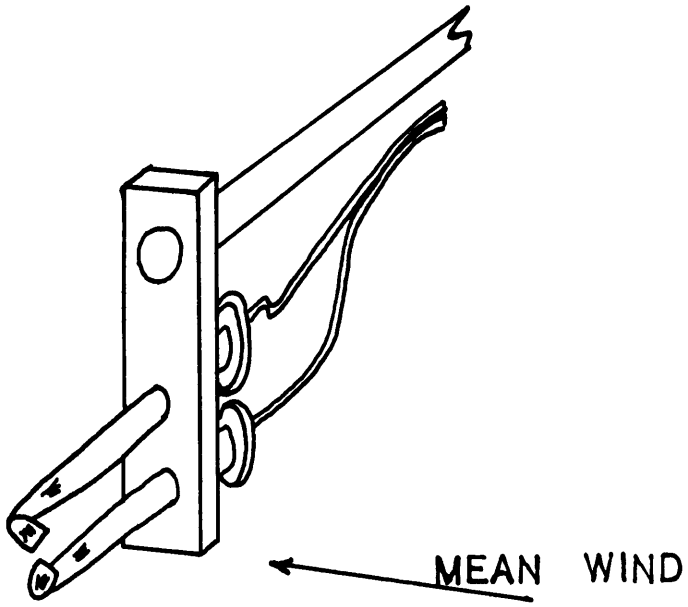

FIGURE 2.2

Sketch of hot film probe arrangement.

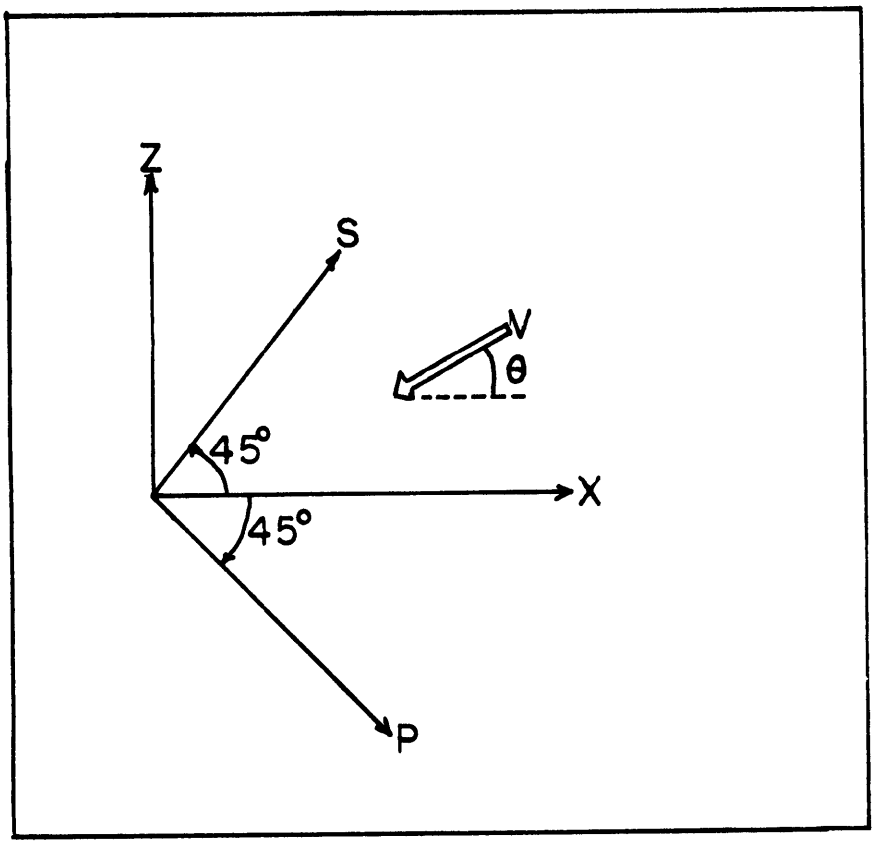

FIGURE 2.3

Geometery of hot film probe arrangement.

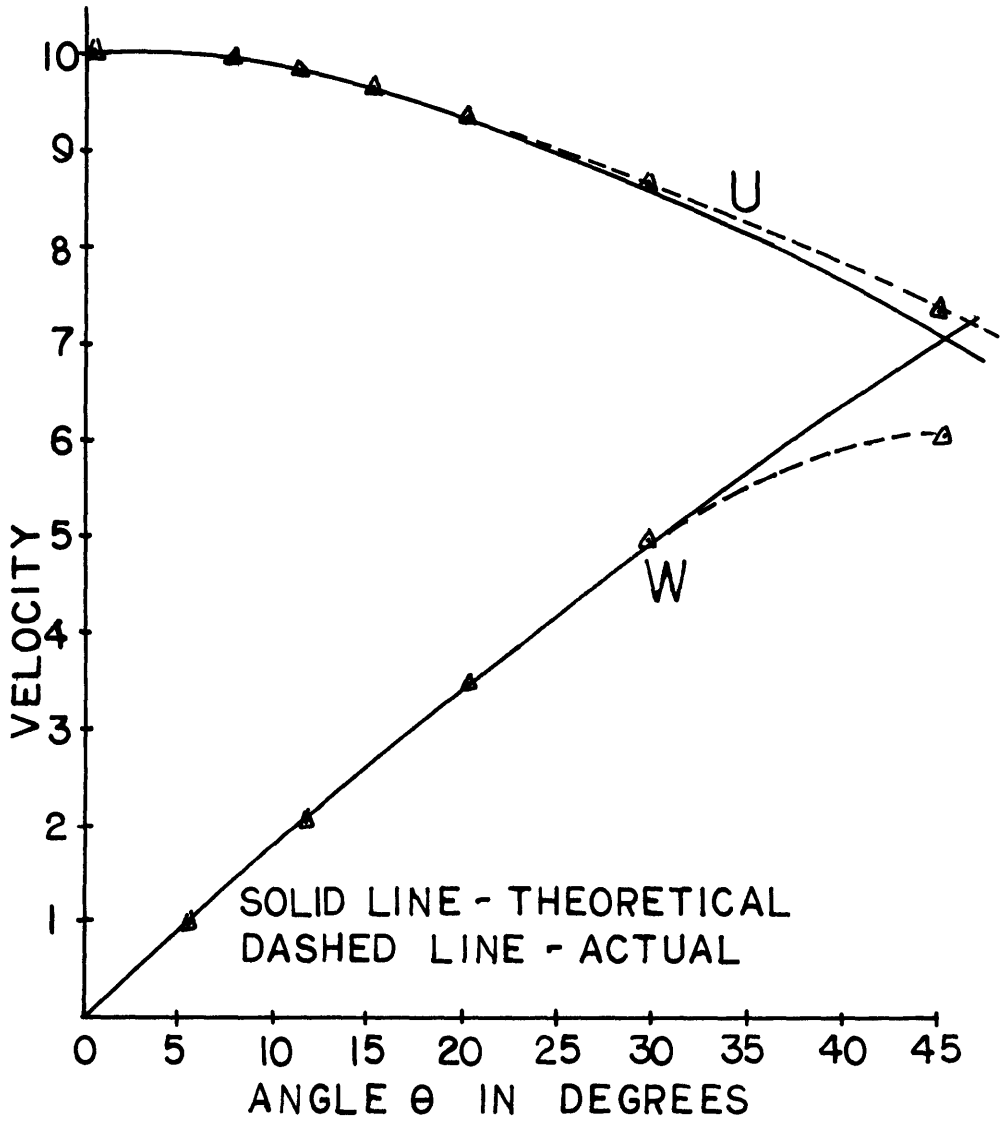

FIGURE 2.4

Orthogonally mounted hot-film probe directional response based on wind tunnel tests.

The response characteristics of a hotwire pair mounted in an orthogonal configuration is shown in figure 2.4. Note that $\overline{U}$ and $\overline{W}$ components are accurately measured within plus or minus 30 degrees of the horizontal. This requires that $|W|<0.6|U|$, a condition which is generally true in the atmosphere since $\overline{W} = 0$ and $\overline{w'^2}$ is at most an order of magnitude smaller than $\overline{U}$.

The probes encompass a field of measurement of roughly one-half centimeter, while the scale of the fluctuations being studied are of order 10 centimeters or greater. Consequently the measurement field of the probes can be considered to be a point. Further, for measurement of mean wind speeds over time intervals of several minutes, one can expect two sensors separated horizontally by a distance of roughly 1 meter to sense the same mean wind speed. Therefore:

$$\overline{V}_p = \overline{V}_s$$
$$\overline{V'^2}_p = \overline{V'^2}_s$$
$$\overline{V}_p + \overline{V}_s = B\overline{V}_c \qquad (2.10)$$

Where V_c is the horizontal mean wind speed as sensed by a cup anemometer located at the same height and in close proximity to the hotwire pair. B is an arbitrary constant of proportionality to be determined. Equation (2.10) says that both probes and the cup anemometer sense the same mean wind, while each of the two probes sense the same mean square turbulent fluctuations. Reconsidering the alignment problem, if the output of the two probes is adjusted to satisfy equation (2.10), then $\overline{W}_a = 0$ and the error terms in equation (2.3) are eliminated.

Given two records of hotwire data from a pair of hotwire sensors mounted for Reynolds stress measurement, the records can be statistically normalized with a mean equal to zero and with a unit standard deviation.

This satisfies equations (2.10) and (2.3). The signals would have an arbitrary calibration, however, and the velocities could not be determined unless B is determined. To determine B we will depend on a mean wind trend within the wind record. Let

$$MV_a = V_p$$
$$MV_b = V_s \qquad (2.11)$$

where M is a velocity calibration constant; V_a and V_b are the values of velocity at any given instant in the two sets of normalized velocity records. From equation (2.10) and equation (2.11) one can write an expression for a record possessing a mean velocity trend. The mean velocity over an arbitrary sub-interval within the record about times t_1 and t_2 can be expressed as:

$$\overline{M(V_a(t_1) + V_b(t_1))} = \overline{BV_c(t_1)}$$
$$\overline{M(V_a(t_2) + V_b(t_2))} = \overline{BV_c(t_2)} \qquad (2.12)$$

Where the two time intervals are non-overlapping, and by virtue of the trend, $V_c(t_1)$ is not equal to $V_c(t_2)$. Adding the two expressions in equation (2.12) and solving for B/M:

$$\frac{B}{M} = \frac{1}{A} = \frac{[\overline{V_a(t_2)} - \overline{V_a(t_1)}] + [\overline{V_b(t_2)} - \overline{V_B(t_1)}]}{[\overline{V_c(t_2)} - \overline{V_c(t_1)}]} \qquad (2.13)$$

This expression can be used to scale U by substituting into equation (2.9) with the result:

$$U = A\ (V_a + V_b) + \overline{V}_c \qquad (2.14)$$

The scaling of the vertical wind component is based on an examination of the following equations, which follow directly from equations (2.9) (2.10) and (2.14):

$$\overline{U'^2} = A^2 \overline{(V'_a + V'_b)^2} = A^2 (2 + 2\overline{V'_a V'_b})$$

$$= N_1^2 \overline{(V'_p + V'_s)^2} = N_1^2 (\overline{2V'^2_p} + \overline{2V'_p V'_s})$$

$$N_1 = \frac{\sqrt{2}}{2(1 + K)} \quad ; \quad N_2 = \frac{\sqrt{2}}{2(1 - K)}$$

$$\overline{W'^2} = N_2^2 \overline{(V_p - V_s)^2} = N_2^2 (\overline{2V'^2_p} - 2\overline{V'_p V'_s})$$

If we multiply out both terms, and substitute an expression for $\overline{U'^2}$ where appearing in W'^2, we can write:

$$\overline{W'^2} = \frac{A^2 N^2 2}{N_1^2} \overline{(V_a - V_b)^2} \qquad (2.15)$$

Finally, expressing N_1 and N_2 in terms of K, the result becomes:

$$W = A\left(\frac{1 + K}{1 - K}\right) (V_a - V_b) \qquad (2.16)$$

This equation, along with (2.14), has been used to solve for U and W using hotwire signals. These equations incorporate corrections for instrument alignment, in-site calibration, and probe response characteristics.

Other instrument errors.

There are three classes of errors which will be discussed next. The first concern, of course, is the non-linear response characteristics of the hotwire anemometer. The usual approach, which was followed during the summer of 1968, is to employ an analog device such as the one described in appendix III to linearize the anemometer output. In retrospect, however, this appraoch was a poor one since it tended to maximize another class or error of concern, i.e., the data transmission and conversion error.

The initial philosophy, based in part on the then existing data analysis techniques, was to linearize the signals in the field before transmission and recording. The justification for doing this was to record and process signals which could be subsequently treated as linear signals by analog data processing systems. As the techniques for hotwire data processing were refined, coupled with a shift from analog to digital processing, it became clear that the problem of linearization needed reexamination.

The basic problem is that while most hotwire anemometers have essentially unlimited dynamic range when used for atmospheric measurements, the data recording and conversion devices have limited dynamic range and limited sensitivity. For example, a 10-bit analog-to-digital converter was used to digitize the signals. The maximum range of this device is plus or minus 512, for a maximum resolution of roughly one part in 1000. If one starts allocating the available range of the digitizer to accommodate the maximum wind gust expected of say 20 meters-sec^{-1}, then for a linear signal the maximum resolution is of the order of .02 meters-sec^{-1}. This is the approximate magnitude of the velocities we wish to resolve. Consequently significant data is degraded or completely lost due to transmission range resolution.

The response of a hotwire is usually expressed:

$$E^2 - E_o^2 = \beta U^{1/2} \qquad (2.17)$$

Where E is the hotwire voltage output, E_o is the no-flow voltage output, β is an instrument characteristic parameter, and U is wind velocity. Note that the hotwire voltage output varies as the fourth root of the

wind velocity. Consequently for low wind velocities the set sensitivity is large and diminishes for higher wind velocities. The characteristic response of the hotwire anemometer therefore provides a signal compression. If the E_o voltage is subtracted from the signal before transmission and recording, one can then utilize the entire channel range for the non-linear signal. After transmission and conversion, the signal can then be linearized in an analog or digital computer, where there is again essentially unlimited range and resolution. The result is a signal with wide dynamic range and with a non-linear resolution. The signal will have high resolution at low wind velocities --- where it is needed --- and poorer resolution at high wind velocities -- where it is of less importance.

Finally, a word about the dynamic response of hot film probes. Rasmussen (1968) has shown that the DISA 55A81 pyrex-backed hot film probe had dynamic response characteristics markedly different from that inferred from static calibration. In view of the unusual geometry of the 55A83 and 55A85 probes, dynamic calibration runs were conducted using the low-turbulence wind tunnel at the Massachusetts Institute of Technology. The results are shown in figure 2.5. The probes have a resonant point at about 1.5 Hz. The response falls off to about 50 percent of the static response at frequencies above 50-100 Hz. The region of interest for atmospheric measurements is the region below 0.5 Hz. In this region, the dynamic characteristics are well approximated by the static calibration of the hot film probes.

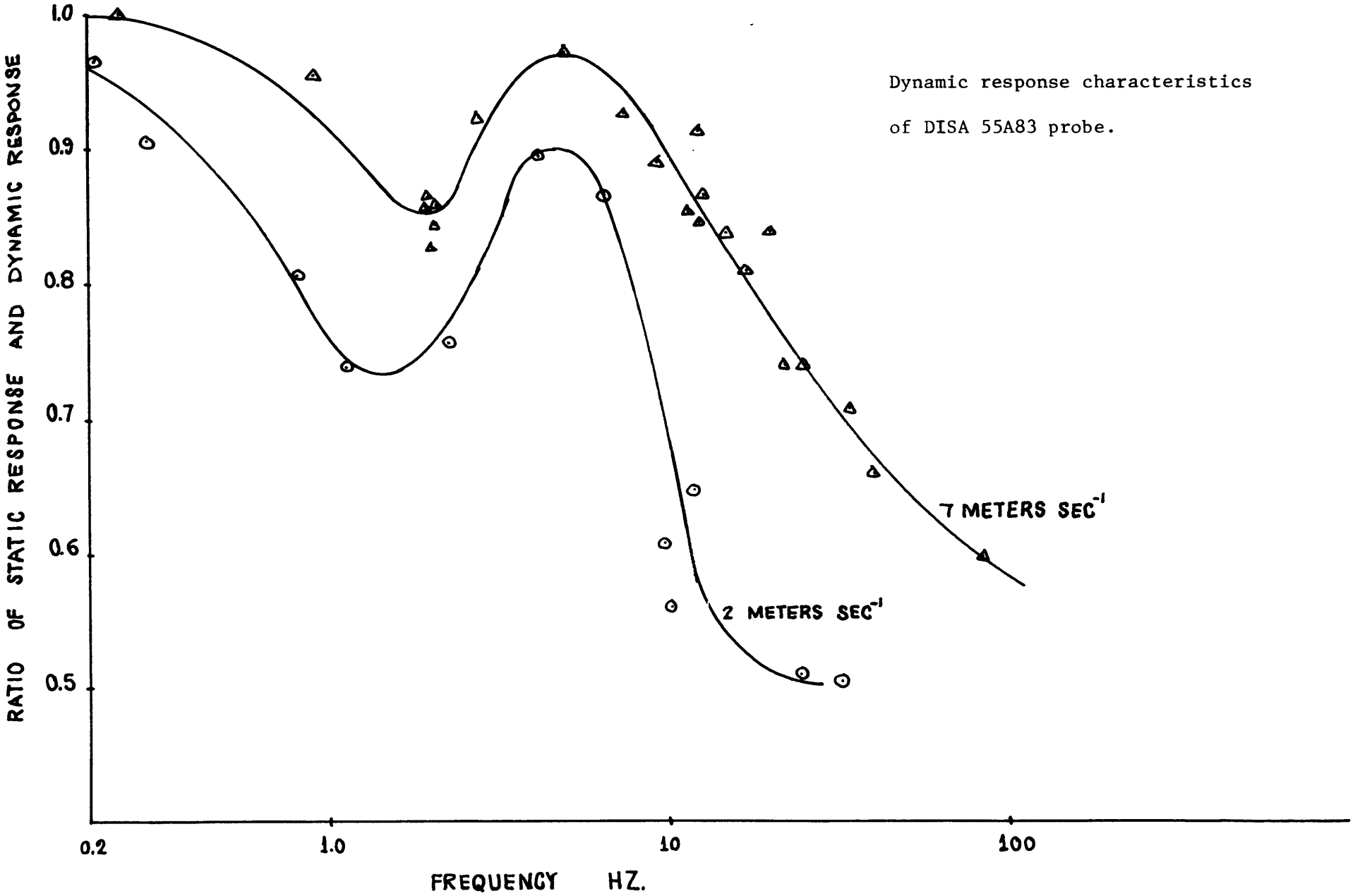

Dynamic response characteristics of DISA 55A83 probe.

Chapter III

The Vertical Mean Wind Profile Over the Ocean For Light to Moderate Winds

The nature of the vertical mean wind profile over the ocean remains one of the central issues in the study of the atmospheric boundary layer over the ocean. Consequently an experimental study has been undertaken in an effort to increase our knowledge of processes in this regime through observation. Over a period of two years, measurements of mean wind speeds at vertically separated stations have been collected by Seesholtz (1968) and this author. This effort has resulted in a data set of 299 mean wind profiles measured in the first ten meters of the atmosphere. The profiles have a distribution as a function of the wind speed at ten meters, taken as the reference height wind speed throughout this report, as shown in figure 3.1. The results of the study are valid in the light to moderate wind speed regime.

Each profile is based on wind speeds measured simultaneously from four to eight anemometer stations. The lowest station was within one meter of the mean sea surface unless sea conditions required otherwise, while the uppermost station varied in position between 8 and 12 meters above the mean sea surface. While instrument configurations varied, in every case the anemometer stations were positioned more or less logarithmically with instruments concentrated within the first few meters above the water's surface. The instruments were attached to a rigid spar standing in 60 feet of water, therefore, the measurements are free of effects such as buoy or ship motion while the behavior of the wind-waves can be

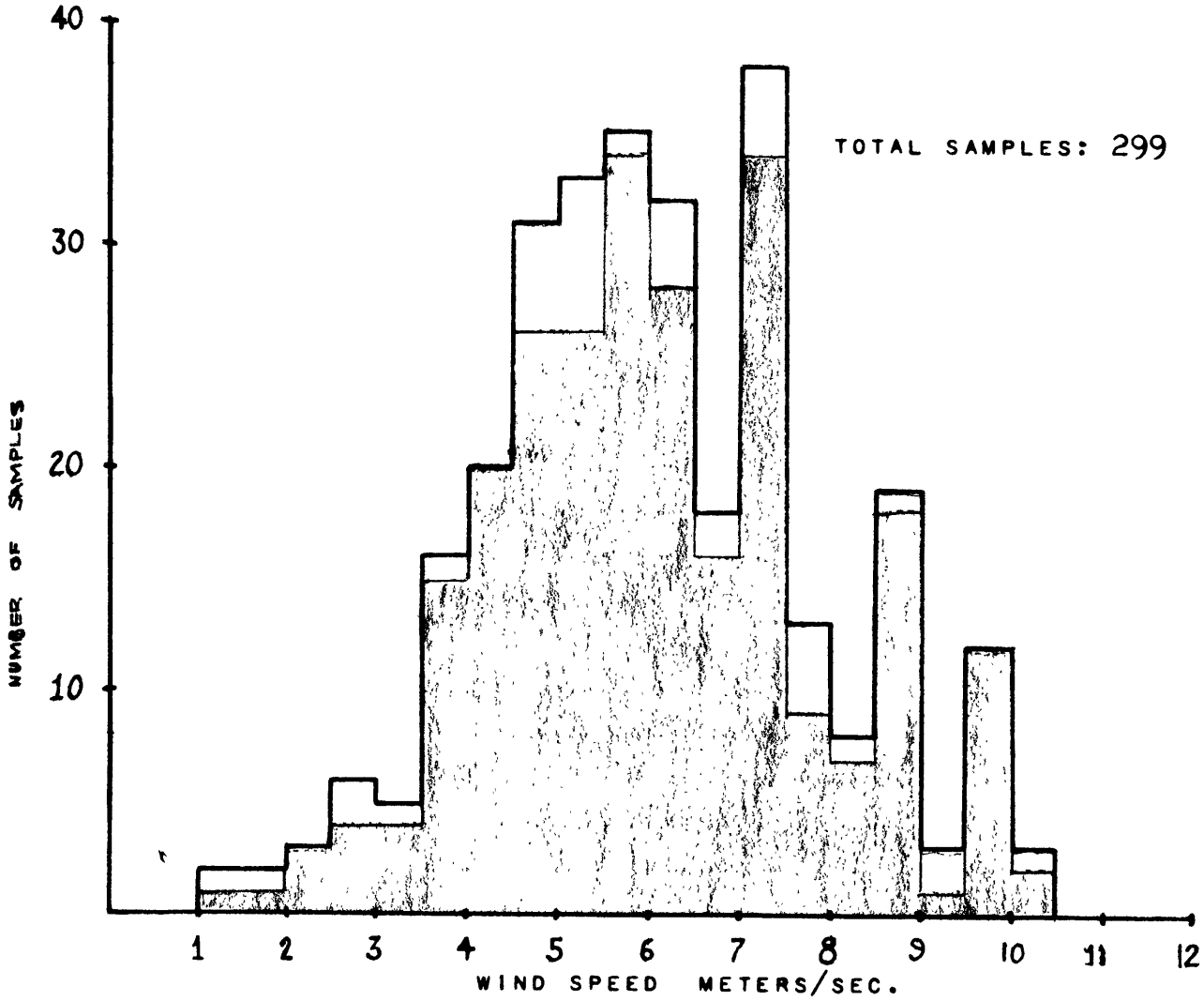

Figure 3.1 Distribution of wind profile samples. Shaded area is distribution of wind profiles with a correlation with a log profile of 0.94 or better.

expected to be that of deep water wind waves. All wind speeds have been averaged over a ten minute interval.

The basis for the analysis and discussion is the logarithmic wind profile, defined as:

$$U(z) = \frac{U_*}{K} \ln\left(\frac{z}{z_o}\right) \qquad (3.1)$$

z_o is the roughness length, defined as that height at which U(z), the mean wind at height z is equal to zero. This parameter is normally thought of as characterizing the effect of boundary on the mean air flow. U_* is the friction velocity, where $U_* = (\overline{u'w'})^{1/2}$. K is von Karman's constant, taken to be equal to 0.42. From an experimental viewpoint, U_* and z_o can be uniquely determined from equation (3.1) provided the profile is in fact logarithmic. These parameters become indeterminate, however, for experimental data representing non-logarithmic profiles unless one has a prior knowledge of the functional form of the profile. Therefore, experimental profiles which are not logarithmic will be discarded. Non-logarithmic profiles can result from a myriad of causes, such as stability changes, a passing ship upwind of the observation station, etc. Aside from the indeterminancy problem, discarding anomalous profiles excludes extraneous information which might otherwise bias the results and their subsequent interpretation. Fortunately, while valid cases of non-logarithmic profiles exist over the ocean, they are the anomaly. In this study, thirteen percent of the data sample has been discarded. Of that 13 percent, better than half of the cases can be discarded on valid physical grounds. Therefore, better than 90 percent

of the valid measured profiles are logarithmic, as shown in the shaded areas of figure 3.1.

Equation (3.1) is linear in $\ell n(z)$, and can be written:

$$\ell nz = \frac{K}{U_*} U(z) + \ell nz_o \qquad (3.2)$$

One can use linear regression techniques to find the best least-squares fit of the assumed profile form to the observed data. Following Hoel (1954, p 127), equation (3.2) can be written in terms of the observed wind speed V at instrument height Y_i:

$$\ell nz - \overline{(\ell nY_i)} = \frac{\overline{V(Y_i)\ell nY_i} - (\overline{\ell nY_i})(\overline{V\ (Y_i)})}{\overline{V(Y_i)^2} - \overline{V(Y_i)}^2} \; U(z) - \overline{V(Y_i)} \qquad (3.3)$$

The overbar represents an ensemble mean, while N is the number of profile points measured for each profile. The ensemble mean is defined in the usual sense for discrete data:

$$\overline{f} = \frac{1}{N} \sum_{I=1}^{N} f_i$$

From equation (3.3) the equation of the line best fitting the profile is determined. From this line, U_* and z_o can be directly computed, along with a linear correlation coefficient:

$$r = \frac{\overline{V(Y_i)\ln Y} - (\overline{\ln Y_i})\ (\overline{V(Y_i)})}{[(\overline{\ln Y_i})^2 - (\overline{\ln Y_i})^2]\ [\overline{V^2(Y_i)} - \overline{V(Y_i)}^2]^{1/2}} \qquad (3.4)$$

These correlation coefficients measure how well the logarithmic profile form represents the observed profile. Detailed information for each profile is presented in Appendix I. Those examining this appendix will note that U_* has been computed for several heights, and does not always appear as a constant with height. This variation is because the $U_*(z)$ displayed in appendix I is computed from equation (3.2) using the observed wind at height z, instead of the computed profile wind. The ten meter reference U_*, however, in all cases is the profile value.

Table 3.1 lists the distribution of correlation coefficients computed from each of the observed mean wind profiles. A correlation coefficient of 0.94 has been chosen as the division point between those profiles defined as logarithmic and those profiles discarded as deviating from the logarithmic form. The shaded region of figure 3.1 represents the distribution of the logarithmic wind profiles after the anomalous profiles had been discarded. Note that those profiles taken to be logarithmic are distributed as a function of 10 meter wind speed roughly the same as the distribution of the total sample. Each of the discarded profiles were individually examined, with the following results:

A. Of the four profiles with correlation coefficients less than 0.74, three were measured during a time period when the mean wind speed suddenly increased at the upper levels during the averaging period.

TABLE I

Correlation Coefficient	NR. Samples
1.00	86
.980 to 1.00	106
.950 to .980	59
.920 to .950	26
.890 to .920	11
.860 to .890	02
.830 to .860	03
.800 to .830	02
.740 to .800	00
.700 to .740	04

The fourth profile could not be classified due to insufficient supplementary information.

B. The profiles with correlation coefficients between 0.94 and 0.80 consists of 19 profiles measured during experiments with artificial sea-slicks. These are not considered representative of a true marine environment. The remaining cases, though not attributed to any identifiable cause, were characterized by intermittency. That is to say for a set of consecutive profiles, there would be one or two anomalous profiles dispersed among an otherwise fully logarithmic set.

After the profiles were computed and sorted those profiles defined as logarithmic were grouped into classes according to ten-meter wind speed. While the data was computed for a number of class intervals, a class interval of 50cm/sec^{-1} was chosen as optimum for displaying the data. A broader class interval retains the gross features, but tends to smear the detail. Narrower class intervals result in a discontinous histogram. The class boundaries fall on the integral wind speed value and the one-half meter/sec^{-1} values of reference wind speed. An observed wind speed which fell exactly on the boundary was grouped with the higher adjacent class. The data in each class was used to compute a mean friction velocity and roughness length appropriate for the class.

The roughness length as a function of reference mean wind speed is shown in figure 3.2. The structure of this parameter was quite unanticipated. The first appearance of this structure resulted in extensive

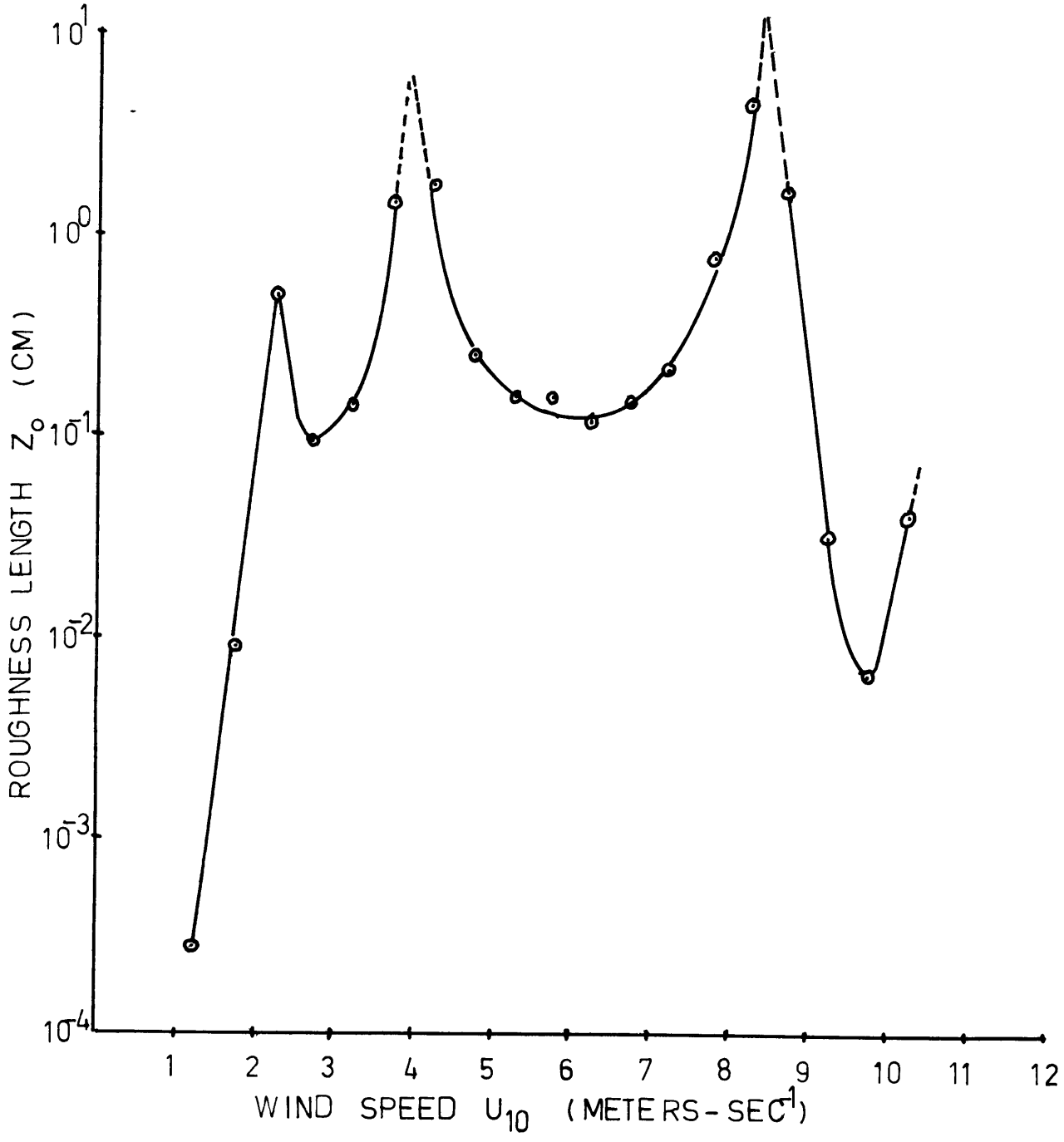

Figure 3.2 Roughness length of a function of 10 meter wind speed.

recomputation, however the features persisted. Wu (1969) recently has published a paper with data processed in a somewhat similar fashion. While Wu did not take note of it, his roughness length plot shows peaks similar to those in figure 3.2 at 4 and 8 meters/sec^{-1}. Wu's graphs were drawn without any data discrimination and for wider class intervals, therefore, the peaks did not stand out as markedly as they do in figure 3.2. Additional corroborating evidence of an indirect kind is provided by Kinsman's (1968) review of the Beaufort wind scale. The scale is shown in figure 3.5. Note that the natural wind speed division points selected on the basis of the appearance of the sea surface to seamen coincides closely with the peaks in the roughness length graph.

On the basis that marked changes in roughness length characterize a change in the condition of the underlying surface as seen by the atmosphere, one can speculate on the significance of each of the peaks. If an air stream was introduced over a perfectly calm sea, and then the wind velocity was slowly increased, there should exist some velocity at which the first wind-waves will appear. Below this velocity the atmosphere should be expected to see a smooth aerodynamic boundary. Above this velocity, the atmosphere should feel a boundary with different aerodynamic characteristics. In figure 3.2 such a change occurs at 2 meters/sec^{-1}, suggesting this as the minimum wave generating wind speed. This velocity is equivalent to a one meter wind speed of 1.5 meters/sec^{-1}, and is in close agreement with Jefferys' minimum wind speed for wind generation as discussed in Lamb (1932, p 625).

The roughness length peak at 4 meters/ sec^{-1} cannot be explained. To the knowledge of the author, there isn't any theoretical work which could be used as a basis for explaining this peak. A tentative physical

explanation will be suggested later based on an analysis of the velocity defect graph, figure 3.5. The marked peak at 8.5 meters/sec^{-1}, however, is reminiscent of the widely discussed Kelvin-Helmholtz shear instability, predicted by Munk (1947) to occur at 6 meters/sec^{-1}. The higher observed wind velocity for the onset of the shear instability is attributed to the modification of the surface tension of the sea water due to dissolved sea salts and contaminants.

Friction velocity as a function of reference wind speed (figure 3.3) shows a strong linear dependence upon velocity. For the 0-10 meter/sec^{-1} speed range, the friction velocity can be approximated by the formula:

$$U_* = .04U(10) \qquad (3.5)$$

Note that the friction velocity plot shows only minor deviations from its trend in the vicinity of 2 and 4 meter/sec^{-1}. At 8.5 meters/sec^{-1}, however, the friction velocity appears to be strongly influenced by the same processes which effect the roughness length parameter. This strong effect is again what one might expect in the case of the Kelvin-Helmholtz instability, where the boundary instability changes the character of the entire turbulent regime.

The drag coefficient at height Z is defined:

$$C_D(z) = \left(\frac{U*}{U(z)}\right)^2 \qquad (3.6)$$

The plot of the drag coefficient is displayed in figure 3.4. Again, the singularities are clearly evident, as is the constant drag coefficient of 1.6×10^{-3} between singularities. The behavior of the drag coefficient in the vicinity of the singularities is typical also of the behavior of the values of the friction velocity. This wide deviation

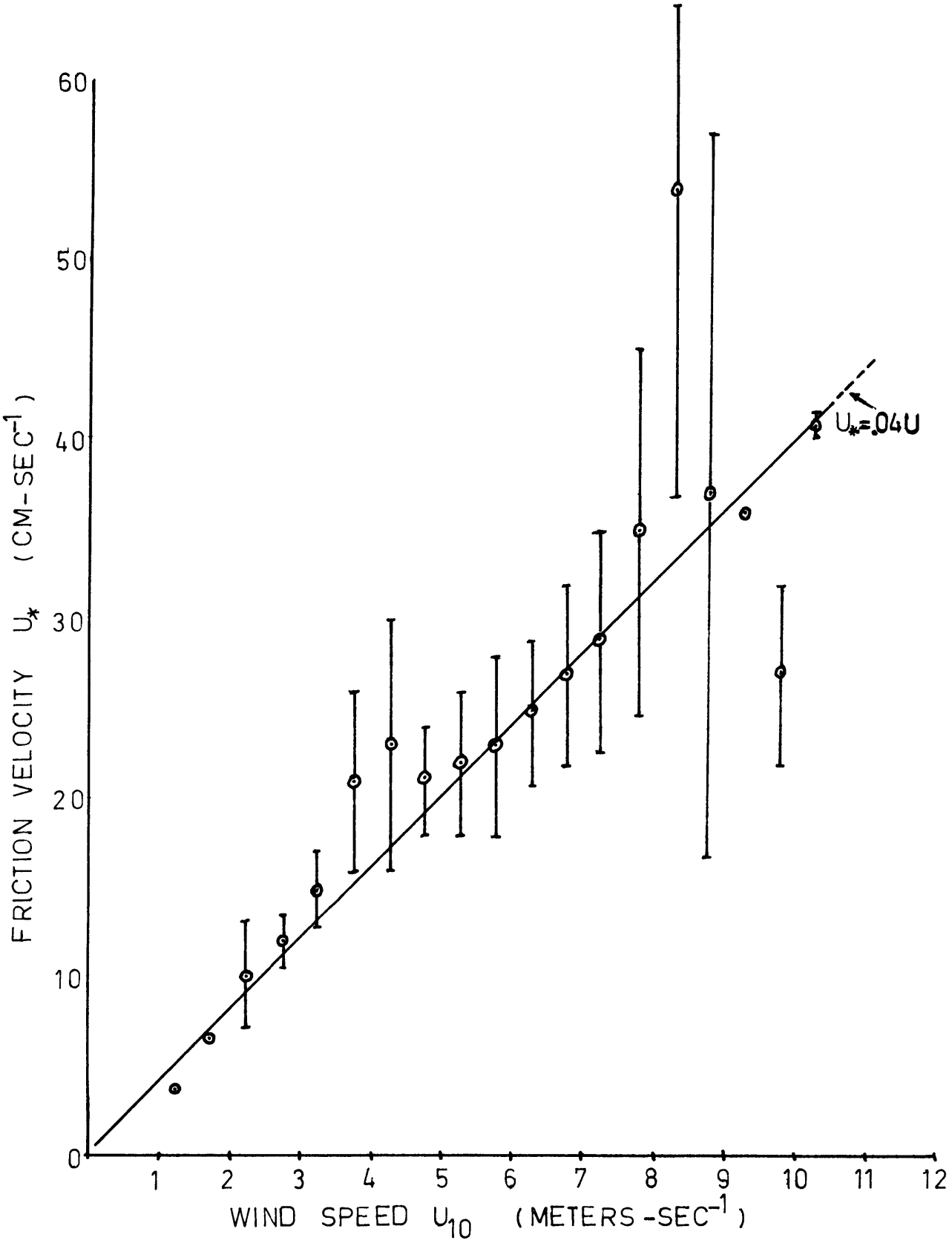

Figure 3.3 Friction velocity as a function of 10 meter wind speed.

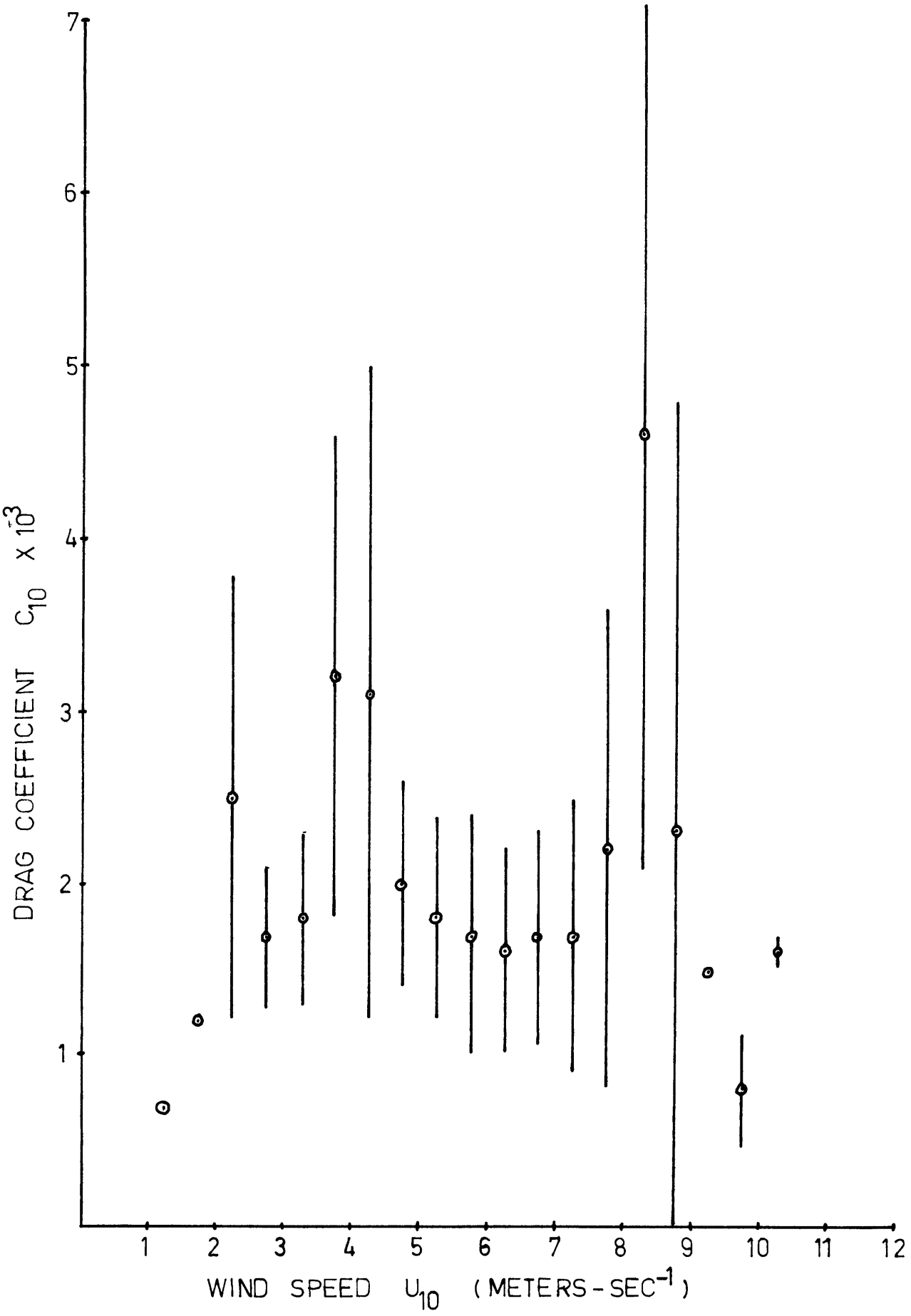

Figure 3.4 Drag coefficient as a function of 10 meter wind speed.

at the singularities suggests that the variables have a modal structure within the class interval. This is what one would expect for sharp discontinuities. Such a structure would result in a mean for the class interval lying somewhere between the two modes of the variable, and extremely large and somewhat meaningless variance value. The functional dependence of the drag coefficient on wind velocity has been a matter of extensive debate, based and scattered data. The results presented here suggest that the inferred functional dependence of the drag coefficient would depend more on how fast the wind was blowing during the various investigator's measurements or how the data was grouped, than on any physical relationship. The value of 1.6×10^{-3} for the drag coefficient agrees with laboratory values of the drag coefficient determined by eddy correlation techniques as summarized by Roll (1965, p 158) and the values measured in the field using eddy correlation techniques reported by Weiler and Burling (1967).

The computed mean values of U_* and Z_o for each class interval were used in equation (3.1) to compute a mean 10 meter wind speed for each velocity class. It was expected that the computed speed would closely approximate the specified mean wind speed for the class. In most cases, however, this computation resulted in a consistent underestimate of the wind speed appropriate for the class. The magnitude of this underestimate is shown in figure 3.5. Since we have been processing the data using statistical approaches, this result should be interpreted from a statistical viewpoint. The implicit assumption in equation (3.1) is that U_* and Z_o are each independent parameters required to describe the flow. If, however, they are not statistically independent,

the mean profile form can be expected to deviate from that inferred from equation (3.1) by the amount of correlation between U_* and z_o. We will represent U_* and z_o as the sum of mean quantity and a deviation from the mean:

$$U_* = \overline{U}_* + U_*'$$

$$\ln \frac{z}{z_o} = \overline{(\ln \frac{z}{z_o})} + (\ln \frac{z}{z_o})' \qquad (3.7)$$

Equation (3.7) is substituted into equation (3.1) and an ensemble mean is taken. The results are:

$$\overline{U}(z) = \frac{1}{k} U_* \overline{(\ln \frac{z}{z_o})} + \overline{\frac{1}{k} U_*' (\ln \frac{z}{z_o})'} \qquad (3.8)$$

Note that this is not the same type of averaging process as is done in the familiar Reynolds convection. In this case we are averaging over an ensemble defined by all those values of U_* and z_o which fall within a specified class interval, rather than over an arbitrary time period. Equation (3.8) therefore indicates that for any given class of wind profile data, the mean wind speed at a height z can be represented as the sum of a mean profile component and a term representing the correlation between U_* and z_o. For wind flow over a rigid boundary, where the nature of the surface is indpendent of the flow parameters, the correlation term can be expected to go to zero and equation (3.8) reverts to the familiar logarithmic profile. We can interpret the first term on the right hand side of equation (3.8) as representing the mean velocity at any height required to support atmospheric dynamics, while the second term identifies profile modification due to external effects. In view of the data screening, the effects of errors in determining the profile descriptors should be expected to be random, rather than systematic

in the fashion shown in figure 3.5. Similarly, atmospheric stability variations are expected to be random in nature, and should not contribute to the correlation term. Richardson numbers were computed as instrumentation permitted, and indicated near-neutral stability conditions in the lower levels of the atmosphere over the ocean. Therefore the second term on the right hand side of equation (3.8) is taken to represent the wind at any height required to support air-sea interaction dynamics. For simplicity, we will write equation (3.8) as:

$$U = U_p + U_w \qquad (3.9)$$

Where U_p is the profile component of the mean wind, and U_w is the boundary interaction component of the mean wind. U_p is always a positive quantity however as shown in figure 3.5, U_w takes on both positive and negative values, with a transition at about 2 meters/sec^{-1}. Given the mean parameters of $\overline{z}_o$ and $\overline{U}*$, the resulting momentum U_p at any level z is all that is required to effect a balance between the momentum created at some higher level and the momentum transferred or lost due to friction. The additional momentum, U_w, represents either the excess or deficit of momentum, where the positive sign indicates excess, available at level z to support the modification of the boundary characteristics. Figure 3.5 indicates that at wind speeds greater than 2 meters/ sec^{-1} in the mean there is an excess of momentum in the atmosphere available for wave generation and maintenance. At wind speeds less than 2 meters/sec^{-1}, in the mean the atmosphere does not appear to have adequate momentum to support frictional losses, and receives momentum from the ocean, presumably from the underlying

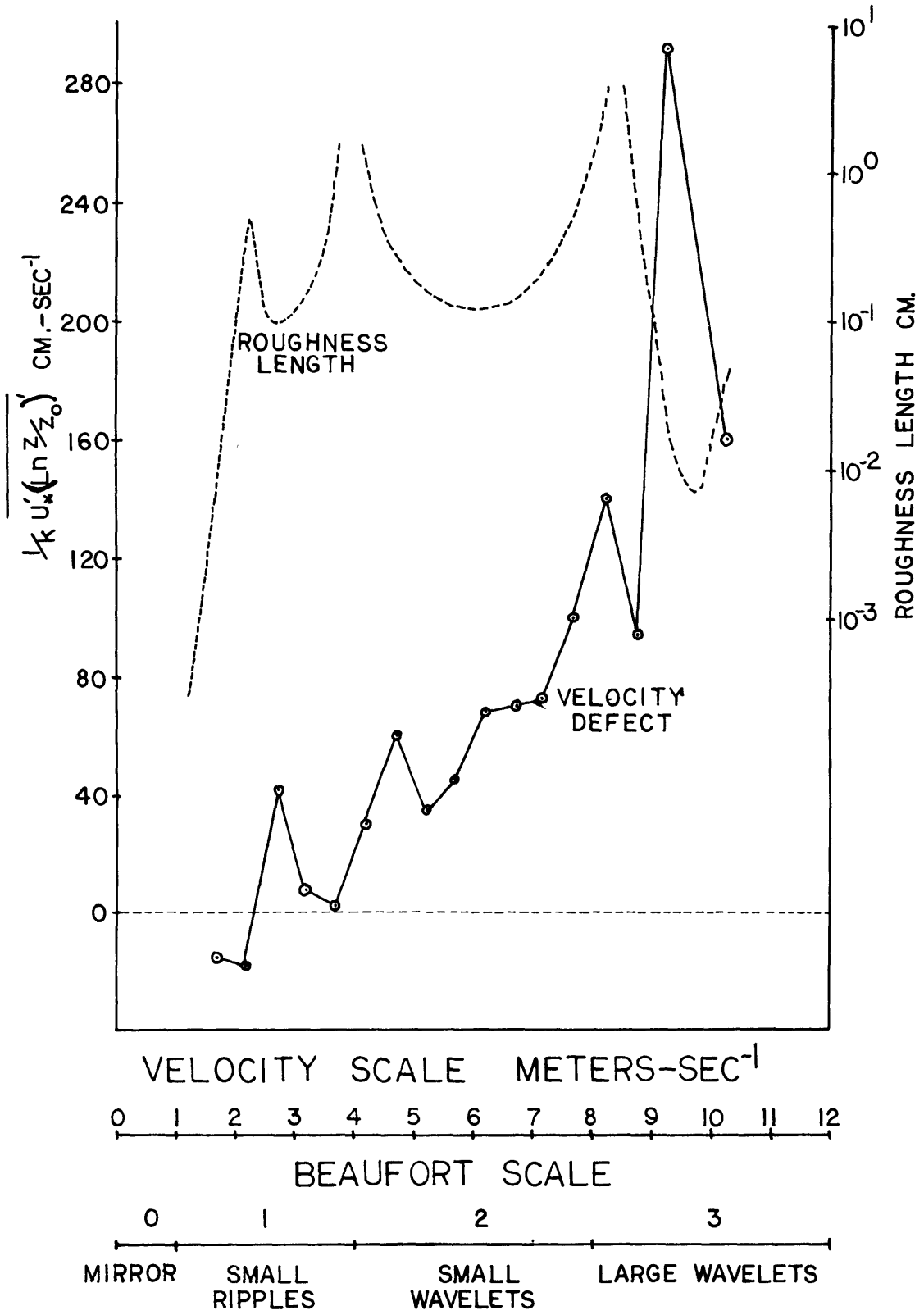

Figure 3.5 Velocity defect (U_w) and roughness length plotted as a function of (a) ten meter wind speed; (b) the Beaufort wind scale.

swell. This interpretation is consistent with and reinforces the view that there is a minimum wave generation wind speed at about 2 meters/sec^{-1}. Above 4 meters/sec^{-1} the ratio of U_w/U varies between 0.1 and 0.2. This ratio is consistent with the ratio of wave growth momentum to the total atmospheric momentum determined by Stewart (1961).

Conclusions.

Charnock (1955) suggested z_o should be proportional to U_*^2/g resulting the wind profile formula:

$$U(z) = \frac{U_*}{k} \ln \frac{\beta z}{(\frac{U_*}{g})^2} \qquad (3.10)$$

β is a constant of proportionality. Inspection of figure 3.2 clearly shows that z_o does not vary as U_*^2. Laboratory experiments by Wu (1968) resulted in similar findings, however Wu noted that the Charnock expression is appropriate at high wind speeds. This expression implicity assumes that a single surface roughness parameter will specify both the momentum balance requirements of the ocean and the atmosphere. There is no reason for this to be so. It is suggested that a more appropriate approach is the separation of the profile into two components, a component resulting from atmospheric dynamics and one resulting from wind wave interaction, similar to that done in equation (3.9).

At low wind speeds, the vertical mean wind profile parameters are all functions of velocity, with the roughness length parameter being highly structured. Two of the three peaks in the roughness length graph can be explained by recourse to classical hydrodynamics. The peak at 4 meter/sec^{-1} requires explanation. The rise and then the return to

a near zero value of the velocity defect in figure 3.5 at 4 meter/sec^{-1}, taken along with the roughness length plot suggests to this author that the peak at 4 meter/sec^{-1} may be associated with a transition from capillary waves to gravity waves as those waves having a dominant effect on the atmosphere. The evidence is far too meager and the arguement far too tenuous, however, to make this assertion with any firm conviction.

Chapter IV

Small-Scale Atmospheric Processes Just Above the Sea Surface

General

Current theory describing the momentum transfer processes at the air-sea boundary require specific behavior of the atmosphere before momentum interchange can occur. A continuing controversy exists over the validity of the theory, based on the critical appraisal of the assumptions about the atmosphere directly above the water surface. Resolution of the controversy lies in observation of the actual behavior of the atmosphere above the ocean surface. This chapter provides some observations in this regime.

Background

The wave generation mechanism proposed by Phillips (1957) relies on the advection of turbulent eddies over the sea surface to induce a resonant response at the ocean surface, resulting in the growth of wind-waves. Application of this theory requires a statement about how eddies are advected across the water surface. The theory uses the concepts of a dominant eddy convection velocity and an integral time scale of the turbulence in a convected frame. The theory describes the initial excitation of waves by turbulent air pressures which are not affected by wave motions. As soon as the waves start affecting the air motions, feedback coupling occurs, which is described by Miles' (1957) theory. This theory predicts exponential wave growth caused by a vorticity interchange across a "critical level", defined as that level where $\bar{U}(z)$, the mean wind speed at height z, is equal to C, the phase speed of the growing wave.

The rate of momentum transfer is proportional to

$$M \approx \frac{\rho_a}{4} \left(\partial^2 \bar{U}/\partial z^2\right)/(\partial U/\partial z) \quad \overline{w'^2} \tag{4.1}$$

ρ_a is the density of air, while w is the vertical velocity. All quantities in equation (4.1) are evaluated at the critical level. Application of the Miles theory requires an assumption about the constancy of the vertical mean wind profile and the magnitude of $\overline{w'^2}$. The constancy of the mean wind profile appears valid as discussed in chapter III. The value of $\overline{w'^2}$ is usually taken to be equal to the mean square amplitude of the growing wave. This infers a coupling between wind and wave, where the motion of the wind above the wave is identically equal to that of the wave.

Measurements of wave growth by Snyder and Cox (1966) and Barnett and Wilkerson (1967) indicate the theoretical wave growth is insufficient to account for observed wave growth. Measurements by Seesholtz (1968), however, result in reasonable estimates of wave growth using Miles' theory. In his results, Seesholtz demonstrated that wave-growth computations are quite sensitive to accurate profile measurements and that one must use mean wind speeds averaged over a short period of time.

Stewart (1967) argues using wind spectra that waves do not induce fluctuations in the atmosphere of the order assumed by Miles of the $\overline{w'^2}$ term in equation (4.1). Stewart's arguments lose force, however, due to the wide bandwidth of his spectral estimates and the lack of information about smoothing techniques employed. Hanning the spectrum, for

example, could spread the observed wave energy into adjacent bands, causing the observed low power at the wind-wave band. Weiler and Burling (1967) published spectra with narrower bandwidths. These spectra show considerable energy in the region of the typical wave frequencies; however, sharp peaks were not observed.

Some of the failure to observe wave energy in spectral density plots of atmospheric turbulence may be due to the method of representing the spectrum. To illustrate, let us examine a highly structured spectrum. Figure 4.1 shows two plots of an ocean surface wave spectrum, specifically chosen because of the dominant peaks in the spectrum. Figure 4.1(a) is a linear plot of the wave spectrum, while figure 4.1(b) is a plot of $f\phi(f)$ versus $\ell n\ f$, as spectra usually are represented in atmospheric studies. Figure 4.1(a) indicates a dominant near-monotonic swell. Examining figure 4.1(b), however, one would tend to conclude only that there is considerable energy in the region of typical swell frequencies. One does not clearly observe the sharp peak and the nature of the swell. Small detail is lost in the plot. In order to emphasize small features in the spectrum, all spectral density plots are presented herein with linear frequency scales. This is easily accomplished since only a narrow portion of the atmospheric frequency domain is presented.

Taylor Hypothesis

The Taylor, or "Frozen Turbulence" hypothesis relates the time and space scales of turbulence. This hypothesis postulates that if the mean wind speed were high enough, the turbulence would remain unchanged as it is being convected past a point, such that:

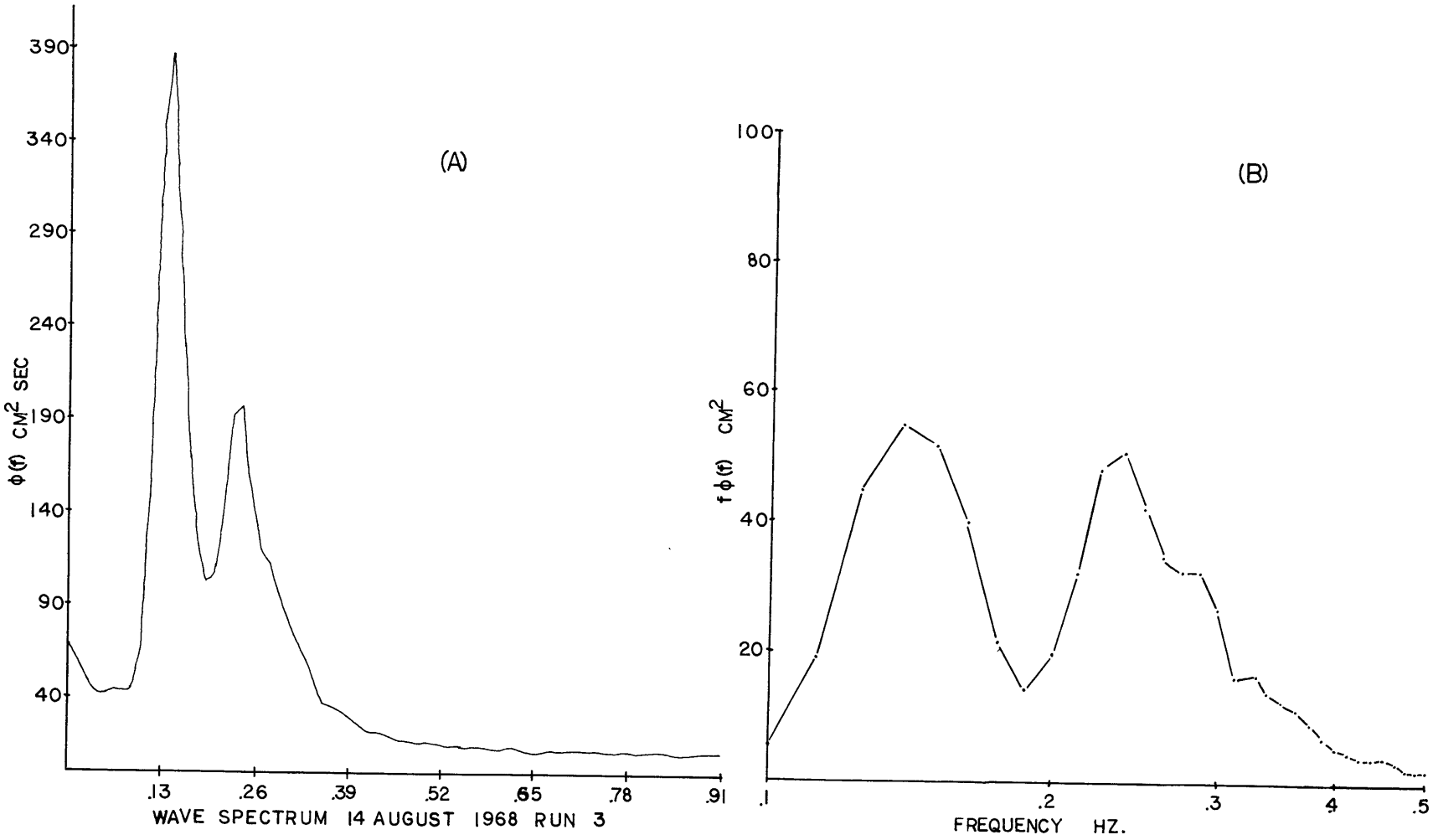

Figure 4.1 Comparison of plots of wave energy.

$$f = \frac{Uk}{2\pi} \tag{4.2}$$

k denotes the wave number, U is the velocity of the mean air stream, and f is the frequency of the eddies measured at a point. In a shear flow, however, the Taylor hypothesis is expected to hold only for eddies of such size that: [see Lumley and Panofsky (1964 pg. 57)]:

$$\left|\frac{\partial \bar{U}}{\partial z}\right| << k\bar{U} \tag{4.3}$$

If we differentiate equation (3.1), and combine the result with equations (4.2) and (4.3), the minimum frequency for which Taylor's hypothesis is expected to hold can be expressed as:

$$f >> \frac{U_*}{2\pi\kappa z} \tag{4.4}$$

where κ is Von Karman's constant.

Taylor's hypothesis has been repeatedly confirmed over land, as summarized by Monin (1967), resulting in its wide application over land and sea. The validity of the Taylor hypothesis in the frequency domain of wind waves has not been confirmed. In fact, the characteristic cats-eye pattern of the Miles wave-generation mechanism as described by Lighthill (1962) suggests that the atmospheric eddies would move coupled with the wind wave, rather than convected along by the mean wind.

To measure the validity of Taylor's hypothesis, consider two wind measuring devices separated by a distance ζ, and oriented such that they both lie on the same mean wind streamline. The average time τ for

eddies to travel the distance ζ can be determined from the correlation:

$$R_{uu}(\tau) = \langle U(x,t),\ U(x+\zeta,\ t+\tau)\rangle \tag{4.5}$$

If τ_a is that delay time when R_{uu} is a maximum, one can compute a correlation velocity U_R:

$$U_R = \frac{\zeta}{\tau_a} \tag{4.6}$$

For Taylor's Hypothesis to be valid, $U_R = \bar{U}$. Table 4.1 lists the mean wind speed for two elevations measured by cup anemometers, along with U_R as measured by hot film anemometers and determined from Equation (4.6). Note that U_R does not in general equal U. Further, there does not appear to be any pattern between the convected velocity and the ratio $U_*/2\pi\kappa z$.

For one day, the data allowed a more detailed analysis of the convected velocities. Equation (4.5) can be fourier transformed into the cross spectral density function, S(f), where:

$$S_{u_1u_2}(f) = 2\int_{-\infty}^{\infty} R_{u_1u_2}(\tau)e^{-i2\pi f\tau}\,d\tau \tag{4.7}$$

$S_{u_1u_2}(f)$ is a complex number and can be represented in complex polar form with the absolute value of $S_{u_1u_2}(f)$ and a phase angle $\phi(f)$. This phase angle is related to sensor separation and the wavelength λ of the ratio:

$$\frac{\phi(f)}{\zeta} = \frac{2\pi}{\lambda} \tag{4.8}$$

TABLE 4.1

Check of Taylor's Hypothesis

Date	Z = 1 meter			Z = 5 meters			Conditions
	$\frac{U_*}{2\pi KZ}$	U_R	$\overline{U}$	$\frac{U_*}{2\pi KZ}$	U_R	$\overline{U}$	
3 Aug 68	.110	4.0 ± .5	3.8	.021	5.0 ± .5	4.8	NG
6 Aug 68 Run 1	.110	4.0 ± .5	5.5	.021	4.5 ± .5	6.8	G
6 Aug 68 Run 2	.099	3.5 ± .5	5.0	.020	3.5 ± .5	6.0	NG
5 Aug 68	.175	2.0 ± .5	5.0	.035	4.5 ± .5	7.0	G
9 Aug 68	.110	3.9 ± .2	5.4	.021	4.7 ± .2	6.5	G

G = wind wave generating conditions

NG = non-generating conditions

From Equation (4.2) the convected velocity can be expressed

$$U_R(f) = \frac{2\pi f\zeta}{\phi(f)} \tag{4.9}$$

In practice $\phi(f)$ is measured only for values varying from 0 to 2π. For $\lambda < \zeta$, however, the true phase angle has a value equal to $\phi(f) + 2N\pi$. The criteria for determining the sensor separation, ζ, did not foresee spectral computations. Consequently the value of ζ = 20 meters is too large and has resulted in the $2N\pi$ ambiguity. This ambiguity has been arbitrarily resolved by selecting that value of U_R nearest to the mean wind speed $\bar{U}$, consistent with adjacent spectral values. In general, the correct value of U_R was clearly evident.

Figures 4.2 and 4.3 are two plots taken on the same day, where U_R has been computed using equation (4.9) and plotted as a function of frequency. Both figures display the spectrum of the ocean wave field appropriate for the measurement period; the measured mean wind speed for the appropriate heights; and the phase and group velocity for the underlying ocean waves. The values used to construct figure 4.2 were measured under calm, stable conditions. A heavy fog bank shrouded the measurement site and the ocean for a radius of at least 15 miles. Visibility at the site varied between 50-150 feet. $U_*/2\pi\kappa z$ = .072 for 1 meter, .014 for a height of five meters. Figure 4.3, measured during the afternoon of the same day, was measured during strong wind-wave generating conditions. During this period, the sky was clear with unlimited visibility and estimated near-neutral stability conditions. $U_*/2\pi\kappa z$ = .11 for 1 meter, .021 for five meters. The spectral bandwidth in both figures is .05 Hz, the

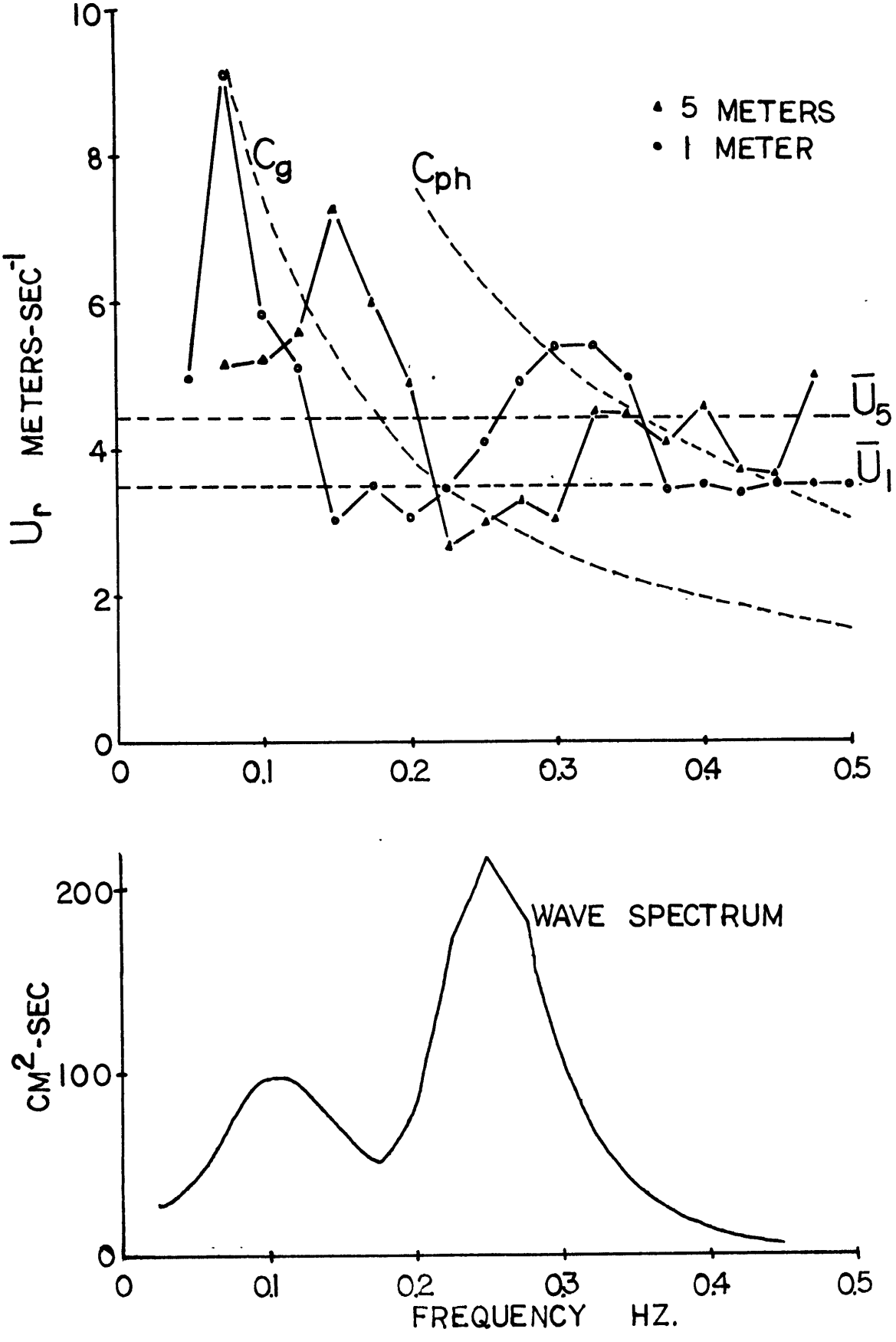

Figure 4.2

Convected velocity during non-generating conditions

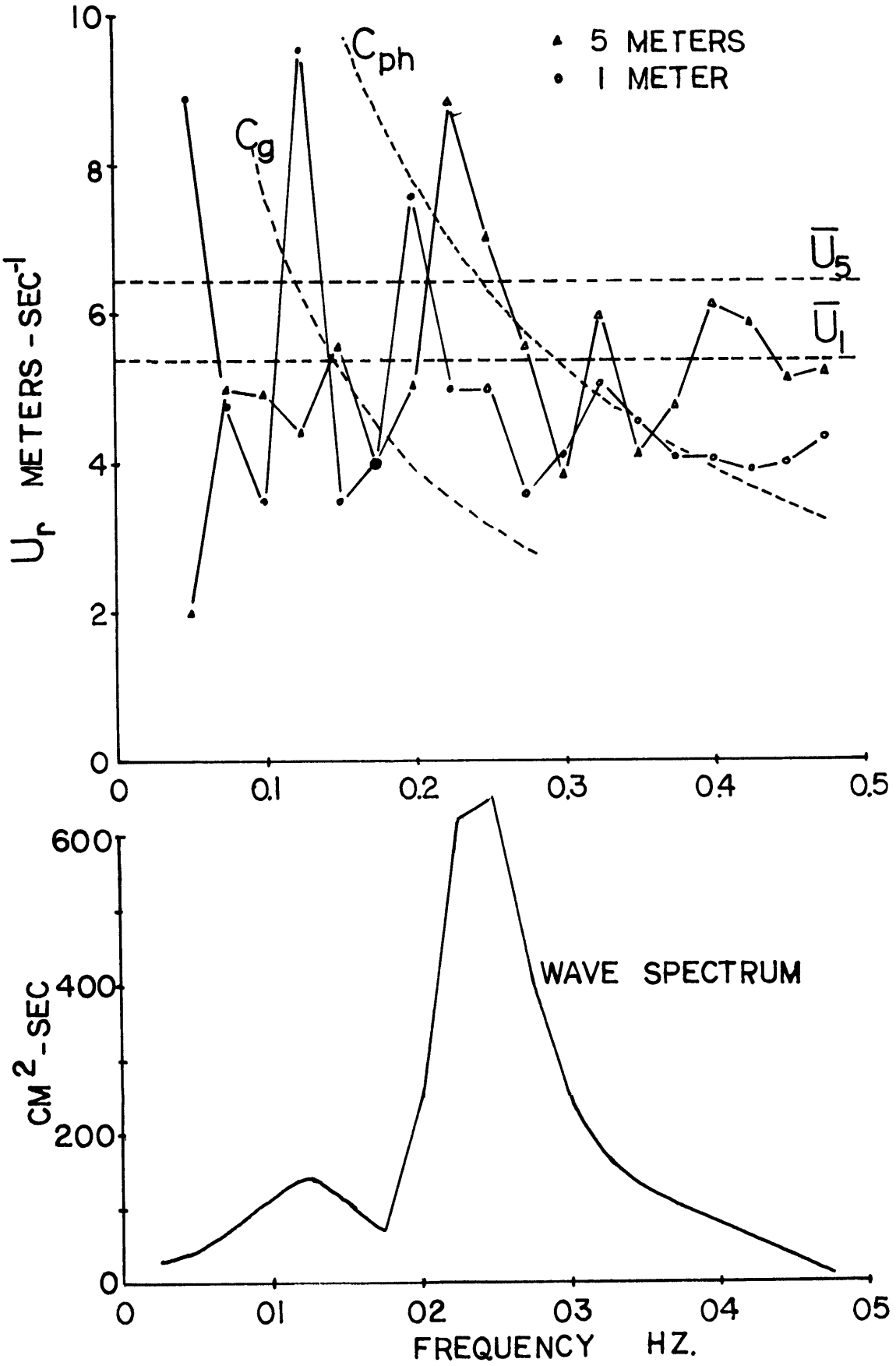

Figure 4.3

Convected velocity during wave-generation conditions

standard error of estimate is .075 with 195 degrees of freedom.

Examining the two cases, in the non-generating case (figure 4.2) those eddies corresponding to the frequency of the dominant waves appear to travel faster than the same frequency eddies at 5 meters, while at high frequencies (f>.4) the eddies appear to be convected along at the speed of the mean wind. During the generating conditions (figure 4.3) the picture has changed. The eddies at all frequencies except those at the dominant wave frequencies tend to move slower than the mean wind.

This result suggests that the validity of Taylor's hypothesis is suspect in the near-ocean atmosphere that spectral domain encompassing frequencies at which ocean surface waves can be expected to occur. For all frequencies in figure 4.2 and for the swell frequencies in figure 4.3, experimental information is inadequate to draw any inferences about possible phase lock, since there is no reason to expect the swell or the old wind-sea to be propagating in the same direction as the mean wind. The wind-sea in figure 4.3, however, was generated by the observed mean wind. In this case, we should expect the wind-waves to propagate in the same mean direction as the mean wind. Figure 4.3 suggests the existence of phase lock for wind waves at both 1 and 5 meters. At frequencies greater than 0.4 Hz, there appears to be a tendency toward decoupling where some eddies move at a mean wind speed while some remain coupled with the wind waves.

As discussed in chapter I, original plans called for the use of two remote buoys and a three-point space correlation field. The loss of one

of these buoys severely restricted a more definitive study of this problem.

Direct Reynolds Stress Measurements

Application of the techniques discussed in chapter II resulted in the direct measurement of Reynolds stress for 5 cases. Unfortunately, a large amount of data was discarded since the data transmission resolution problem discussed in chapter II was not fully appreciated until late in the summer. Those runs of sufficient quality to process are listed in table 4.2.

The tabulated drag coefficients agree with those of Weiler and Burling (1967), while the value of $\overline{u'w'}$ agrees with the square of the friction velocity, U_*^2, derived from the profiles. In case 5, the measured value of $\overline{u'w'}$ appears high; however it is measured at a wind velocity very close to that at which the boundary instability appears to occur as discussed in chapter II. Values of U_*^2 may deviate from the observed $\overline{u'w'}$ in this regime due to the use of ten minute average mean wind speeds. Perhaps shorter averaging times are appropriate. In all cases the normalized standard error of estimate is .10 (see appendix II).

Wind-Wave Coupling and Capillary Waves

During the course of the experiments, wind parameters were measured over a sea covered with an artificial sea slick. The measurements are compared with measurements made without a sea slick. These experiments provide detailed information about the near-surface wind field and provide an indication of the importance of small waves to air-sea interaction processes.

TABLE 4.2

Direct Reynolds Stress Measurements

Case	Eddy Correlation $\overline{u'w'}$ cm^2/sec^{-2}	Mean wind U(10) $meters/sec^{-1}$	Profile $U*^2$ cm^2/sec^{-2}	Drag Coefficient $C_D \times 10^{-3}$
1	840	7.2	810	1.7
2	400	4.5	380	2.0
3	625	7.0	770	1.3
4	1290	9.3	1225	1.4
5	1510	8.2	930	2.3

The sea slick was developed by Barger and Garret (1968) to provide intense capillary wave damping. Dr. Barger and Dr. Garret also developed the technique for dispensing the slick material, and worked directly with this investigator by providing the material and supervising its dispersion over the sea surface. The experimental technique for applying the slick and its gross results on both the wind field and the wind sea is described by Barger, et al. (1969). Briefly, measurements were made before, during and after an artificial sea slick had been spread over the ocean surface. Marked modification of the wind profile roughness length parameter and the high frequency wave energy was noted.

Using the techniques discussed in chapter II, the wind at a height of 1 meter above the mean water surface was resolved into a horizontal component, U, and a vertical component, W. Each of these components, taken individually and together, were used to compute cross spectral density functions relating the variables to wave height as measured by a wave gauge. From these computations, the coherence between the spectral component of the wave field and the corresponding spectral component of the wind is computed. The coherence is defined:

$$C(f) = \frac{S_{12}(f)^2}{S_{11}(f)\ S_{22}(f)} \qquad (4.10)$$

where the spectral density function S_{ii} is defined in equation (4.7), and the subscripts 1 and 2 relate to any specified variables 1 and 2 respectively.

Figure 4.4 displays the wave spectrum measured (a) well before the

slick arrived at the site, (b) just after the slick enveloped the site, and (c) just after the slick cleared the site. Note in particular the reduction of wave energy at high frequencies (greater than 0.3 Hz) as the slick persists. The increased wind-wave energy between the 1140 A.M. spectrum and the 1240 spectrum clearly identifies the condition as one in which wind waves were being generated. That portion of the spectrum above 0.3 Hz is the saturated portion of the wave spectrum, and should be constant from spectrum to spectrum.

Figure 4.4 is constructed from a digitally computed spectrum. In order to eliminate uncertainty in the high frequency spectral estimates introduced by Nyquist folding, a spectrum was computed by analog techniques only for the high frequency components of the waves, using wave height data passed through a high pass filter and a waveform analyzer. Figure 4.5(a) represents the wave spectrum measured at the same time the 1140-1210 spectrum in figure 4.4 was measured. Figure 4.5(b) was measured just before the slick cleared the measurement site, while figure 4.5(c) shows the wave energy well after the slick had cleared the measurement site. The difference in high frequency wave energy from spectrum to spectrum is clearly evident.

We will compare the wind field over the ocean during the time the sea slick was in the vicinity of the measurement site with the wind field observed after the slick had passed. This choice is based on the similarity of the ocean surface wave spectrum for each period as shown in figure 4.4. The wave spectrum measured before the slick arrived at the site differs enough from the other two spectra to eliminate this run for

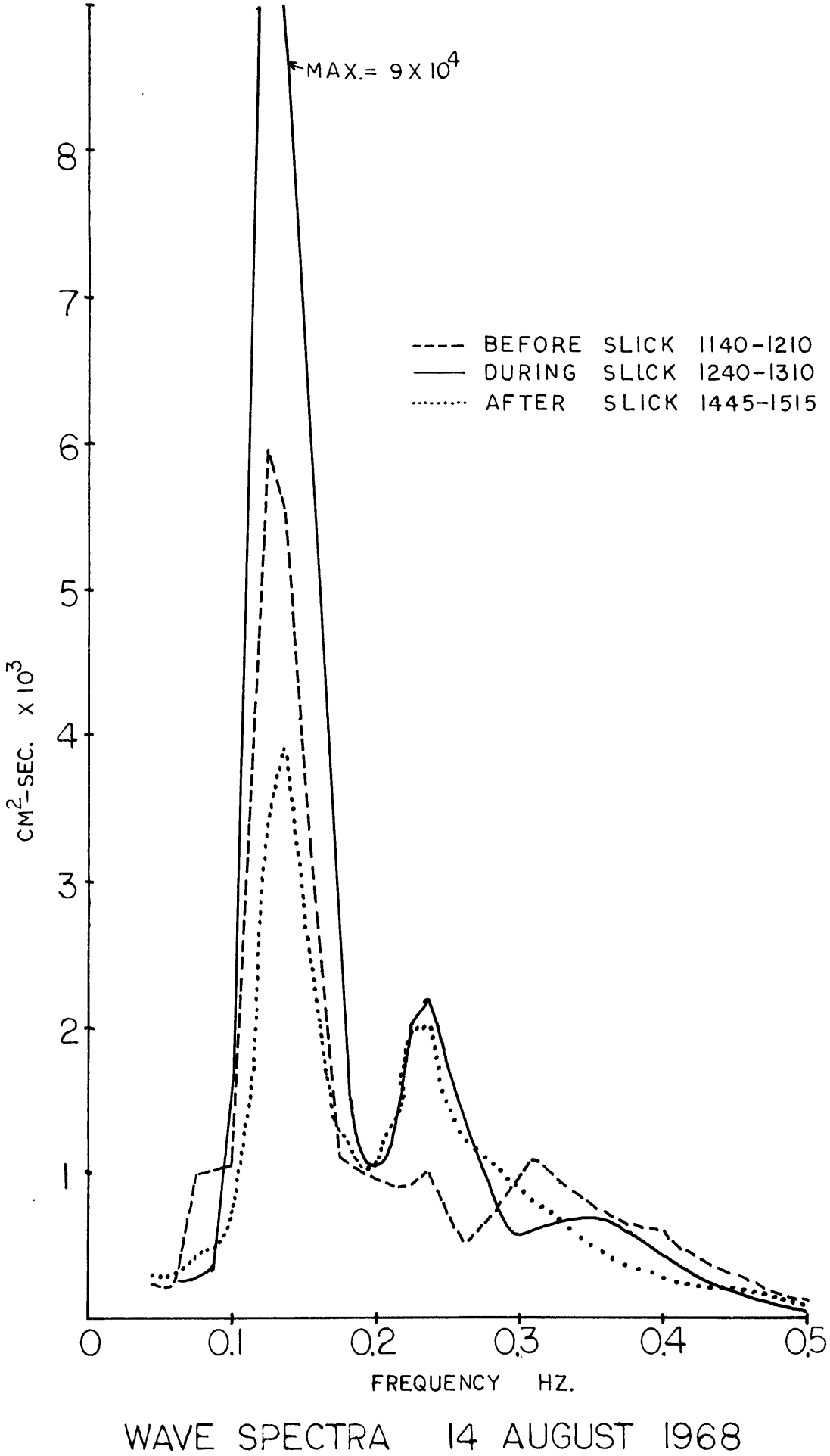

Figure 4.4 Digital wave spectrum.

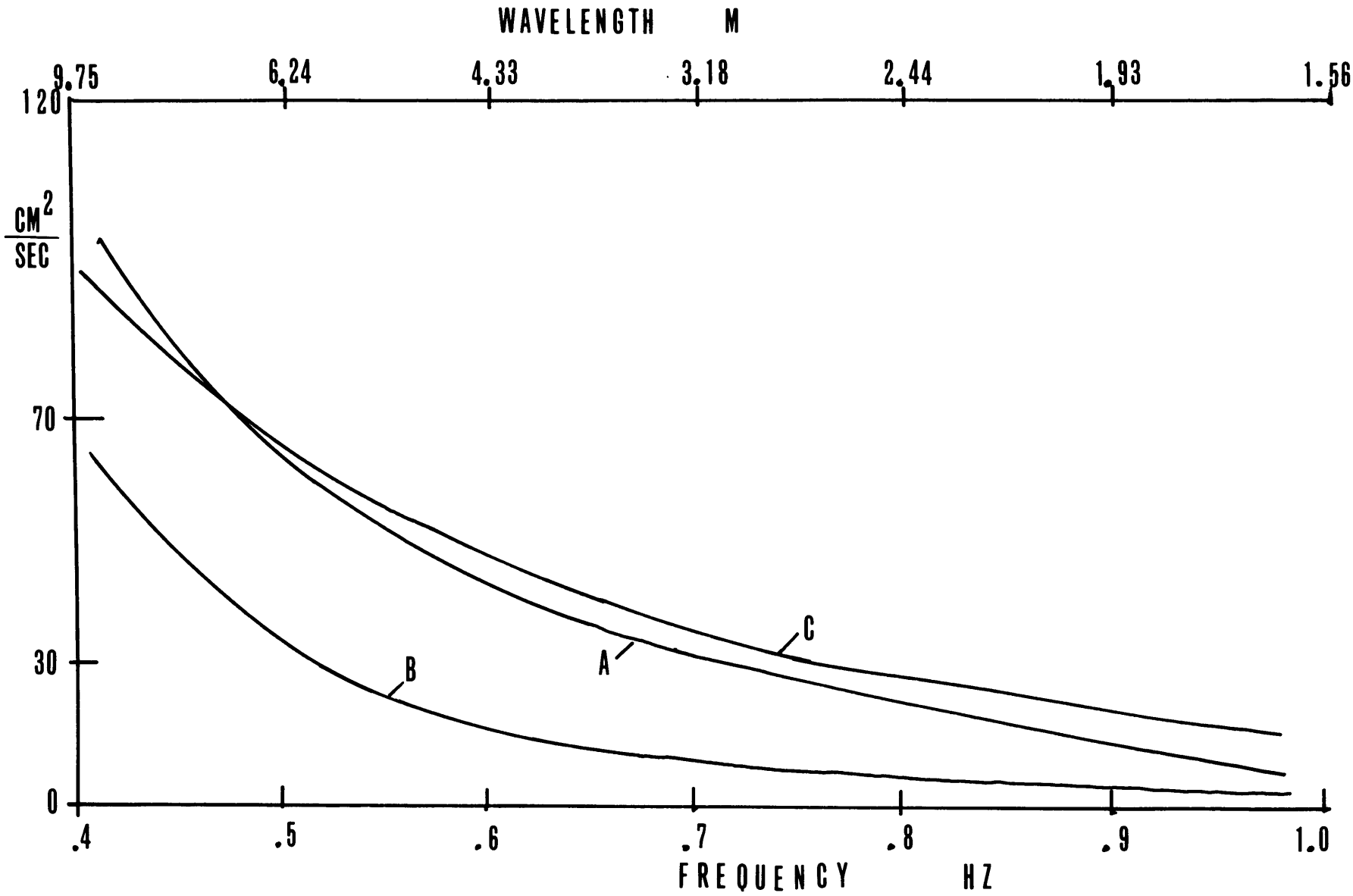

Figure 4.5 Analog wave spectrum above 0.4Hz.

direct comparison of the data.

The cross spectral density and coherence was computed for the following variables measured during and after the passage of the artificial sea slick:

a. Horizontal velocity, U, versus wave height, η.

b. Vertical velcoity, W, versus wave height, η.

c. Horizontal velocity, U, versus vertical velocity, W. (Reynolds stress).

Plots of this data are displayed in figures 4.6 through 4.8. For all plots, the spectral bandwidth is .025 Hz, and the standard error of estimate is 0.10 with 100 degrees of freedom. These plots indicate:

a. The coherence between the swell and the wind field is modified only slightly, if at all, by the presence of a sea slick. Without the slick, however, the horizontal velocity maximum occurs over the wave trough. With the slick present, the horizontal velocity maximum shifts to over the wave crest.

b. The coherence between the wind sea and the wind field directly above the water surface is strongly influenced by the presence of the slick. With the slick absent, there is a moderate coupling of the wind and the sea. When the slick is present, the wind field appears to lose all knowledge of the motions of the wind-sea. This can be seen in the U and W versus η coherence plots and also in the U versus W phase angles. The phase angles of this Reynolds stress spectrum are completely unaffected by the underlying sea during the presence of a slick.

c. The horizontal velocity (figure 4.6) is a maximum over the wave trough for both the wind sea and the swell. This result was first observed by Seesholtz (1968). At that time some had argued that such might be true for either the wind sea or the swell; however, figure 4.3 shows this phase relation to be true for both.

On the basis that the primary effect of a sea slick is the damping of capillary waves, the experimental evidence suggests that the coupling of the long wavelength wind-waves to the atmosphere is controlled in some manner by the capillary or short wavelength gravity waves. This would suggest that theoretical models for wave generation need to address both the long wavelengths generating wave and its relation with the short wavelengths wave. Similarly, it would appear that laboratory investigations may be of limited value in wind-wave generation studies unless both the long wavelength gravity wave and the short wavelength capillary wave can be simultaneously scaled and represented in a laboratory environment.

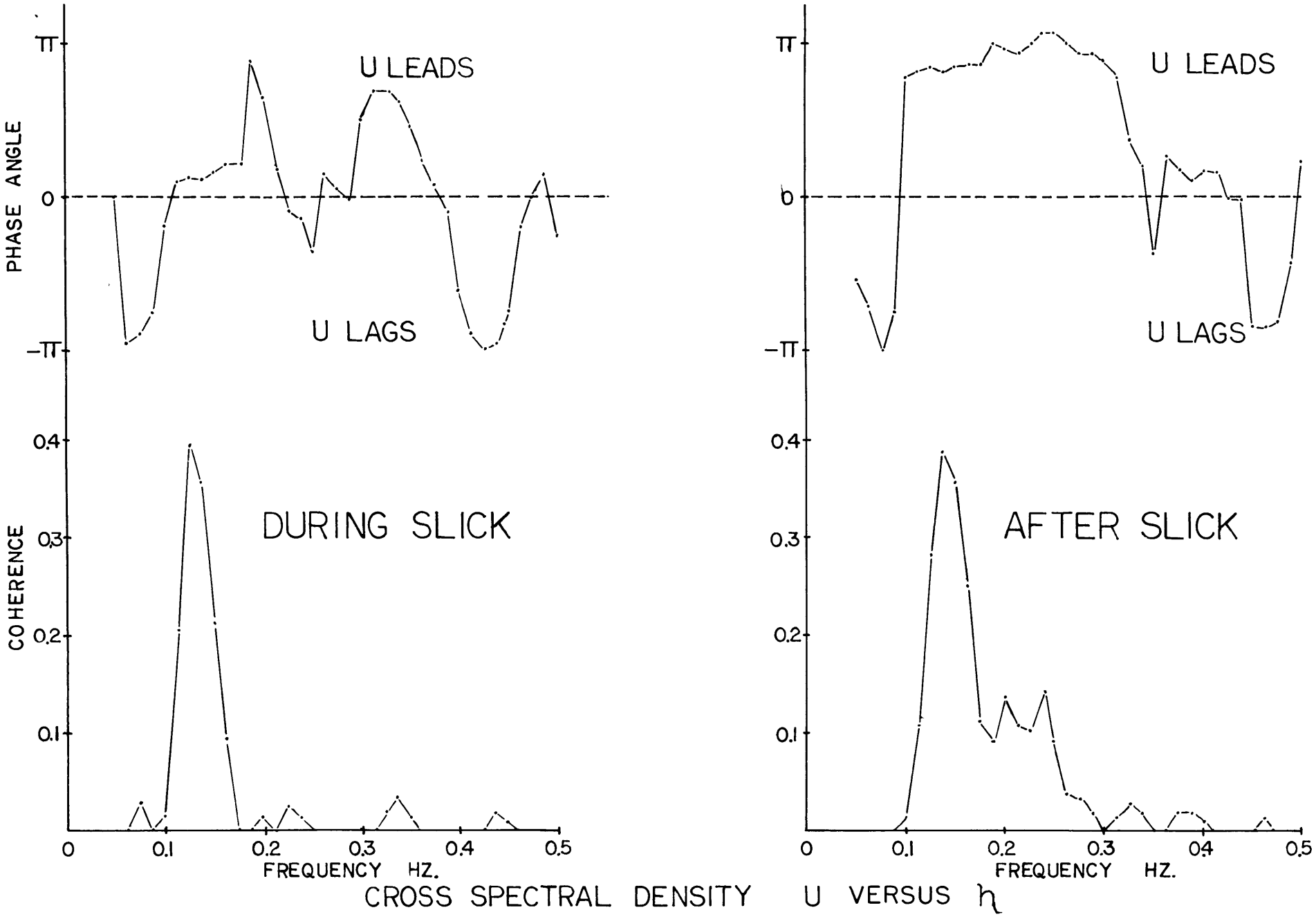
PHASE ANGLE
π
0
-π
U LEADS
U LAGS
COHERENCE
0.4
0.3
0.2
0.1
DURING SLICK
AFTER SLICK
0
0.1
0.2
0.3
0.4
0.5
FREQUENCY HZ.
CROSS SPECTRAL DENSITY U VERSUS η

Figure 4.6

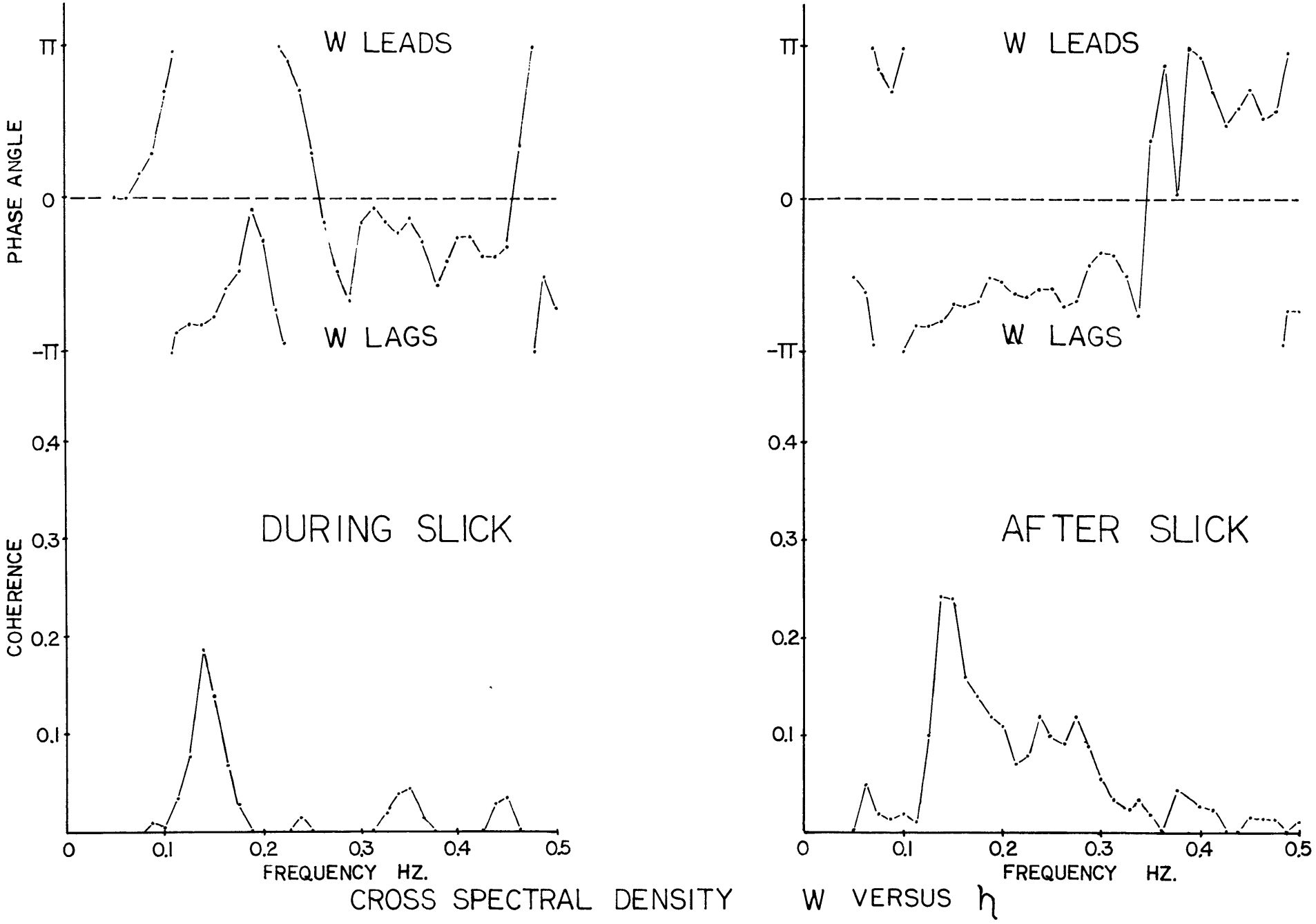
W LEADS
W LAGS
PHASE ANGLE
π
0
-π
0.4
0.3
0.2
0.1
COHERENCE
DURING SLICK
AFTER SLICK
0
0.1
0.2
0.3
0.4
0.5
FREQUENCY HZ.
CROSS SPECTRAL DENSITY W VERSUS h

Figure 4.7

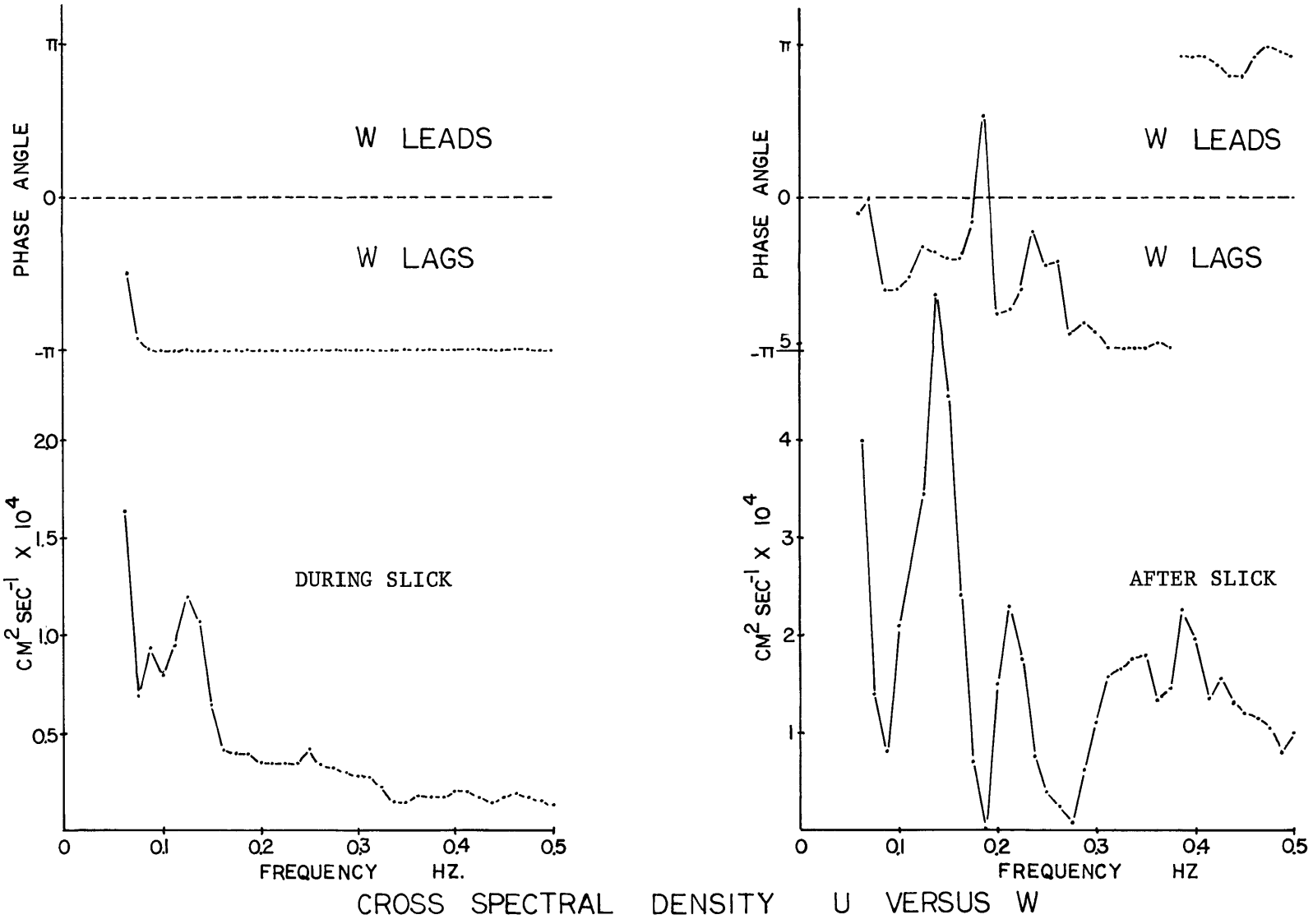

CROSS SPECTRAL DENSITY U VERSUS W

Figure 4.8

Chapter V

Summary of Results and Recommendations

The Direct Measurement of Reynolds Stress

The techniques outlined in this report appear to provide valid results for the direct measurement of Reynolds stress. Unfortunately, a large portion of the summer effort was expended perfecting the technique, so the results were not as copious as desired. The data presented in chapter IV represents measurements made under near ideal equipment conditions. That is, all instrument gains were set at near optimum levels for data transmission, while system noise was low. The measurement system appears to be capable of surviving in the environment, if one can insure faithful data recording and conversion.

Availability of digital processing or sophisticated analog data processing is mandatory for processing the data from the Reynolds stress sensor. The individual probe signals should be recorded either analog or digitally without linearizaton and then linearized by the terminal processor. If digital processing is used, a minimum of 12 bits of significance is considered necessary to avoid loss of data significance due to quantitizing errors. Significance was achieved with a 10-bit digitizer only through careful data selection and gain adjustment.

It is recommended that continued direct measurements of Reynolds stress be made, but only after facilities are available to provide digital data with 12 bits or more of significance for processing. The preferred alternative is digital recording in the field. This step by passes intermediate analog recording and processing, eliminating the attendant opportunity for data degradation.

The DISA anemometer systems used for measuring Reynolds stress proved to be ideally suited to the task. The weak point in the system is the step resistance changes of the probes. This probe behavior is unsatisfactory and needs correction. It would appear that the probe behavior is more a result of manufacturing quality control than design. A probe purchased in 1967 performed for two years without trouble, while all of the probes purchased in 1968 suffered unacceptable resistance variability.

Vertical Mean Wind Profiles

Details of the vertical mean wind profile parameters are beginning to emerge. In the wind regime studied, the wind speed and the friction velocity are linearly related in the mean, while the roughness length parameter is highly structured. Evidence suggests a minimum 10 meter wind speed for wave generation of 2 meters/sec^{-1}. The roughness length and friction velocity plots indicate the existence of boundary instability at a ten meter wind speed of 4 and 8 meter/sec^{-1}. The instability at 8 meters/sec^{-1} can be explained by the Kelvin-Helmholtz instability. The one at 4 meters/sec^{-1} needs explanation. Finally, the mean profiles were shown to have a component which contributes to boundary modification.

It is important to consider the profile results in terms of an air-sea momentum budget. That momentum lost by the atmosphere can be partitioned into a portion lost to friction, a portion lost to the maintenance of the existing wave field, and a portion required to generate new waves. Other effects, such as drift current generation, can be lumped together with the friction term. Use of the profile parameter plots as models of the

atmosphere in some wave-generation prediction scheme may be ill-advised since the plots do not provide for the partition of momentum between that required to maintain the wind sea and that provided for further growth of wind waves. Failure to consider the momentum partition may have further intorduced a systematic bias into the plots. At intermediate wind speeds one might expect generating conditions to be observed more frequently while at high wind speeds the momentum required for maintaining the existing wave field may become the dominant effect. Therefore the plots in chapter III are presented as representing a "typical" mean state of the vertical mean wind profile over the sea.

Clearly, the next step in the study of the vertical mean wind profile over the sea is the consideration of momentum partition. It is recommended that observed profiles be catalogued and sub-divided into three sets; one set containing profiles observed during rising seas, one set containing profiles observed during falling seas, and finally one set of profiles observed during fully arisen seas. Each set can be analyzed using the techniques followed in chapter III. The resulting profile parameters will represent mean profiles appropriate for use in modeling an air-sea relationship.

In order to provide for the fine grained analysis of mean wind profiles over the ocean, the profile data set must be increased by at least a threefold amount. It is recommended that efforts continue to collect mean wind profiles over the ocean from rigid platforms.

Small scale wind motions above the sea.

The Taylor Hypothesis does not appear to be a valid approximation for treating turbulence directly above the ocean surface in the spectral

domain of ocean surface waves.

Sea slicks whose effects on ocean surface waves is the intense damping of capillary wave systems are shown to have strong effects on the coupling of the near-ocean wind field with the long wave length ocean wind waves. This result suggests that the capillary waves play an important role in the generation of wind waves and the dynamics of the atmospheric boundary layer above the ocean surface.

The horizontal velocity maximum occurs over the wave trough, both for the swell and the components of the wind sea.

These results demonstrate the importance of observing small scale atmospheric processes near the ocean surface. The use of artificial sea slicks provides the field investigator with a powerful research tool. Their use constitutes one of the few measures a field researcher can employ to control his environment. It is strongly recommended that this technique be exploited to its fullest to enhance our understanding of the small scale processes at the air-sea boundary.

The apparent importance of capillary waves and/or short gravity waves to air-sea dynamics is a matter requiring additional investigation, both theoretical and experimental. Before realistic models of the air-sea boundary processes can be constructed, the role of these waves in the total dynamics must be identified.

Acknowledgements

Professor Erik L. Mollo-Christensen at the Massachusetts Institute of Technology has been my principal source of advice, support and instruction during the past several years. His encouragement and patience is most sincerely appreciated.

Mr. Ortwin von Zweck worked closely with me both in the field and during the analysis phase of the project. Our many long discussions and hours working together on common problems has been a key to the success of this study.

Mr. Kenneth A. Morey and Mr. James H. Peers worked on the technical end of this study since its inception. Their innovative skill, technical competence, and willingness to devote many long hours to the support of this work contributed to the success of the project.

There are many who have contributed each in his special way to this effort. Mr. Anthony Cella worked many hours with me on Lewis Wharf assembling the prototype satellite buoy system during the early stages of this project. Mr. Edward Bean's skill in the machine shop overcame many of the design problems in the satellite buoy. Mr. Louis LeTourneau operated the research boat during the field portion of the work. Miss Louise Harris and Miss Diane Lippincott typed the manuscript.

Appendix I

Wind Profile Data

Elementary statistical techniques have been applied to the raw wind profile data to develop this table of data. The usual form for the logarithmic wind profile can be written:

$$\ell n(z) = \frac{K}{U_*} U(z) + \ell n(z_o) \qquad \text{(AI.1)}$$

where z is the height above the boundary, $\overline{U}(z)$ is the mean wind at height z, U_* is the "friction velocity", where $U_*^2 = -\overline{U'W'}$; K is von Karman's constant and is equal to approximately 0.42 and z_o is the roughness length. Equation (AI.1) is linear in $\ell n(z)$, therefore the logarithmic wind profile can be fitted to the raw data using linear regression techniques (see chapter 3). Such a best fit establishes the form of the profile, the roughness length, z_o, and the friction velocity, U_*. Further, a correlation coefficient can be computed providing a measure of how accurately the logarithmic profile represents the raw wind data.

After the form of the profile had been established, the wind data was printed for the "standard" heights as shown in the table. When raw wind data was available for the standard height, it was printed, otherwise a wind velocity computed from equation (A1.1) was printed. The standard observation heights for all data during the summer of 1968 was 1 meter, 2 meters, 3 meters, 5 meters, and 8.2 meters. The observation heights for Seesholtz' data are as published by Seesholtz (1968).

The drag coefficient is defined as:

$$C_D = \left(\frac{U_*}{U}\right)^2 \qquad \text{(AI.2)}$$

This was computed using the value of friction velocity derived from the profile for 2 meters and 10 meters.

The gradient Richardson number is defined as:

$$Ri = \frac{g}{\theta} \frac{\frac{\partial \theta}{\partial z}}{(\frac{\partial v}{\partial z})^2} \qquad \text{(AI.3)}$$

For purposes of computation, equation (AI.3) was rewritten:

$$Ri = (\frac{g}{\bar{T}}) \ (\frac{\Delta T}{\Delta z} - \Gamma_d) \ (1/(\frac{\Delta U}{\Delta z})^2) \qquad \text{(AI.4)}$$

Where $\bar{T}$ was the mean temperature at 3 meters, $\Delta T/\Delta z$ the temperature gradient between 1 and 5 meters, Γ_d the dry adiabatic lapse rate, and $\Delta U/\Delta z$ the wind gradient between 1 and 5 meters. g is the acceleration due to gravity.

Each profile is identified by the month, day and run number. For example, profile 08-14-203 is the third profile taken during run 2 on 14 Augst 1968. The profiles carrying an "S" in front of the profile identity were compiled from Seesholtz' data.

Further details on the measurement and computation of the pertinent profile information is contained in the appropriate sections of this report.

WIND PROFILE DATA

PROFILE NUMBER	WIND SPEED VS. HEIGHT 1M.	2M.	5M.	10M.	PROFILE FIT	RICHARDSON NUMBER
7-23-101	508.	552.	610.	654.	1.00	
7-23-102	563.	615.	682.	733.	1.00	
7-23-104	537.	590.	635.	682.	0.70	
7-23-105	543.	595.	659.	708.	1.00	
7-23-106	546.	598.	665.	716.	1.00	
7-23-107	537.	587.	647.	694.	1.00	
7-23-108	511.	560.	621.	668.	1.00	
7-23-109	492.	538.	600.	646.	1.00	
7-23-110	513.	556.	612.	654.	1.00	
7-23-201	486.	534.	595.	641.	1.00	
7-23-202	481.	527.	586.	632.	1.00	
7-23-203	418.	462.	520.	564.	1.00	
7-23-204	416.	461.	514.	556.	1.00	
7-23-205	410.	457.	515.	561.	1.00	
7-23-206	401.	445.	548.	616.	0.97	
7-24-101	190.	199.	214.	225.	0.99	
7-24-102	119.	124.	134.	140.	0.99	
7-24-103	127.	129.	136.	140.	0.91	
7-24-104	178.	179.	188.	193.	0.85	
7-26-101	204.	223.	258.	282.	0.99	
7-26-102	156.	164.	181.	193.	0.98	
7-26-103	142.	160.	191.	212.	0.99	
7-26-104	133.	153.	181.	201.	1.00	
7-29-101	440.	507.	600.	669.	1.00	
7-29-102	444.	522.	676.	780.	0.98	
7-29-103	430.	497.	624.	711.	0.99	
7-29-104	517.	571.	680.	753.	0.98	
7-29-201	524.	569.	631.	678.	1.00	
7-29-202	545.	583.	636.	675.	1.00	
7-29-203	519.	552.	600.	635.	1.00	
8-02-101	343.	374.	413.	446.	1.00	0.02481
8-02-102	343.	377.	423.	462.	1.00	0.01878
8-02-103	278.	304.	346.	376.	1.00	0.02587
8-02-104	279.	317.	369.	408.	1.00	0.01003
8-02-105	337.	379.	431.	475.	1.00	0.02100
8-02-106	368.	409.	463.	506.	1.00	0.02079
8-03-101	452.	488.	555.	601.	0.99	0.00497
8-03-102	477.	517.	590.	640.	0.99	0.00418
8-03-103	440.	480.	547.	594.	0.99	0.00460
8-03-104	366.	401.	463.	506.	0.99	0.00560

VELOCITIES IN CM./SEC. HEIGHTS IN METERS

DERIVED PROFILE DATA

PROFILE NUMBER	ROUGHNESS LENGTH	FRICTION VELOCITY 1M.	2M.	5M.	10M.	DRAG COEF. 2M.	10M.
7-23-101	0.03307	25.3	25.4	25.3	25.3	0.0021	0.0015
7-23-102	0.04701	29.4	29.4	29.4	29.4	0.0023	0.0016
7-23-104	0.04836	28.1	28.3	27.5	27.5	0.0023	0.0016
7-23-105	0.05045	28.6	28.7	28.6	28.6	0.0023	0.0016
7-23-106	0.06069	29.5	29.5	29.5	29.5	0.0024	0.0017
7-23-107	0.03686	27.2	27.3	27.2	27.2	0.0022	0.0015
7-23-108	0.05240	27.1	27.1	27.1	27.1	0.0024	0.0016
7-23-109	0.06468	26.8	26.8	26.8	26.8	0.0025	0.0017
7-23-110	0.02309	24.5	24.5	24.5	24.5	0.0019	0.0014
7-23-201	0.07193	26.9	26.9	26.9	26.9	0.0025	0.0018
7-23-202	0.06528	26.2	26.2	26.2	26.2	0.0025	0.0017
7-23-203	0.13922	25.4	25.4	25.4	25.4	0.0030	0.0020
7-23-204	0.09831	24.0	24.2	24.1	24.1	0.0028	0.0019
7-23-205	0.18706	26.1	26.2	26.1	26.1	0.0033	0.0022
7-23-206	1.74909	39.6	37.6	38.8	38.8	0.0071	0.0040
7-24-101	0.00045	6.2	6.1	6.2	6.2	0.0009	0.0007
7-24-102	0.00027	3.7	3.7	3.7	3.7	0.0009	0.0007
7-24-103	0.00000	2.4	2.4	2.4	2.4	0.0003	0.0003
7-24-104	0.00000	2.8	2.8	2.8	2.8	0.0002	0.0002
7-26-101	0.27650	13.9	13.5	13.8	13.8	0.0037	0.0024
7-26-102	0.00893	6.7	6.6	6.6	6.6	0.0016	0.0012
7-26-103	1.02859	12.4	12.1	12.3	12.3	0.0058	0.0034
7-26-104	1.12484	11.9	11.8	11.8	11.8	0.0060	0.0035
7-29-101	1.23676	40.0	39.9	40.0	40.0	0.0062	0.0036
7-29-102	5.50893	61.2	58.2	60.0	60.0	0.0124	0.0059
7-29-103	3.34642	50.7	48.6	49.9	49.9	0.0096	0.0049
7-29-104	0.78237	42.6	41.2	42.1	42.1	0.0052	0.0031
7-29-201	0.03925	26.7	26.7	26.7	26.7	0.0022	0.0016
7-29-202	0.00668	22.7	22.6	22.7	22.7	0.0015	0.0011
7-29-203	0.00344	20.2	20.1	20.2	20.2	0.0013	0.0010
8-02-101	0.04338	17.7	17.7	17.7	17.8	0.0022	0.0016
8-02-102	0.12760	20.6	20.5	20.5	20.6	0.0030	0.0020
8-02-103	0.16288	17.3	17.1	17.3	17.3	0.0032	0.0021
8-02-104	0.66906	22.3	22.3	22.3	22.3	0.0049	0.0030
8-02-105	0.35393	23.9	23.9	23.8	23.9	0.0040	0.0025
8-02-106	0.21439	24.0	23.9	23.9	24.0	0.0034	0.0022
8-03-101	0.11242	26.6	26.1	26.4	26.4	0.0029	0.0019
8-03-102	0.13867	29.0	28.4	28.8	28.8	0.0030	0.0020
8-03-103	0.15988	27.3	26.9	27.2	27.2	0.0031	0.0021
8-03-104	0.28322	25.0	24.5	24.8	24.8	0.0037	0.0024

VELOCITIES IN CM./SEC. HEIGHTS IN METER EXCEPT ROUGHNESS LENGTH IS IN CENTIMETERS.

WIND PROFILE DATA

PROFILE NUMBER	WIND SPEED VS. HEIGHT 1M.	2M.	5M.	10M.	PROFILE FIT	RICHARDSON NUMBER
8-03-105	314.	350.	415.	460.	0.99	0.00514
8-03-106	296.	298.	348.	376.	0.80	0.02006
8-05-102	601.	687.	800.	886.	1.00	0.00133
8-05-103	644.	688.	747.	792.	1.00	0.00997
8-05-104	561.	626.	713.	778.	1.00	0.00231
8-05-105	495.	518.	549.	573.	1.00	0.04064
8-05-106	492.	594.	730.	833.	1.00	0.00117
8-05-201	469.	576.	717.	824.	1.00	0.00306
8-05-202	475.	583.	725.	833.	1.00	0.00301
8-05-203	477.	590.	740.	853.	1.00	0.00272
8-05-204	474.	589.	742.	858.	1.00	0.00261
8-05-205	447.	572.	738.	863.	1.00	0.00383
8-06-101	552.	592.	656.	705.	0.99	0.00494
8-06-102	576.	620.	680.	731.	0.99	0.00496
8-06-103	574.	613.	677.	727.	0.99	0.00491
8-06-104	600.	643.	709.	763.	0.99	0.01600
8-06-105	560.	600.	659.	710.	0.99	0.00551
8-06-106	583.	624.	690.	740.	0.99	0.01651
8-06-107	583.	624.	682.	727.	1.00	0.01248
8-06-108	529.	560.	614.	647.	0.99	0.04453
8-06-109	478.	513.	565.	599.	1.00	0.03923
8-06-201	536.	575.	631.	681.	0.99	-0.00908
8-06-202	544.	582.	640.	687.	0.99	-0.00885
8-06-203	521.	558.	613.	657.	1.00	-0.00961
8-06-204	510.	547.	607.	648.	1.00	-0.00877
8-06-205	504.	541.	599.	641.	1.00	-0.00908
8-06-206	491.	527.	582.	627.	0.99	-0.00175
8-06-207	408.	438.	479.	515.	0.99	-0.00294
8-06-208	432.	465.	516.	558.	0.99	-0.00208
8-06-209	448.	484.	540.	585.	0.99	0.00623
8-06-210	474.	519.	578.	629.	0.99	0.00487
8-07-101	266.	292.	354.	392.	0.99	
8-07-102	287.	311.	364.	398.	0.99	
8-07-103	273.	294.	333.	361.	0.99	
8-07-104	268.	289.	334.	363.	0.99	
8-07-105	247.	270.	313.	341.	1.00	
8-07-106	255.	284.	340.	377.	0.99	
8-07-107	259.	285.	335.	369.	0.99	
8-07-108	255.	271.	317.	344.	0.98	
8-09-101	317.	284.	385.	472.	0.73	

VELOCITIES IN CM./SEC. HEIGHTS IN METERS

DERIVED PROFILE DATA

PROFILE NUMBER	ROUGHNESS LENGTH	FRICTION VELOCITY 1M.	2M.	5M.	10M.	DRAG COEF. 2M.	10M.
8-03-105	0.83403	26.2	25.5	26.0	26.0	0.0053	0.0032
8-03-106	0.08396	16.7	15.3	16.0	16.0	0.0026	0.0018
8-05-102	0.79030	49.6	49.6	49.6	49.6	0.0052	0.0031
8-05-103	0.00456	25.8	25.8	25.8	25.8	0.0014	0.0011
8-05-104	0.25863	37.7	37.7	37.7	37.7	0.0036	0.0023
8-05-105	0.00004	13.5	13.5	13.5	13.5	0.0007	0.0006
8-05-106	3.61881	59.3	59.3	59.3	59.3	0.0099	0.0051
8-05-201	4.74580	61.6	61.6	61.6	61.6	0.0114	0.0056
8-05-202	4.70204	62.2	62.2	62.2	62.2	0.0114	0.0056
8-05-203	5.39393	65.3	65.3	65.3	65.3	0.0123	0.0059
8-05-204	5.84018	66.7	66.7	66.7	66.7	0.0128	0.0060
8-05-205	8.41221	72.3	72.3	72.3	72.3	0.0159	0.0070
8-06-101	0.02694	26.9	26.6	26.7	26.8	0.0020	0.0014
8-06-102	0.01956	27.0	26.9	26.8	27.0	0.0019	0.0014
8-06-103	0.02075	27.1	26.7	26.9	27.0	0.0019	0.0014
8-06-104	0.02230	28.6	28.3	28.3	28.5	0.0019	0.0014
8-06-105	0.01890	26.1	25.9	25.9	26.1	0.0019	0.0014
8-06-106	0.02149	27.6	27.3	27.4	27.5	0.0019	0.0014
8-06-107	0.00901	25.1	24.9	25.0	25.0	0.0016	0.0012
8-06-108	0.00472	21.2	21.0	21.2	21.1	0.0014	0.0011
8-06-109	0.01355	21.5	21.4	21.5	21.4	0.0017	0.0013
8-06-201	0.02166	25.4	25.2	25.1	25.4	0.0019	0.0014
8-06-202	0.01760	25.1	24.9	25.0	25.1	0.0018	0.0013
8-06-203	0.01583	23.8	23.6	23.7	23.8	0.0018	0.0013
8-06-204	0.02281	24.3	24.1	24.3	24.2	0.0019	0.0014
8-06-205	0.02321	24.1	23.9	24.0	24.0	0.0019	0.0014
8-06-206	0.02642	23.8	23.6	23.6	23.8	0.0020	0.0014
8-06-207	0.01463	18.5	18.4	18.4	18.5	0.0018	0.0013
8-06-208	0.04048	22.1	21.9	21.9	22.1	0.0022	0.0016
8-06-209	0.05922	24.1	23.8	23.9	24.0	0.0024	0.0017
8-06-210	0.08794	26.9	26.9	26.7	26.9	0.0027	0.0018
8-07-101	1.04206	23.3	22.2	22.9	22.8	0.0058	0.0034
8-07-102	0.35400	20.3	19.6	20.1	20.0	0.0040	0.0025
8-07-103	0.09021	15.6	15.3	15.4	15.5	0.0027	0.0018
8-07-104	0.20298	17.3	16.8	17.1	17.1	0.0034	0.0022
8-07-105	0.29314	16.9	16.5	16.8	16.8	0.0038	0.0024
8-07-106	0.98653	22.1	21.4	21.8	21.8	0.0057	0.0033
8-07-107	0.52543	19.7	19.2	19.6	19.5	0.0045	0.0028
8-07-108	0.21026	16.6	15.8	16.3	16.3	0.0034	0.0022
8-09-101	6.10017	45.4	32.5	35.0	37.1	0.0131	0.0062

VELOCITIES IN CM./SEC. HEIGHTS IN METER EXCEPT ROUGHNESS LENGTH IS IN CENTIMETERS.

WIND PROFILE DATA

PROFILE NUMBER	WIND SPEED VS. HEIGHT 1M.	2M.	5M.	10M.	PROFILE FIT	RICHARDSON NUMBER
8-09-102	338.	370.	408.	442.	1.00	
8-09-103	368.	406.	457.	496.	1.00	
8-09-104	340.	370.	415.	447.	1.00	
8-09-105	355.	389.	433.	468.	1.00	
8-09-106	320.	353.	402.	440.	1.00	
8-09-107	328.	358.	406.	440.	1.00	
8-09-108	378.	411.	456.	491.	1.00	
8-09-109	384.	385.	463.	512.	0.91	
8-09-201	548.	596.	662.	713.	1.00	
8-09-202	539.	584.	646.	693.	1.00	
8-09-203	547.	593.	654.	704.	1.00	
8-09-204	601.	653.	716.	769.	1.00	
8-12-101	497.	531.	578.	613.	1.00	
8-12-102	447.	486.	535.	573.	1.00	
8-12-103	422.	455.	492.	522.	1.00	
8-12-104	472.	511.	558.	594.	1.00	
8-12-105	483.	522.	570.	607.	1.00	
8-12-106	485.	527.	577.	616.	1.00	
8-12-107	509.	552.	605.	645.	1.00	
8-12-108	498.	540.	591.	631.	1.00	
8-12-109	491.	530.	577.	614.	1.00	
8-12-201	564.	614.	678.	727.	1.00	
8-12-202	553.	601.	657.	701.	1.00	
8-12-203	567.	618.	679.	727.	1.00	
8-12-204	599.	644.	701.	744.	1.00	
8-12-205	598.	644.	703.	747.	1.00	
8-12-206	616.	665.	726.	774.	1.00	
8-12-207	573.	619.	679.	725.	1.00	
8-13-101	292.	313.	359.	387.	0.99	
8-13-102	345.	370.	426.	460.	0.99	
8-13-103	313.	338.	397.	430.	0.99	
8-13-104	300.	323.	375.	405.	0.99	
8-13-105	339.	364.	407.	437.	1.00	
8-13-106	409.	436.	481.	513.	1.00	
8-13-107	485.	520.	580.	621.	1.00	
8-13-108	491.	527.	586.	628.	1.00	
8-13-109	467.	500.	560.	599.	1.00	
8-13-201	476.	537.	565.	633.	0.93	
8-13-202	473.	509.	539.	581.	0.97	
8-13-203	456.	484.	514.	550.	0.97	

VELOCITIES IN CM./SEC. HEIGHTS IN METERS

DERIVED PROFILE DATA

PROFILE NUMBER	ROUGHNESS LENGTH	FRICTION VELOCITY 1M.	2M.	5M.	10M.	DRAG COEF. 2M.	10M.
8-09-102	0.05179	17.9	17.9	17.8	17.9	0.0023	0.0016
8-09-103	0.13348	22.2	22.2	22.2	22.3	0.0030	0.0020
8-09-104	0.07275	18.8	18.7	18.8	18.8	0.0026	0.0018
8-09-105	0.06983	19.6	19.5	19.5	19.6	0.0025	0.0017
8-09-106	0.22936	21.0	20.8	20.9	21.0	0.0035	0.0023
8-09-107	0.13593	19.9	19.7	19.8	19.8	0.0030	0.0020
8-09-108	0.04334	19.5	19.5	19.5	19.5	0.0022	0.0016
8-09-109	0.37525	27.5	24.5	25.8	26.0	0.0041	0.0026
8-09-201	0.04867	28.7	28.6	28.7	28.7	0.0023	0.0016
8-09-202	0.03130	26.7	26.7	26.7	26.7	0.0021	0.0015
8-09-203	0.03200	27.2	27.1	27.1	27.2	0.0021	0.0015
8-09-204	0.02500	29.0	29.1	28.9	29.0	0.0020	0.0014
8-12-101	0.00518	20.1	20.1	20.1	20.1	0.0014	0.0011
8-12-102	0.02788	21.8	21.9	21.9	21.9	0.0020	0.0015
8-12-103	0.00572	17.3	17.4	17.3	17.3	0.0015	0.0011
8-12-104	0.01242	21.0	21.1	21.0	21.0	0.0017	0.0013
8-12-105	0.01271	21.5	21.6	21.5	21.5	0.0017	0.0013
8-12-106	0.01804	22.5	22.6	22.6	22.6	0.0018	0.0013
8-12-107	0.01697	23.5	23.6	23.5	23.5	0.0018	0.0013
8-12-108	0.01730	23.0	23.1	23.0	23.0	0.0018	0.0013
8-12-109	0.00945	21.2	21.3	21.2	21.2	0.0016	0.0012
8-12-201	0.03385	28.2	28.3	28.3	28.3	0.0021	0.0015
8-12-202	0.01663	25.4	25.6	25.5	25.5	0.0018	0.0013
8-12-203	0.02705	27.6	27.8	27.6	27.6	0.0020	0.0014
8-12-204	0.00716	25.1	25.2	25.1	25.1	0.0015	0.0011
8-12-205	0.00961	25.9	25.9	25.9	25.9	0.0016	0.0012
8-12-206	0.01233	27.4	27.4	27.4	27.4	0.0017	0.0013
8-12-207	0.01675	26.3	26.4	26.4	26.4	0.0018	0.0013
8-13-101	0.12482	17.5	16.9	17.3	17.2	0.0029	0.0020
8-13-102	0.14232	21.0	20.4	20.9	20.8	0.0030	0.0020
8-13-103	0.31626	21.7	21.0	21.6	21.3	0.0038	0.0025
8-13-104	0.20481	19.4	18.8	19.2	19.1	0.0034	0.0022
8-13-105	0.04111	17.4	17.2	17.3	17.3	0.0022	0.0016
8-13-106	0.01395	18.4	18.2	18.3	18.4	0.0017	0.0013
8-13-107	0.03173	24.1	23.8	24.0	24.0	0.0021	0.0015
8-13-108	0.03008	24.2	23.9	24.1	24.1	0.0021	0.0015
8-13-109	0.03548	23.5	23.2	23.4	23.4	0.0021	0.0015
8-13-201	0.07531	26.5	27.3	25.7	26.7	0.0026	0.0018
8-13-202	0.00343	18.4	18.5	18.1	18.5	0.0013	0.0010
8-13-203	0.00129	16.2	16.2	16.0	16.2	0.0011	0.0009

VELOCITIES IN CM./SEC. HEIGHTS IN METER EXCEPT ROUGHNESS LENGTH IS IN CENTIMETERS.

WIND PROFILE DATA

PROFILE NUMBER	WIND SPEED VS. HEIGHT 1M.	2M.	5M.	10M.	PROFILE FIT	RICHARDSON NUMBER
8-13-204	481.	485.	513.	538.	0.91	
8-13-205	476.	503.	527.	563.	0.95	
8-13-206	475.	504.	537.	573.	0.98	
8-14-101	527.	576.	619.	681.	0.96	
8-14-102	544.	597.	640.	702.	0.97	
8-14-103	537.	593.	638.	713.	0.94	
8-14-104	554.	612.	654.	729.	0.94	
8-14-105	608.	671.	715.	796.	0.94	
8-14-106	598.	664.	709.	793.	0.94	
8-14-107	588.	655.	692.	779.	0.92	
8-14-108	603.	668.	714.	797.	0.94	
8-14-109	573.	633.	665.	745.	0.91	
8-14-201	575.	632.	669.	748.	0.92	
8-14-202	497.	543.	569.	632.	0.91	
8-14-203	504.	552.	572.	633.	0.91	
8-14-204	718.	780.	775.	899.	0.70	
8-14-205	740.	817.	835.	936.	0.87	
8-14-206	772.	847.	863.	967.	0.85	
8-14-207	713.	789.	813.	907.	0.89	
8-14-208	628.	668.	716.	793.	0.91	
8-14-209	627.	696.	729.	811.	0.93	
8-14-301	549.	614.	653.	722.	0.96	
8-14-302	578.	642.	677.	746.	0.95	
8-14-303	640.	709.	751.	825.	0.96	
8-14-304	669.	735.	780.	854.	0.96	
8-14-305	645.	710.	751.	824.	0.95	
8-26-101	389.	430.	472.	518.	0.98	
8-26-102	378.	417.	449.	493.	0.97	
8-26-103	389.	424.	457.	498.	0.97	
8-26-104	389.	426.	464.	508.	0.98	
8-26-201	342.	384.	433.	477.	0.99	
8-26-202	341.	383.	430.	473.	1.00	
8-26-203	354.	392.	439.	483.	0.99	
8-26-301	342.	381.	426.	469.	0.99	
8-26-302	377.	416.	465.	511.	0.99	
8-26-401	362.	408.	456.	506.	0.99	
8-26-402	321.	360.	402.	445.	0.99	
8-27-101	220.	238.	248.	271.	0.93	
8-27-102	206.	227.	245.	269.	0.98	
8-27-103	228.	248.	269.	296.	0.96	

VELOCITIES IN CM./SEC. HEIGHTS IN METERS

DERIVED PROFILE DATA

PROFILE NUMBER	ROUGHNESS LENGTH	FRICTION VELOCITY 1M.	2M.	5M.	10M.	DRAG COEF. 2M.	10M.
8-13-204	0.00000	11.4	11.0	11.1	11.2	0.0005	0.0004
8-13-205	0.00035	15.1	15.2	14.9	15.2	0.0009	0.0007
8-13-206	0.00142	17.0	17.0	16.8	17.0	0.0011	0.0009
8-14-101	0.03499	26.5	26.6	25.9	26.5	0.0021	0.0015
8-14-102	0.03180	27.0	27.3	26.5	27.1	0.0021	0.0015
8-14-103	0.08518	30.4	30.6	29.4	30.4	0.0027	0.0018
8-14-104	0.06498	30.2	30.5	29.2	30.3	0.0025	0.0017
8-14-105	0.05563	32.4	32.8	31.4	32.5	0.0024	0.0017
8-14-106	0.07956	33.5	33.9	32.4	33.6	0.0026	0.0018
8-14-107	0.08099	33.0	33.5	31.7	33.1	0.0026	0.0018
8-14-108	0.07375	33.4	33.8	32.4	33.5	0.0026	0.0018
8-14-109	0.04545	29.8	30.2	28.6	29.8	0.0023	0.0016
8-14-201	0.04801	30.1	30.3	28.9	30.1	0.0023	0.0016
8-14-202	0.02177	23.6	23.8	22.7	23.6	0.0019	0.0014
8-14-203	0.01105	22.1	22.5	21.3	22.2	0.0017	0.0012
8-14-204	0.03292	35.8	35.8	32.2	34.9	0.0021	0.0015
8-14-205	0.01759	34.2	35.0	32.6	34.2	0.0018	0.0013
8-14-206	0.01293	34.5	35.1	32.7	34.4	0.0017	0.0013
8-14-207	0.02040	33.6	34.3	32.2	33.6	0.0019	0.0014
8-14-208	0.02313	30.0	29.5	28.7	29.7	0.0019	0.0014
8-14-209	0.03317	31.3	32.0	30.3	31.4	0.0021	0.0015
8-14-301	0.05192	29.1	29.7	28.5	29.3	0.0023	0.0016
8-14-302	0.02893	28.4	29.0	27.8	28.6	0.0020	0.0015
8-14-303	0.02581	31.0	31.7	30.4	31.2	0.0020	0.0014
8-14-304	0.01964	31.3	31.9	30.8	31.5	0.0019	0.0014
8-14-305	0.01957	30.2	30.8	29.6	30.4	0.0019	0.0014
8-26-101	0.08600	22.0	22.2	21.8	22.1	0.0027	0.0018
8-26-102	0.04294	19.5	19.7	19.2	19.6	0.0022	0.0016
8-26-103	0.02485	18.7	18.9	18.4	18.8	0.0020	0.0014
8-26-104	0.04936	20.4	20.5	20.1	20.5	0.0023	0.0016
8-26-201	0.27027	23.2	23.2	23.0	23.2	0.0037	0.0024
8-26-202	0.23370	22.5	22.7	22.4	22.6	0.0035	0.0023
8-26-203	0.17169	22.2	22.2	22.0	22.3	0.0032	0.0021
8-26-301	0.18232	21.7	21.8	21.5	21.8	0.0033	0.0022
8-26-302	0.15508	23.3	23.2	23.0	23.3	0.0031	0.0021
8-26-401	0.26759	24.5	24.6	24.2	24.6	0.0037	0.0024
8-26-402	0.22579	21.1	21.2	20.9	21.2	0.0035	0.0023
8-27-101	0.00435	8.8	8.9	8.5	8.8	0.0014	0.0010
8-27-102	0.04648	10.7	10.8	10.6	10.8	0.0023	0.0016
8-27-103	0.04794	11.9	11.9	11.6	11.9	0.0023	0.0016

VELOCITIES IN CM./SEC. HEIGHTS IN METER EXCEPT ROUGHNESS LENGTH IS IN CENTIMETERS.

WIND PROFILE DATA

PROFILE NUMBER	WIND SPEED VS. HEIGHT 1M.	2M.	5M.	10M.	PROFILE FIT	RICHARDSON NUMBER
8-27-201	233.	251.	267.	290.	0.95	
8-27-202	277.	301.	320.	347.	0.96	
8-27-203	476.	518.	542.	586.	0.96	
8-27-301	557.	607.	632.	686.	0.94	
8-27-302	534.	581.	602.	652.	0.94	
8-27-303	574.	626.	655.	710.	0.95	
8-27-304	593.	642.	659.	715.	0.91	
8-27-401	597.	652.	688.	750.	0.96	
8-27-402	565.	619.	659.	714.	0.97	
8-27-403	563.	615.	650.	709.	0.95	
9-06-101	471.	531.	571.	638.	0.96	0.01200
9-06-102	436.	486.	513.	572.	0.93	0.02060
9-06-103	444.	496.	529.	587.	0.95	0.01108
9-06-104	421.	471.	507.	564.	0.96	0.00713
9-06-105	376.	421.	453.	505.	0.96	0.00905
9-06-106	394.	442.	474.	528.	0.96	0.00820
9-06-107	403.	456.	491.	547.	0.96	0.00698
9-06-108	413.	464.	497.	554.	0.96	0.00747
9-06-109	427.	478.	507.	566.	0.94	-0.00227
9-06-110	425.	476.	509.	565.	0.96	-0.00205
9-10-101	360.	576.	657.	844.	0.95	
9-10-102	425.	634.	718.	900.	0.95	
9-10-103	349.	635.	708.	967.	0.92	
9-10-104	500.	620.	699.	801.	0.98	
9-10-105	498.	574.	650.	717.	1.00	
9-10-106	501.	580.	655.	724.	1.00	
9-10-107	487.	561.	627.	692.	0.99	
9-10-108	504.	577.	644.	707.	0.99	
9-10-201	364.	417.	482.	529.	1.00	
9-10-202	335.	384.	441.	486.	1.00	
9-10-203	388.	446.	514.	566.	1.00	
9-10-301	392.	451.	524.	578.	1.00	
9-10-302	385.	447.	516.	572.	1.00	
9-10-303	409.	473.	541.	597.	1.00	
9-10-401	400.	464.	534.	598.	1.00	
9-10-402	342.	411.	453.	513.	0.98	
9-10-403	429.	515.	561.	636.	0.97	
9-10-404	509.	604.	656.	739.	0.97	
S8-02-01	484.	508.	554.	588.	0.99	
S8-02-02	478.	500.	547.	582.	0.99	

VELOCITIES IN CM./SEC. HEIGHTS IN METERS

DERIVED PROFILE DATA

PROFILE NUMBER	ROUGHNESS LENGTH	FRICTION VELOCITY 1M.	2M.	5M.	10M.	DRAG COEF. 2M.	10M.
8-27-201	0.00799	9.9	9.9	9.7	9.9	0.0016	0.0012
8-27-202	0.00833	11.8	12.0	11.6	11.9	0.0016	0.0012
8-27-203	0.00312	18.4	18.7	18.1	18.5	0.0013	0.0010
8-27-301	0.00337	21.6	22.1	21.2	21.8	0.0013	0.0010
8-27-302	0.00211	19.8	20.3	19.5	20.0	0.0012	0.0009
8-27-303	0.00438	22.9	23.3	22.5	23.0	0.0014	0.0011
8-27-304	0.00107	20.7	21.1	20.2	20.8	0.0011	0.0008
8-27-401	0.00968	25.8	26.3	25.4	26.0	0.0016	0.0012
8-27-402	0.01239	25.1	25.5	24.8	25.3	0.0017	0.0013
8-27-403	0.01141	24.8	25.2	24.3	24.9	0.0017	0.0012
9-06-101	0.12446	28.2	28.8	27.5	28.4	0.0029	0.0020
9-06-102	0.05122	23.0	23.5	22.3	23.1	0.0023	0.0016
9-06-103	0.06534	24.2	24.7	23.7	24.4	0.0025	0.0017
9-06-104	0.09187	24.1	24.5	23.6	24.3	0.0027	0.0019
9-06-105	0.10018	21.8	22.2	21.3	21.9	0.0028	0.0019
9-06-106	0.09856	22.7	23.2	22.2	22.9	0.0028	0.0019
9-06-107	0.12598	24.2	24.8	23.7	24.4	0.0029	0.0020
9-06-108	0.09735	23.8	24.3	23.3	24.0	0.0027	0.0019
9-06-109	0.06902	23.5	24.0	22.8	23.6	0.0025	0.0017
9-06-110	0.07596	23.7	24.2	23.2	23.8	0.0026	0.0018
9-10-101	15.61819	77.5	90.4	75.8	81.1	0.0246	0.0092
9-10-102	10.85057	76.6	87.0	75.0	79.6	0.0188	0.0078
9-10-103	24.30229	98.7	120.6	93.7	104.0	0.0360	0.0116
9-10-104	1.78543	49.7	52.6	49.7	50.6	0.0072	0.0040
9-10-105	0.48045	37.3	38.1	37.4	37.5	0.0044	0.0027
9-10-106	0.49770	37.8	38.7	37.9	38.1	0.0045	0.0028
9-10-107	0.36343	34.7	35.6	34.7	35.0	0.0040	0.0026
9-10-108	0.28569	34.4	35.2	34.5	34.6	0.0037	0.0024
9-10-201	0.62402	28.7	28.9	28.8	28.7	0.0048	0.0029
9-10-202	0.57557	26.0	26.3	26.1	26.1	0.0047	0.0029
9-10-203	0.65309	30.9	31.2	31.0	30.9	0.0049	0.0030
9-10-301	0.77379	32.3	32.5	32.4	32.3	0.0052	0.0031
9-10-302	0.81895	32.1	32.6	32.2	32.2	0.0053	0.0032
9-10-303	0.64462	32.4	33.0	32.5	32.5	0.0049	0.0030
9-10-401	0.86295	33.6	34.1	33.6	33.9	0.0054	0.0032
9-10-402	0.80535	28.3	29.8	28.2	28.8	0.0053	0.0032
9-10-403	0.65356	34.1	36.0	33.8	34.7	0.0049	0.0030
9-10-404	0.46225	37.9	39.8	37.6	38.5	0.0043	0.0027
S8-02-01	0.00644	20.1	19.6	19.7	19.7	0.0015	0.0011
S8-02-02	0.00919	20.6	20.0	20.1	20.1	0.0016	0.0012

VELOCITIES IN CM./SEC. HEIGHTS IN METER EXCEPT ROUGHNESS LENGTH IS IN CENTIMETERS.

WIND PROFILE DATA

PROFILE NUMBER	WIND SPEED VS. HEIGHT 1M.	2M.	5M.	10M.	PROFILE FIT	RICHARDSON NUMBER
S8-02-03	449.	479.	520.	552.	1.00	
S8-03-01	282.	307.	342.	367.	0.98	
S8-03-02	345.	377.	416.	444.	0.99	
S8-03-03	381.	416.	458.	488.	0.99	
S8-03-04	381.	412.	453.	482.	0.99	
S8-03-05	383.	408.	449.	478.	0.99	
S8-04-01	706.	744.	818.	878.	0.99	
S8-04-02	757.	797.	876.	939.	0.99	
S8-04-03	781.	822.	903.	966.	0.99	
S8-04-04	824.	869.	956.	1026.	0.99	
S8-04-05	838.	870.	962.	1032.	0.98	
S8-04-06	776.	817.	900.	965.	0.99	
S8-07-01	378.	389.	435.	464.	0.98	
S8-07-02	368.	378.	460.	512.	0.82	
S8-07-03	395.	407.	451.	480.	0.98	
S8-07-04	413.	430.	470.	497.	0.99	
S8-07-05	428.	447.	493.	522.	0.99	
S8-07-06	474.	499.	547.	580.	1.00	
S8-07-07	484.	505.	560.	598.	0.98	
S8-07-08	477.	502.	554.	590.	1.00	
S8-07-09	451.	477.	523.	555.	1.00	
S8-07-10	430.	456.	501.	532.	1.00	
S8-07-11	461.	479.	584.	636.	0.91	
S8-09-01	454.	478.	527.	562.	0.99	
S8-09-02	441.	460.	506.	540.	0.99	
S8-09-03	446.	467.	514.	549.	0.99	
S8-09-04	440.	458.	504.	537.	0.99	
S8-09-05	415.	430.	480.	512.	0.99	
S8-09-06	439.	460.	510.	545.	0.99	
S8-15-01	263.	261.	311.	334.	0.95	
S8-15-02	249.	243.	297.	319.	0.94	
S8-15-03	305.	318.	364.	392.	0.99	
S8-15-04	337.	354.	428.	479.	0.87	
S8-15-05	359.	373.	430.	465.	0.99	
S8-15-06	322.	330.	405.	443.	0.94	
S8-15-07	336.	344.	389.	414.	0.98	
S8-15-08	366.	378.	475.	519.	0.95	
S8-16-01	341.	358.	403.	436.	0.97	
S8-16-02	345.	364.	420.	461.	0.96	
S8-16-03	338.	357.	415.	456.	0.97	

VELOCITIES IN CM./SEC. HEIGHTS IN METERS

DERIVED PROFILE DATA

PROFILE NUMBER	ROUGHNESS LENGTH	FRICTION VELOCITY 1M.	2M.	5M.	10M.	DRAG COEF. 2M.	10M.
S8-02-03	0.00680	18.7	18.6	18.6	18.6	0.0015	0.0011
S8-03-01	0.03220	14.0	14.1	14.2	14.2	0.0021	0.0015
S8-03-02	0.01952	16.2	16.3	16.4	16.4	0.0019	0.0014
S8-03-03	0.01263	17.0	17.2	17.3	17.3	0.0017	0.0013
S8-03-04	0.01073	16.7	16.8	16.9	16.9	0.0017	0.0012
S8-03-05	0.00947	16.5	16.4	16.5	16.5	0.0016	0.0012
S8-04-01	0.03851	35.9	34.8	34.5	34.5	0.0022	0.0015
S8-04-02	0.03060	37.4	36.3	36.1	36.1	0.0021	0.0015
S8-04-03	0.02622	37.9	36.8	36.6	36.6	0.0020	0.0014
S8-04-04	0.04006	42.1	40.8	40.5	40.5	0.0022	0.0016
S8-04-05	0.04140	43.0	41.0	40.9	40.9	0.0022	0.0016
S8-04-06	0.03385	38.8	37.6	37.5	37.5	0.0021	0.0015
S8-07-01	0.01356	17.0	16.2	16.5	16.5	0.0017	0.0013
S8-07-02	1.13545	32.9	29.2	30.2	30.2	0.0060	0.0035
S8-07-03	0.01313	17.7	16.9	17.1	17.1	0.0017	0.0013
S8-07-04	0.00367	16.2	15.8	15.9	15.9	0.0013	0.0010
S8-07-05	0.00490	17.3	16.8	17.1	17.1	0.0014	0.0011
S8-07-06	0.00621	19.6	19.2	19.4	19.4	0.0015	0.0011
S8-07-07	0.01874	22.6	21.8	22.0	22.0	0.0019	0.0014
S8-07-08	0.01490	21.7	21.1	21.3	21.3	0.0018	0.0013
S8-07-09	0.00490	18.2	18.0	18.1	18.1	0.0014	0.0011
S8-07-10	0.00565	17.6	17.4	17.6	17.6	0.0015	0.0011
S8-07-11	0.21739	30.1	28.1	30.2	30.2	0.0034	0.0022
S8-09-01	0.01750	21.0	20.5	20.5	20.5	0.0018	0.0013
S8-09-02	0.01343	19.8	19.1	19.2	19.2	0.0017	0.0013
S8-09-03	0.01837	20.7	20.1	20.1	20.1	0.0019	0.0013
S8-09-04	0.01185	19.5	18.8	18.9	18.9	0.0017	0.0012
S8-09-05	0.01365	18.7	17.9	18.3	18.3	0.0017	0.0013
S8-09-06	0.01878	20.5	19.8	20.0	20.0	0.0019	0.0014
S8-15-01	0.03827	13.4	12.2	13.1	13.1	0.0022	0.0015
S8-15-02	0.05371	13.2	11.8	13.0	13.0	0.0024	0.0017
S8-15-03	0.05172	16.1	15.4	15.9	15.9	0.0023	0.0016
S8-15-04	1.42245	31.7	28.6	29.2	29.2	0.0065	0.0037
S8-15-05	0.11693	21.3	20.0	20.6	20.6	0.0029	0.0020
S8-15-06	0.31569	22.4	20.5	22.0	22.0	0.0038	0.0025
S8-15-07	0.00969	14.5	13.9	14.3	14.3	0.0016	0.0012
S8-15-08	0.25257	24.5	22.7	25.0	25.0	0.0036	0.0023
S8-16-01	0.09646	19.6	18.8	18.8	18.8	0.0027	0.0019
S8-16-02	0.42618	25.3	23.7	23.8	23.8	0.0042	0.0027
S8-16-03	0.48278	25.3	23.7	23.9	23.9	0.0044	0.0027

VELOCITIES IN CM./SEC. HEIGHTS IN METER EXCEPT ROUGHNESS LENGTH IS IN CENTIMETERS.

WIND PROFILE DATA

PROFILE NUMBER	WIND SPEED VS. HEIGHT 1M.	2M.	5M.	10M.	PROFILE FIT	RICHARDSON NUMBER
S8-16-04	342.	361.	436.	494.	0.93	
S8-16-05	360.	381.	442.	489.	0.96	
S8-16-06	353.	373.	442.	492.	0.95	
S8-16-07	384.	398.	472.	530.	0.91	
S8-16-08	390.	407.	476.	531.	0.92	
S8-16-09	364.	376.	445.	497.	0.92	
S8-16-10	382.	394.	445.	483.	0.94	
S8-16-11	410.	427.	466.	494.	0.99	
S8-16-12	413.	429.	486.	530.	0.93	
S8-16-13	396.	408.	471.	519.	0.93	
S8-16-14	405.	421.	477.	520.	0.94	
S8-16-15	414.	430.	497.	547.	0.94	
S8-17-01	283.	301.	383.	438.	0.97	
S8-17-02	260.	280.	370.	433.	0.96	
S8-17-03	263.	284.	381.	449.	0.95	
S8-17-07	272.	288.	368.	422.	0.96	
S8-17-08	243.	256.	330.	379.	0.96	
S8-17-09	255.	267.	335.	382.	0.95	
S8-17-10	239.	250.	278.	297.	0.85	
S8-17-11	261.	274.	335.	377.	0.96	
S8-17-12	287.	302.	363.	406.	0.96	
S8-17-13	272.	289.	349.	392.	0.97	
S8-17-15	241.	258.	327.	375.	0.96	
S8-17-16	263.	283.	354.	403.	0.97	
S8-18-01	545.	576.	660.	721.	0.97	
S8-18-02	499.	531.	613.	671.	0.98	
S8-18-03	538.	565.	669.	745.	0.95	
S8-18-04	619.	642.	729.	786.	0.98	
S9-21-01	424.	456.	506.	544.	0.99	
S9-21-02	449.	477.	528.	567.	1.00	
S9-21-03	508.	531.	583.	622.	0.99	
S9-21-05	489.	512.	566.	606.	0.99	
S9-21-06	511.	536.	593.	636.	0.99	
S9-21-08	513.	541.	590.	628.	1.00	
S9-21-09	516.	542.	582.	612.	1.00	
S9-21-10	559.	585.	638.	678.	0.99	
S9-21-12	618.	645.	700.	742.	0.99	
S9-21-13	601.	630.	687.	729.	1.00	
S9-21-14	512.	543.	594.	632.	1.00	
S9-26-01	746.	762.	817.	860.	0.98	

VELOCITIES IN CM./SEC. HEIGHTS IN METERS

DERIVED PROFILE DATA

PROFILE NUMBER	ROUGHNESS LENGTH	FRICTION VELOCITY 1M.	2M.	5M.	10M.	DRAG COEF. 2M.	10M.
S8-16-04	2.63131	37.6	33.3	33.2	33.2	0.0085	0.0045
S8-16-05	0.63903	28.5	26.5	26.6	26.6	0.0048	0.0030
S8-16-06	1.18588	31.8	29.1	29.2	29.2	0.0061	0.0035
S8-16-07	1.67790	37.6	33.3	33.2	33.2	0.0070	0.0039
S8-16-08	1.22203	35.4	31.9	31.7	31.7	0.0062	0.0036
S8-16-09	1.39012	34.1	30.3	30.2	30.2	0.0065	0.0037
S8-16-10	0.14873	23.5	21.9	21.9	21.9	0.0031	0.0021
S8-16-11	0.00434	16.3	15.9	16.0	16.0	0.0014	0.0010
S8-16-12	0.23548	27.3	25.4	25.4	25.4	0.0035	0.0023
S8-16-13	0.51139	30.0	27.3	27.4	27.4	0.0045	0.0028
S8-16-14	0.21878	26.4	24.7	24.7	24.7	0.0034	0.0023
S8-16-15	0.48938	31.1	28.6	28.7	28.7	0.0044	0.0028
S8-17-01	4.10586	35.5	31.0	31.9	31.9	0.0106	0.0053
S8-17-02	8.46464	42.1	35.4	36.3	36.3	0.0160	0.0070
S8-17-03	10.27388	46.2	38.3	39.2	39.2	0.0182	0.0076
S8-17-07	4.50126	35.1	30.4	31.3	31.3	0.0111	0.0055
S8-17-08	4.98391	32.4	27.7	28.6	28.6	0.0117	0.0057
S8-17-09	3.57226	30.6	26.5	27.1	27.1	0.0099	0.0050
S8-17-10	0.01741	11.0	10.7	10.8	10.8	0.0018	0.0013
S8-17-11	2.06298	26.9	24.0	24.4	24.4	0.0076	0.0042
S8-17-12	1.42371	27.0	24.4	24.8	24.8	0.0065	0.0037
S8-17-13	1.61513	26.4	24.0	24.4	24.4	0.0069	0.0039
S8-17-15	4.50604	31.1	27.2	27.7	27.7	0.0111	0.0055
S8-17-16	3.53801	31.5	28.1	28.6	28.6	0.0098	0.0050
S8-18-01	0.25438	36.5	34.6	34.8	34.8	0.0036	0.0023
S8-18-02	0.33020	34.9	33.2	33.5	33.5	0.0039	0.0025
S8-18-03	1.08616	47.6	43.3	43.6	43.6	0.0059	0.0034
S8-18-04	0.07731	34.6	32.7	33.2	33.2	0.0026	0.0018
S9-21-01	0.04732	22.2	21.9	21.9	21.9	0.0023	0.0016
S9-21-02	0.03715	22.7	22.2	22.2	22.2	0.0022	0.0015
S9-21-03	0.01726	23.5	22.7	22.7	22.7	0.0018	0.0013
S9-21-05	0.03203	24.3	23.4	23.4	23.4	0.0021	0.0015
S9-21-06	0.03494	25.7	24.8	24.8	24.8	0.0021	0.0015
S9-21-08	0.00894	22.0	21.6	21.6	21.6	0.0016	0.0012
S9-21-09	0.00076	17.5	17.4	17.4	17.4	0.0010	0.0008
S9-21-10	0.00781	23.6	23.1	23.1	23.1	0.0016	0.0012
S9-21-12	0.00456	24.7	24.1	24.1	24.1	0.0014	0.0011
S9-21-13	0.00696	25.1	24.6	24.6	24.6	0.0015	0.0011
S9-21-14	0.01078	22.4	22.1	22.1	22.1	0.0017	0.0012
S9-26-01	0.00072	25.2	24.3	24.3	24.3	0.0010	0.0008

VELOCITIES IN CM./SEC. HEIGHTS IN METER EXCEPT ROUGHNESS LENGTH IS IN CENTIMETERS.

WIND PROFILE DATA

PROFILE NUMBER	WIND SPEED VS. HEIGHT 1M.	2M.	5M.	10M.	PROFILE FIT	RICHARDSON NUMBER
S9-26-02	775.	788.	843.	886.	0.97	
S9-26-03	756.	767.	818.	856.	0.97	
S9-26-04	756.	770.	824.	864.	0.98	
S9-26-05	769.	788.	847.	891.	0.98	
S9-26-06	769.	775.	825.	862.	0.96	
S9-26-07	757.	769.	820.	859.	0.97	
S9-26-08	770.	779.	832.	873.	0.97	
S9-26-09	841.	887.	943.	987.	1.00	
S9-26-10	916.	860.	959.	1016.	0.71	
S9-26-11	822.	860.	924.	973.	0.99	
S9-26-12	834.	873.	921.	959.	1.00	
S9-26-13	862.	907.	954.	992.	1.00	
S9-26-14	838.	875.	938.	984.	0.99	
S9-26-15	761.	775.	831.	873.	0.98	
S9-26-16	776.	782.	836.	877.	0.96	
S9-26-17	760.	772.	826.	866.	0.97	
S9-26-18	828.	873.	936.	984.	1.00	
S9-26-19	841.	884.	932.	971.	1.00	
S9-26-20	849.	887.	947.	990.	1.00	

DERIVED PROFILE DATA

PROFILE NUMBER	ROUGHNESS LENGTH	FRICTION VELOCITY 1M.	2M.	5M.	10M.	DRAG COEF. 2M.	10M.
S9-26-02	0.00047	25.2	24.3	24.3	24.3	0.0010	0.0008
S9-26-03	0.00018	22.9	22.1	22.1	22.1	0.0008	0.0007
S9-26-04	0.00040	24.3	23.5	23.5	23.5	0.0009	0.0007
S9-26-05	0.00086	26.4	25.5	25.5	25.5	0.0010	0.0008
S9-26-06	0.00011	22.4	21.5	21.5	21.5	0.0008	0.0006
S9-26-07	0.00021	23.2	22.3	22.3	22.3	0.0008	0.0007
S9-26-08	0.00030	24.2	23.2	23.2	23.2	0.0009	0.0007
S9-26-09	0.00020	25.6	25.7	25.6	25.6	0.0008	0.0007
S9-26-10	0.00452	36.6	32.2	33.0	33.0	0.0014	0.0011
S9-26-11	0.00090	28.3	27.9	28.0	28.0	0.0011	0.0008
S9-26-12	0.00002	21.9	22.0	21.9	21.9	0.0006	0.0005
S9-26-13	0.00001	21.9	22.1	22.0	22.0	0.0006	0.0005
S9-26-14	0.00040	27.0	26.7	26.7	26.7	0.0009	0.0007
S9-26-15	0.00054	25.1	24.2	24.2	24.2	0.0010	0.0008
S9-26-16	0.00038	24.9	23.7	23.7	23.7	0.0009	0.0007
S9-26-17	0.00034	24.2	23.3	23.3	23.3	0.0009	0.0007
S9-26-18	0.00076	28.1	28.0	27.9	27.9	0.0010	0.0008
S9-26-19	0.00003	22.6	22.7	22.6	22.6	0.0007	0.0005
S9-26-20	0.00010	24.6	24.5	24.6	24.6	0.0008	0.0006

Appendix II

Digital Data Processing

Initial plans for the collection and analysis of field data called for the use of analog data processing, using procedures similar to those described by Seesholtz (1968). It became clear, however, that the type of data processing required to adequately investigate the physical phenomena demanded the use of digital computation. The principal limitations of the existing analog system were:

1. The inability to compute cospectra and quadrature spectra.

2. The distortion of spectral estimates caused by linear trends in the data. This problem was most pronounced in the wind data, where strong linear trends were often present.

3. The inability to compute probability density and joint probability density distributions.

4. The restricted precomputation and preprocessing of data before statistical measures were computed.

The shift to digital processing introduced a new set of problems in the overall data handling. The major digital processing handicaps were:

1. The need to develop the processing programs from scratch.

2. Analog-digital conversion facilities with a maximum 10-bit resolution. A minimum of 12 bits are required for significance with some of the data (see Chapter II).

The programs were completely written and tested out in a period of two months. This was accomplished by using the most direct analytic methods possible in all computations. A more refined program could have

been written, however the time required to master the subtleties the computer or advanced computation techniques was not considered warranted.

The analog to digital conversion facility is maintained by the Department of Mechanical Engineering at the Massachusetts Institute of Technology. The facility consists of a Raytheon 16 channel Analog to digital converter connected to an IBM 1130 computer. The converter will accept signals with a maximum signal level of $\pm$10 volts, and will sample at any preset sample rate up to about 6000 samples per second. The final output is standard IBM punched cards formatted with 56 data points per card.

Analog data tapes were prepared for digitizing by prefixing each data tape with a leader containing a square wave calibration signal. The tapes, along with their leaders, were then digitized at 10 times the recorded tape speed. The calibration signal at the beginning of each tape allowed optimizing the gains of each channel amplifier into the digitizer to fully use the $\pm$10 volt digitizing window. After IBM cards had been punched for each data channel, the first several hundred points, which included the calibration signal, were printed out. The digitized value of the calibration signal was then used to determine a scale factor for the data to be used in later computation.

The general procedure for digital processing followed those recommended by Bendat and Piersol (1966). The theoretical maximum sampling period is:

$$t = \frac{1}{2f_c} \qquad \text{(AII.1)}$$

Where f_c is the maximum significant frequency in the record. For wind studies over the ocean, there is little energy of concern above 0.5Hz, however on occasion there may be reason to study up to 1.0Hz. For accurate correlation function measurements, however, Bendat and Piersol recommend:

$$\Delta t = \frac{1}{4f_c} \qquad \text{(AII.2)}$$

On this basis, most of the records were digitized with a digitizing period of 0.2 seconds, while some were digitized with a period of 0.4 seconds.

While correlation functions require data with high sampling rates, the resolution bandwidth for power spectra is given by:

$$B_e = \frac{1}{\Delta t m} \qquad \text{(AII.3)}$$

where m is the number of correlation lags. Similarly the normalized standard error, ε, is specified by:

$$\varepsilon = \sqrt{\frac{m}{N}} \qquad \text{(AII.4)}$$

Where N is the sample size. The computation cost is directly proportional to m, while the error increases with increasing m. It is therefore advantageous to specify as small a value for m as possible. From equation (AII.3), however, the spectral resolution decreases with decreasing m, and increases with both increasing m and Δt. Consequently for spectra, as large as possible Δt is desireable. The program has been set up, therefore, to provide the basic Δt for computations requiring

high sample rates, however the sample period Δt is doubled by discarding every other point for spectra computations.

After the analog data was digitized and the cards prepared for processing, the following digital computations were performed in the order listed:

1. Input. Data, control information, and supplementary information was read into memory. The program could handle four simultaneous channels, each with 9600 data points.

2. Scaling. Each channel of data was multiplied by a scaling constant provided in the input to restore the digitized data to physically meaningful values.

3. Special processing. Special processing included manipulation of data as required for this study and other program users. Special processing included the resolution of hotwire data as described in Chapter II, and the building of data array consisting of the product U(t)W(t) for correlation of Reynolds stress with wave height.

4. Computation and removal of mean and trend. The mean was computed using the formula:

$$\bar{x} = \frac{1}{N} \sum_{i=1}^{N} x_i \qquad \text{(AII.5)}$$

For computing the trend, cognizance is taken of the fact that the indexing variable, i, is a function of time since each adjacent storage location is filled with data sampled at even intervals of Δt. Consequently one can compute the linear regression formula where the value of the

variable is correlated with its location in the array. Therefore, the predicted value of x at any point (denoted as x') is from (Hoel (1954, p 127)):

$$x' = \left[\frac{\sum_{i=1}^{N} x_i i - N\bar{x}\left(\frac{N}{2}\right)}{\sum_{i=1}^{N} i^2 - N\left(\frac{N^2}{4}\right)} \right]\left(i - \frac{N}{2}\right) + \bar{x} \qquad \text{(AII.6)}$$

Simplifying, and noting that we want to subtact x' from each value of x, ie: $x_i - x'_i$, the corrected value of the data in each array, $\hat{x}$, becomes:

$$\hat{x}_i = x_i - \left[\frac{\sum_{i=1}^{N} x_i i - \frac{N^2}{2}\bar{X}}{\sum_{i=1}^{N} i^2 - \frac{N^3}{4}} \right]\left(i - \frac{N}{2}\right) - \bar{x} \qquad \text{(AII.7)}$$

The quantity in the brackets in equation (AII.7) is the slope of the linear trend line. This quantity is printed out with the other statistical measures to allow the user to assess the magnitude and effect of the trend. This technique of trend correction provides a clear spectrum of spectral components of frequencies equal to or higher than $f_L = 1/N(\Delta t)$. Estimates of the power spectral density between 0 and f_L will be in error unless there isn't a trend. The low frequency components will appear as a higher frequency. This can best be graphically illustrated. Figure AII.1 shows an arbitrary frequency component of $f<f_L$, with period T. The trend line, AA', is drawn as the best fit of this component, resulting in an apparent period T'. The period T' is less than T, showing that the low frequency component is represented as a higher frequency. Consequently, while the technique of linear trend removal is simple and direct, the first data point of the raw

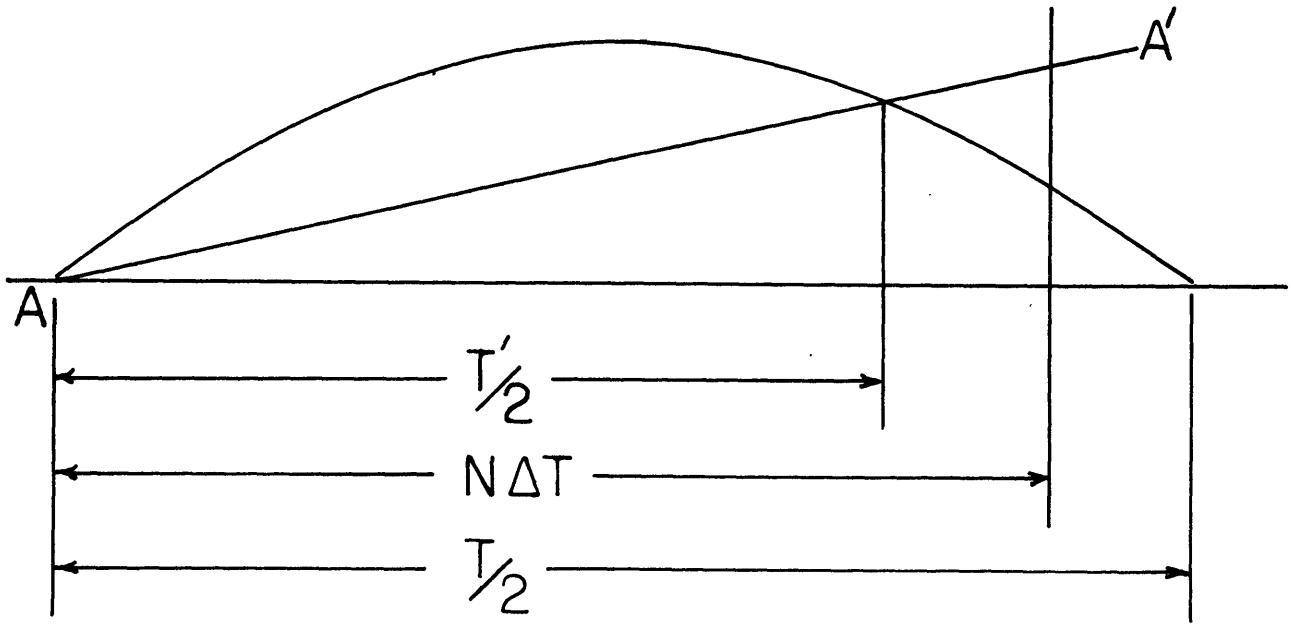

Figure AII.1

Frequency shift of low frequency components caused by linear trend line AA'. Frequency component with period T is represented as a frequency with period T'.

spectrum or the first two data points of the smoothed spectrum will have incorrect power spectral density estimates unless the linear trend line has a slope near zero. In practice, since the maximum array capicity is 9600 data points, a slope of order 10^{-4} or smaller can be interpreted as a zero slope.

5. Computation of higher order moments. The second through the fourth moments are computed and listed for the data in each channel using the following formulas:

$$\text{variance } \overline{X^2} = \left[\frac{1}{N-1} \sum_{i=1}^{N} \hat{X}_i^{\,2}\right]$$

$$\text{Skew } M_3 = \left[\frac{1}{N} \sum_{i=1}^{N} X_i^{\,3}\right] (\overline{X^2})^{-3/2}$$

$$\text{Kurtosis } M_4 = \left[\frac{1}{N} \sum_{i=1}^{N} \hat{X}_i^{\,4}\right] (\overline{X^2})^{-2} \qquad \text{(AII.8)}$$

6. Probability Density. A frequency histogram or a joint frequency histogram for any variable or any pair of variables can be constructed for up to a maximum of 40 class intervals for each variable. The technique is an elementary sorting procedure.

7. Correlation function. Following Bendat and Piersol (1966), the correlation function can be computed for M lags:

$$R_{xy}(j) = \frac{1}{N-j} \sum_{i=1}^{i=N-j} X_i Y_{i+j} \qquad j = 0, 1, 2, \ldots M \qquad \text{(AII.9)}$$

Where the subscript j denotes the jth lag, corresponding to a time lag of $j\Delta t$. For $j\Delta t = \tau$, equation (AII.9) may also be represented as

$R_{xy}(\tau) = \langle x(t)y(t+\tau)\rangle$. If $y_i = x_i$ then equation (AII.9) represents an autocorrelation where:

$$R_{xy}(\tau) = R_{xy}(-\tau) \qquad \text{(AII.10)}$$

Consequently when x = y only the function $R_{xy}(\tau)$ is computed. For a cross-correlation, however, $R_{xy}(\tau)$ and $R_{xy}(-\tau)$ is computed, where $R_{xy}(-\tau) = R_{yx}(\tau)$

8. Power spectral density. The final computation is the fourier transformation of the correlation function into the cospectral density function and the quadrature spectral density function and then representing these as a power function and phase angle. The correlation function can be represented as an odd and an even part:

$$Aj = \frac{1}{2}\,[R_{xy}(j) + R_{yx}(j)]$$

$$Bj = \frac{1}{2}[R_{xy}(j) - R_{yx}(j)] \qquad \text{(AII.11)}$$

For an autocorrelation, $Aj = R_{xy}(j)$ and Bj = 0, however for a cross correlation, both Aj and Bj may be different from zero. If $C_{xy}(f)$ is the co-spectral density and $Q_{xy}(f)$ is the quadrature spectral density, then the spectral density estimates are:

$$C_{xy}(f) = 2\Delta t\left[A_o + 2\sum_{j=1}^{M-1} Aj \cos\left(\frac{\Pi jf}{f_c}\right) + A_M \cos\left(\frac{\Pi Mf}{f_c}\right)\right]$$

$$Q_{xy}(f) = 2\Delta t\left[2\sum_{j=1}^{M-1} Bj \sin\left(\frac{\Pi jf}{f_c}\right) + B_M \sin\left(\frac{\Pi Mf}{f_c}\right)\right] \qquad \text{(AII.12)}$$

where:

$$f = \frac{kf_c}{M} \qquad K = 0, 1, 2, \ldots M$$

Smooth estimates are calculated by smoothing the spectral density estimates by the Hanning method:

$$
\begin{aligned}
C_k &= 0.25\ C_{k-1} + 0.5\ C_k + 0.25\ C_{k+1} \\
Q_k &= 0.25\ Q_{k-1} + 0.5\ Q_k + 0.25\ Q_{k+1} \\
C_o &= 0.5\ C_o + 0.5\ C_1 \\
Q_o &= 0.5\ Q_o + 0.5\ Q_1 \\
C_m &= 0.5\ C_m + 0.5\ C_{m-1} \\
Q_m &= 0.5\ Q_m + 0.5\ Q_{m-1}
\end{aligned}
\qquad \text{(AII.13)}
$$

Finally the spectral density estimates can be represented as a power and phase angle:

$$
\begin{aligned}
P_{xy}(f) &= (C_k^2 + Q_k^2)^{1/2} \\
\Theta_{xy}(f) &= \tan^{-1}\left(\frac{Q_k}{C_k}\right)
\end{aligned}
\qquad \text{(AII.14)}
$$

These are listed and plotted for analysis.

Appendix III

Hotwire Linearizer Design

General Discussion

Effective field use of hotwire anemometers for the study of meteorological turbulence is complicated by the inherently non-linear output of the anemometer. Of the several solutions to this problem, the simplest and most direct is to linearize the hotwire anemometer signal in the field before recording. This approach, from a data processing viewpoint, facilitates system calibration, error tracing, and bookkeeping while recording and processing the data.

While the advantages of hotwire linearization are usually self-evident, economic dictates usually result in adopting alternate procedures. The linearizer discussed herein is one approach to providing direct hotwire linearization while circumventing the cost problem. The linearizer has limited performance, and is unsuited for high frequency measurements. High frequencies are seldom of significance in the field study of meteorological turbulence, however, making the instrument suited for this application.

Design

The response of a hotwire system can be represented by:

$$E^2 - E_o^2 = RC\sqrt{U} \qquad \text{(A3.1)}$$

Where E is the output voltage of the anemometer, E_o is the offset voltage, C the response characteristic of the anemometer, R the operating resistance of the hotwire, and U the wind velocity. The output voltage E can be written:

$$E = E_o + \Delta E \qquad \text{(A3.2)}$$

where ΔE is the difference voltage between the offset voltage and the

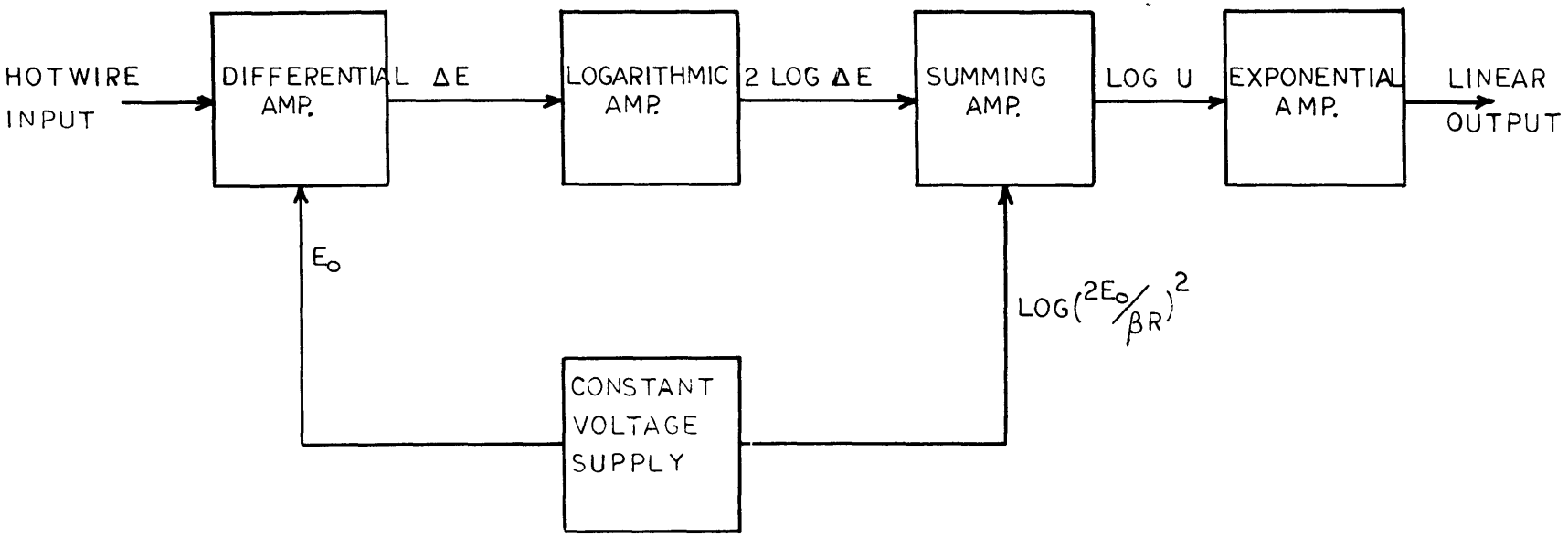

BLOCK DIAGRAM

Figure AIII.1 Block Diagram of Linearizer

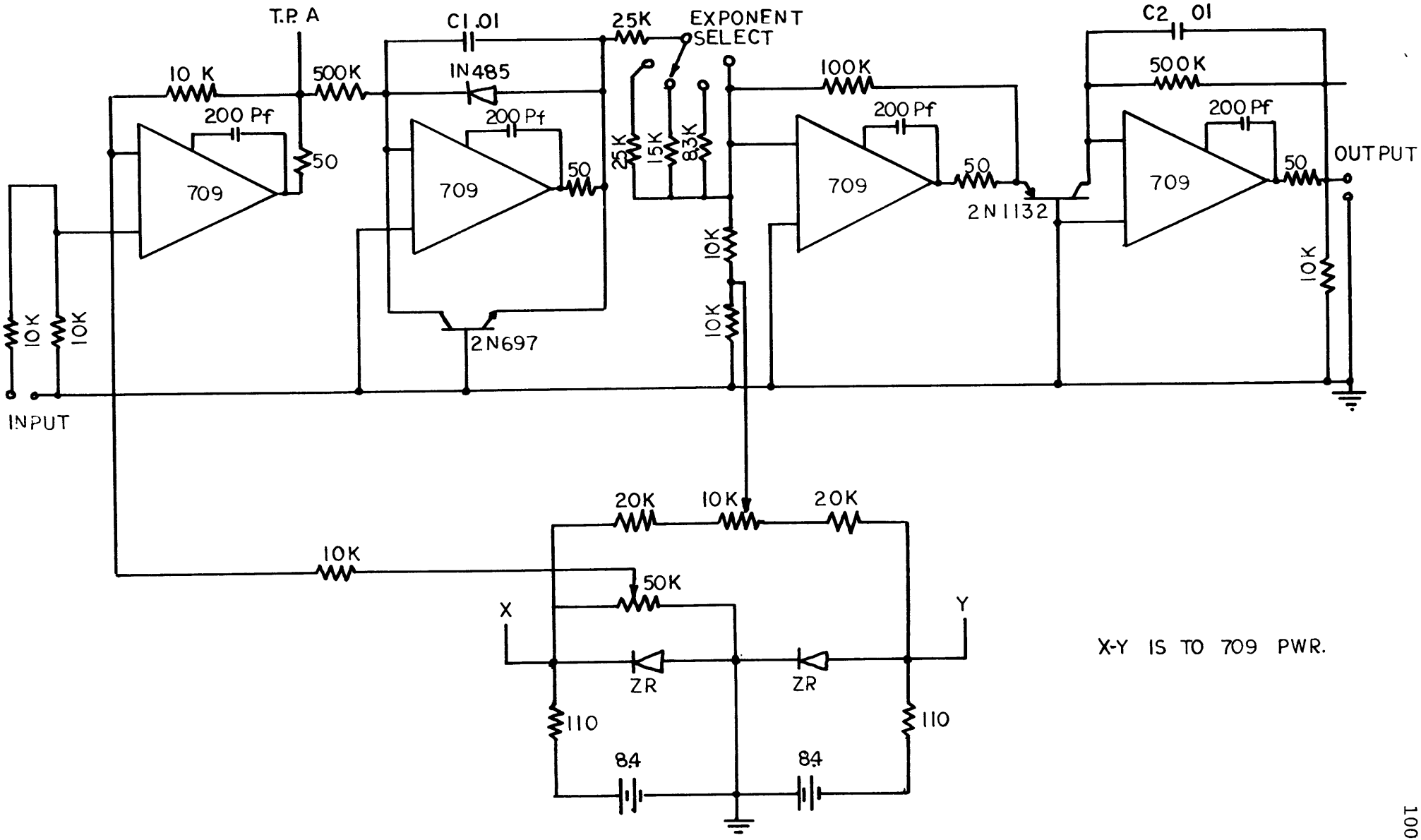

X-Y IS TO 709 PWR.

FIGURE AII.2

HOTWIRE LINEARIZER

output voltage. Substituting equation (A3.2) into (A3.1), the neglecting terms of order ΔE^3 or greater, the transfer function of the linearizer becomes:

$$U = \left(\frac{2E_o}{CR} \right)^2 \Delta E^2 \qquad \text{(A3.3)}$$

The terms enclosed by the parenthesis are constant for any given anemometer system, and need only be set into the linearizer during the initial calibration of the linearizer.

In order to express equation (A3.3) in a form suitable for analog computation, the products are expressed as a sum of logarithms:

$$\text{Log } K + 2 \log \Delta E = \log U \qquad \text{(A3.4)}$$

where:

$$K = \left(\frac{2E_o}{CR} \right)^2$$

Equation (A3.4) can be represented in terms of amplifier building blocks as shown in figure 1. Using standard non-linear amplifier circuits, the circuit as shown in figure 2 was developed.

The construction of the linearizer is straight forward, using standard components.

The functional relationships incorporated into the linearizer crucially depend upon the accuracy of the resistors used in the construction of the set. Consequently all resistors used in the linearizer should be temperature compensated precision metal film resistors.

The frequency response of the linearizer is controlled by capacitors C1 and C2. The frequency response of the linearizer can be extended by replacing these capacitors by smaller valued units, say .001 microfarads. Care should be excercised here, however, since excessive reduction of the values of C1 and C2 will degrade the stability of the linearizer.

Within limits, one can tailor the high-pass characteristics of the linearizer through judicious selection of C1 and C2 to best fit experimental requirements.

While equation (AIII.4) shows U to be a function of ΔE^2, the higher order terms become important at high wind velocities. This along with the fact that some hotwires have response functions which deviate from the ideal King's law response, results in a need for a variable exponent. Consequently a multiple exponent selection has been incorporated into the design, providing a choice of exponents of 2, 2.5, 3, and 4. The response curve of the linearizer appropriate to the test system used in conjunction with the hotwire set is shown in figure 3. The frequency response of the system is shown in figure 4.

Since a number of these linearizers were required, printed circuit boards were drilled and etched. This construction technique provides mechanical rigidity and compactness, in addition to the ease of constructing multiple units. Careful layout of the circuit and mechanical rigidity of the unit is necessary to guarantee circuit stability, particularly if the unit is destined for exposed field use.

Operation.

The output of the linearizer is a negative voltage varying over a range of approximately zero to five volts. The relationship between the output voltage and the input voltage is a function of the exponent and the operating range chosen, and must be determined by set calibration.

To initially set up the linearizer for use, the following steps are suggested:

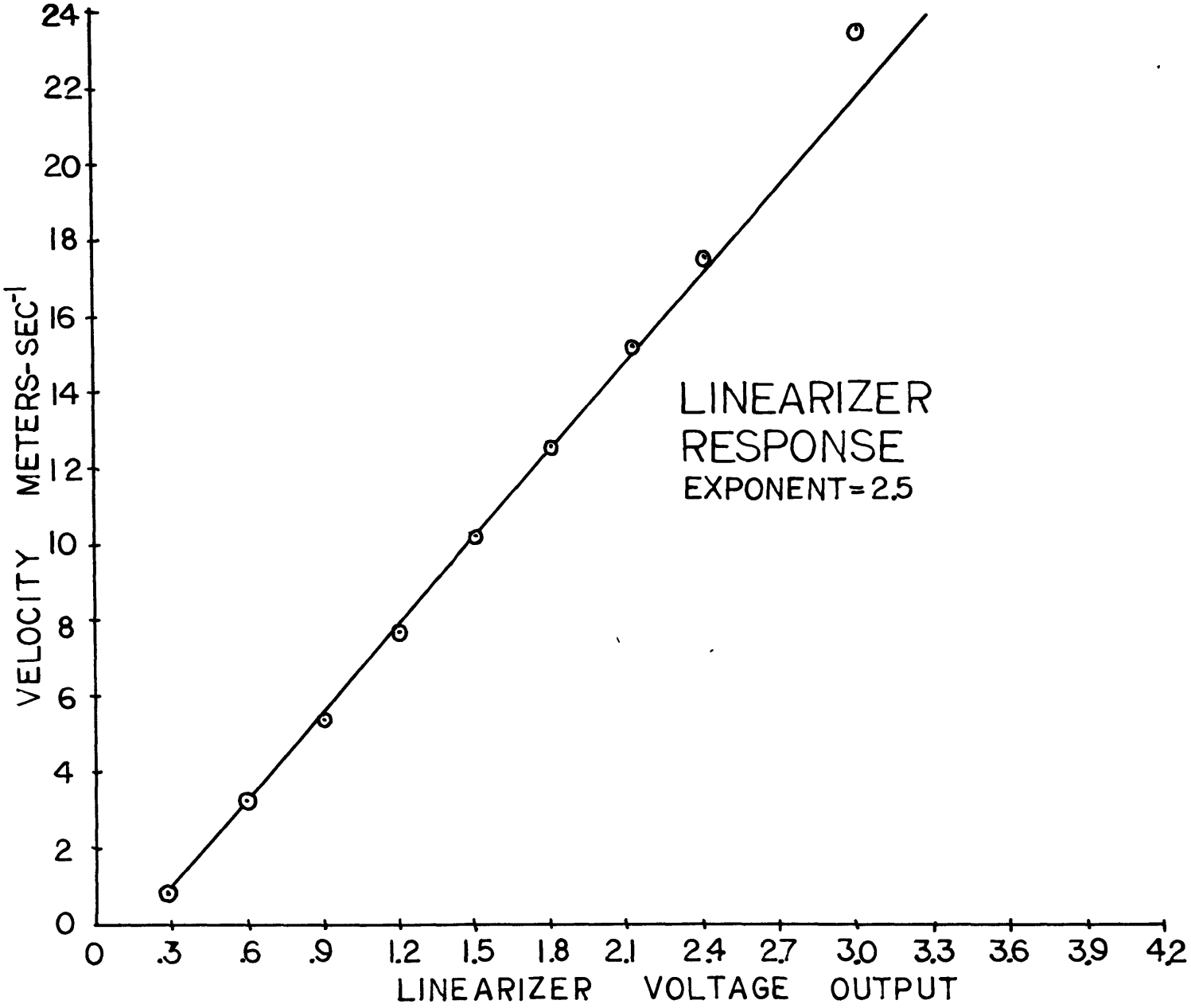

Figure AIII.3

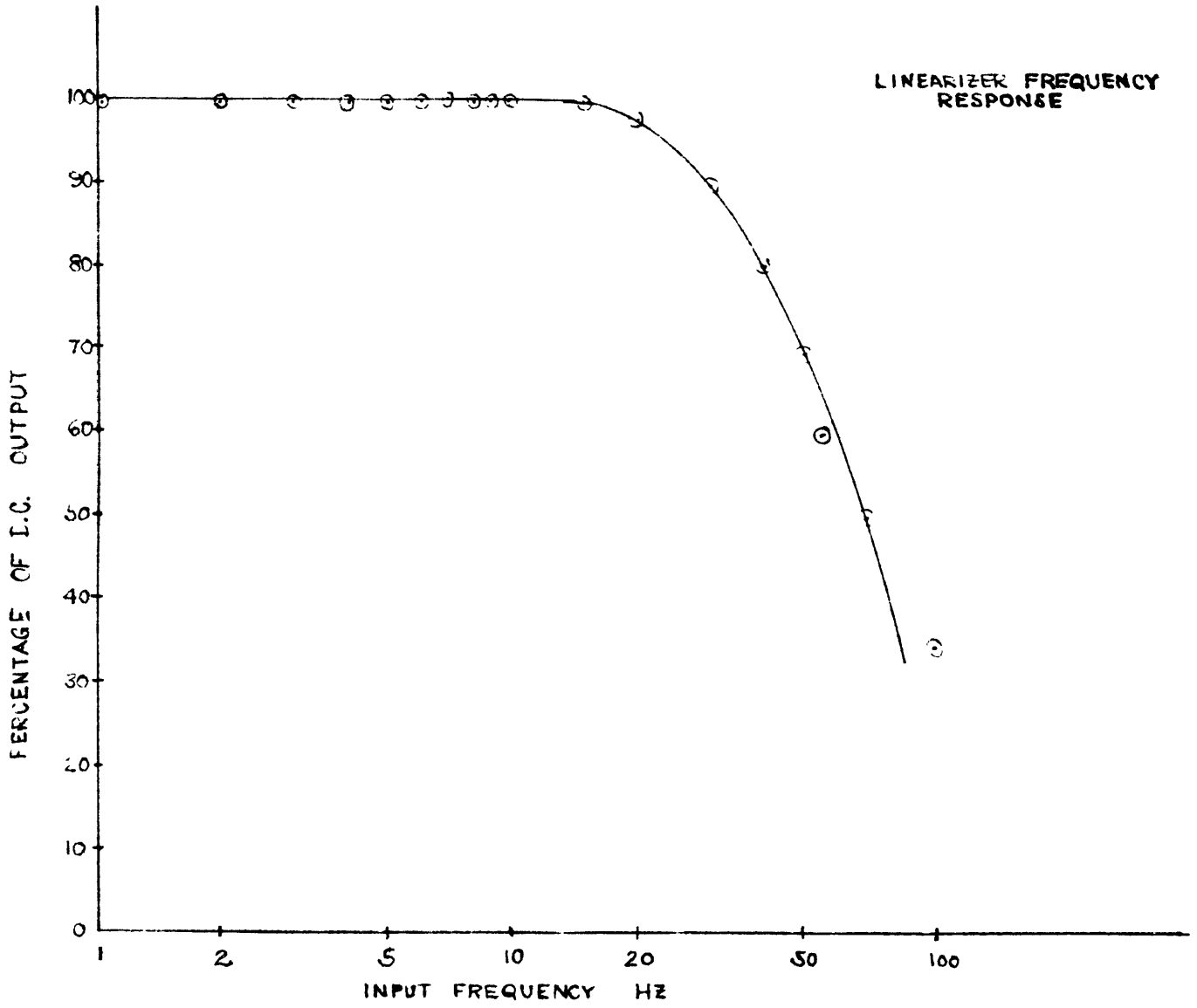

Figure AIII.4

1. Determine E_o for the hotwire set through wind tunnel calibration. The standard technique is to plot the hotwire set response on a graph with E^2 as the abscissa and $\sqrt{U}$ as the ordinate. The best fitting straight line is drawn through the plotted points, and extended until it crosses the voltage axis. The value of E_o^2 is then read off at the intersection of the voltage axis and the response line.

2. Adjust the linearizer for E_o. Impress a voltage across the input of the linearizer equal to E_o. Connect a high impedence voltmeter to test point A and ground. Adjust R1 until the voltmeter reads about 0.2 volts. Theoretically, one should adjust this voltage to read zero volts, however the logarithmic amplifier tends to depart from a logarithmic function for voltages near zero, and a small "keep-alive" voltage is kept across the amplifier to improve the response characteristics.

3. Adjust the linearizer scale. Set the exponent to the desired range. If the exponent value is not known, try 2.5 as a first approximation. Impress a voltage across the input equivalent to the hotwire voltage output corresponding to the maximum expected wind speed. Adjust R2 for a linearizer voltage output of 5 volts or any other convenient voltage depending upon the range of wind speeds of interest.

4. Check and calibrate linearizer. Run a calibration curve on the linearizer to determine the suitability of the exponent and range setting Readjust as necessary.

5. Connect the linearizer to the hotwire anemometer and operate.

Critique.

The linearizer has obvious drawbacks in both circuit performance and in the ease of setting up the instrument for use. This tradeoff is necessary to design an inexpensive unit. Ideas come to mind where the

ease of operation and the performance could be improved with incremental cost increases, however successive increments of improvement results in a deviation from the basic design objective to providing an operational linearizer at the cheapest possible cost. On the positive side the linearizer herein discussed runs at least ten times cheaper than most commerical models.

References

Barger, W. R. and W. D. Garret, 1968, Modification of the air-sea interface by artificial sea slicks, Naval Research Laboratory report 6762.

Barger, W. R., W. D. Garret, E. L. Mollo-Christensen, K. W. Ruggles, Wave damping and wind stress effects of an artificial sea slick, to be published.

Barnett, T. P., and J. C. Wilkerson, 1967, On the generation of wind waves as inferred from airborne measurements of fetchlimited spectra, J. Marine Res., 25, 1.

Bendat, J. S. and A. G. Piersol, 1966, Measurement and analysis of random data, John Wiley and Sons, Inc, New York.

Charnock, H., 1955, Wind stress on a water surface, Quart. J. Roy, Met. Soc., 81, 639-640.

Hoel, P. G., 1954, Introduction to mathematical statistics, John Wiley and Sons, New York.

Kinsman, B., 1965, Wind Waves, Prentice Hall Inc., Englewood Cliffs, New Jersey.

Kinsman, B., 1968, An exploration of the origin and persistance of the Beaufort wind force scale, Chesapeake Bay Institute, Johns Hopkins University technical report 39.

Kraus, E. B., 1968, What do we not know about the sea surface wind stress, Bull. Amer. Met. Soc., 49, 247-253.

Lamb, H., 1932, Hydrodynamics, Reprint by Dover Publications, New York.

Lighthill, M. J., 1962, Physical interpretation of the mathematical theory of wave generation by wind, J. Fluid Mech., 14, 385-398.

Lumley, J. L., and H. A. Panofsky, 1964, The structure of atmospheric turbulence, Interscience Monographs and Texts in Physics and Science XII, John Wiley and Sons, New York.

Miles, J. W., 1957, On the generation of surface waves by shear flows, J. Fluid Mech., 3, 185-209.

Monin, A. S., 1967, Turbulence in the atmospheric boundary layer, Physics of Fluids Supplement, 10, S531-S537.

Munk, W., 1947, A critical wind speed for air-sea boundary processes, J. Marine Res., 6, 203-218.

Paulson, C. A., 1967, Profiles of wind speed, temperature and humidity over the sea, NSF Scientific Report GP-2418, University of Washington, Seattle, Washington.

Phillips. O. M., 1957, On the generation of waves by turbulent wind, J. Fluid Mech., 2, 417-445.

Pond, S., 1968, Some effects of buoy motion on measurements of wind speed and stress, J. Geo. Res., 73, 507-512.

Pond, S., S. D. Smith, P. F. Hamblin, and R. W. Burling, 1966, Spectra of velocity and temperature fluctuations in the atmospheric boundary layer over the sea, J. Atmos. Sci., 23, 376-386.

Pond, S., R. W. Stewart, and R. E. Burling, 1963, Turbulence spectra in the wind over waves, J. Atmos. Sci, 20, 319-324.

Rasmussen, C. G., and B. F. Bellhouse, 1968, Low frequency characteristics of hot-film anemometers, DISA Information Bulletin Number 6, DISA S&B, Midland Park, N.J.

Roll, H. U., 1965, Physics of the Marine Atmosphere, Academic Press, New York.

Seesholtz, J. R., 1968, A field investigation of air flow immediately above ocean surface waves, Massachusetts Institute of Technology, Department of Meteorology technical report.

Snyder, R. L., and C. S. Cox, 1966, A field study of the generation of ocean waves, J. Marine Res., 24, 1966.

Stewart, R. W., 1961, The wave drag of wind over water, J. Fluid Mech., 10, 189-194.

Stewart, R. W., 1967, Mechanics of the air sea interface, Physics of Fluids Supplement, 10, S47-S55.

Weiler, H. S., and R. W. Burling, 1967, Direct measurements of stress and spectra of turbulence in the boundary layer over the sea, J. Atmos. Sci., 24, 653-664.

Wu, J., 1969, Wind stress and surface roughness at air-sea interface, J. Geo. Res., 74, 444-455.

Wu, J., 1968, Laboratory studies of wind-wave interactions, J.Fluid Mech., 34, 91-122.

Biographical Note

The author was born and raised in San Francisco, California. He attended the United States Naval Academy at Annapolis, receiving a B.S. and his commisssion in the United States Navy in 1954. After four years at sea, he attended the United States Naval Postgraduate School at Monterey, California, and received his M.S. degree in Meteorology in 1960. Commander Ruggles subsequently held a number of assignments in the Navy involving both meteorological and general line duties. He was awarded the Secretary of the Navy Commendation medal for original research in anti-submarine warfare techniques, and was commanding officer of the U.S.S. Firm (MSO-444). Beofre undertaking advanced studies at the Massachusetts Institute of Technology, Commander Ruggles served on the staff of the Commander-in-Chief, U.S. Pacific Fleet, where he worked in Electronic Warfare. Upon completion of his studies, the author will report as officer-in-charge of project FAMOS (Fleet Applications of Meteorological Orbiting Satellites) in Washington, D.C.

Commander Ruggles is married to the former Gilda Ide of Spotswood, New Jersey. They have two children, a daughter nine and a son seven.